Metal oxide thin films for optoelectronic applications

Sapna D. Ponja

Supervised by:

Professors Claire J. Carmalt and Ivan P. Parkin

This thesis is submitted in partial fulfilment of the requirements for the Degree of Doctor of Philosophy in Chemistry

2018

I, Sapna Ponja, confirm that the work presented in this thesis is my own. Where information has been derived from other sources, I confirm that this has been indicated in the thesis.

Sapna Ponja
March 2018

For Devchand Anand Ponja

Abstract

This thesis details the use of aerosol assisted chemical vapour deposition to deposit transparent conducting oxide thin films. Transparent conducting oxides are a special class of materials that exhibit high optical transparency as well as good electrical conductivity, two properties usually in contradiction with each other. The combination of these properties in one material has established an essential role for transparent conducting oxides in a range of applications such as flat screen displays, photovoltaic cells, gas sensors, low-emissive coatings and light emitting diodes.

Aerosol assisted chemical vapour deposition is increasingly becoming recognised as a simple, low-cost and reliable technique for depositing thin films. It involves generating an aerosol mist from a solution containing the precursors that is transported with the aid of an inert or reactive carrier gas into the reaction chamber where deposition takes place on a heated substrate. Two of the attractive features of this method are its versatility in allowing the use of precursors that are not suitable for conventional chemical vapour deposition methods as the method depends on solubility rather than volatility and the facility to use multiple precursors simultaneously within a single vessel.

The focus of this work is on doping and co-doping of metal oxide thin films, namely ZnO and SnO_2, to enhance their optoelectronic properties. The ZnO films were doped with group III elements aluminium or gallium, and the SnO_2 films were doped with multivalent elements antimony or tungsten. All four systems were co-doped by introducing fluorine to replace the oxygen ion in the lattice. Fluorine was used as the co-dopant because of its established use in fluorine doped tin(IV) oxide transparent conducting oxides, a commercially available product. Co-doping has received less attention compared with single cation doping largely because of the limitations of other deposition methods. The rationale for co-doping is that it would allow greater tuning of the optoelectronic properties of the transparent conducting oxides to suit specific applications.

All films synthesised in this investigation were characterised using a wide range of techniques including X-ray diffraction, energy and/or wavelength dispersive X-ray spectroscopy, X-ray photoelectron spectroscopy, scanning electron microscopy, UV-visible-near infrared spectroscopy and Hall effect measurements.

Publications – *during the PhD*

1. Sapna D. Ponja, Sanjayan Sathasivam, Ivan P. Parkin and Claire J. Carmalt. Aerosol assisted chemical vapour deposition of highly transparent and conductive tungsten doped and tungsten-fluorine doped tin(IV) oxide thin films In preparation, 2018.

2. Sapna D. Ponja, Sanjayan Sathasivam, Ivan P. Parkin and Claire J. Carmalt. Highly conductive and transparent gallium doped and gallium-fluorine doped zinc oxide thin films deposited *via* aerosol assisted chemical vapour deposition. In preparation, 2018.

3. Sapna D. Ponja, Benjamin A. D. Williamson, Sanjayan Sathasivam, David O. Scanlon, Ivan P. Parkin and Claire J. Carmalt. Enhanced electrical properties of antimony doped tin oxide thin films deposited *via* aerosol assisted chemical vapour deposition. In submission, 2018.

4. Sapna D. Ponja, Sanjayan Sathasivam, Hywel O. Davies, Ivan P. Parkin and Claire J. Carmalt. Polyoxometalate Complexes as Precursors to Vanadium-Doped Molybdenum or Tungsten Oxide Thin Films by Means of Aerosol-Assisted Chemical Vapour Deposition. ChemPlusChem, 81 (3), 307-314, 2016.

5. Sapna D. Ponja, Ivan P. Parkin and Claire J. Carmalt. Synthesis and material characterization of amorphous and crystalline α-Al_2O_3 *via* aerosol assisted chemical vapour deposition. RSC Advances, 6 (105), 102956-102960, 2016.

6. Sapna D. Ponja, Sandeep K. Sehmi, Elaine Allan, Alexander J. MacRobert, Ivan P. Parkin and Claire J. Carmalt. Enhanced Bactericidal Activity of Silver Thin Films Deposited *via* Aerosol-Assisted Chemical Vapor Deposition. ACS Applied Materials and Interfaces, 7 (51), 28616-28623, 2015.

7. Sapna D. Ponja, Ivan P. Parkin and Claire J. Carmalt. Magnesium Oxide Thin Films with Tunable Crystallographic Preferred Orientation *via* Aerosol-Assisted CVD. Chemical Vapor Deposition, 21 (4-6), 145-149, 2015.

8. Sapna D. Ponja, Sanjayan Sathasivam, Ivan P. Parkin and Claire J. Carmalt. Transparent conductive aluminium and fluorine co-doped zinc oxide films *via* aerosol assisted chemical vapour deposition. RSC Advances, 4 (91), 49723-49728, 2014.

Other publications

9. Sanjayan Sathasivam, Andreas Kafizas, Sapna Ponja, Nicholas Chadwick, Davinder S. Bhachu, Salem M. Bawaked, Abdullah Y. Obaid, Shaeel Al-Thabaiti, Sulaiman N. Basahel, Claire J. Carmalt and Ivan P. Parkin. Combinatorial Atmospheric Pressure CVD of a Composite TiO_2/SnO_2 Thin Film. Chemical Vapor Deposition, 20 (1-2-3), 69-79, 2014.

10. Sapna Ponja, Sanjayan Sathasivam, Nicholas Chadwick, Andreas Kafizas, Salem M. Bawaked, Abdullah Y. Obaid, Shaeel Al-Thabaiti, Sulaiman N. Basahel, Ivan P. Parkin and Claire J. Carmalt. Aerosol assisted chemical vapour deposition of hydrophobic TiO_2–SnO_2 composite film with novel microstructure and enhanced photocatalytic activity. Journal of Materials Chemistry A, 1 (20), 6271-6278, 2013.

Acknowledgements

My deep gratitude goes first to my very understanding and patient supervisors Professors Claire J. Carmalt and Ivan P. Parkin for their immeasurable support and guidance over the years, not only academically but on a personal level too. Thank you!

Thank you to the past and present members of the research group in which I was privileged to work alongside. I am indebted to Dr Sanjayan Sathasivam who taught me everything I know about CVD and for his guidance, encouragement and bad jokes! The lab wouldn't have been the same without you. I extend my thanks to Dr Steve Firth for the useful discussions and his expertise in SEM and EDX.

I would also like to thank Dr Sandeep Sehmi for encouraging me to continue with my postgraduate studies. I cherish our friendship and would like to take this opportunity to apologise for being such a chatterbox☺

A very special thank you to Dr Mavji Patel to whom without him I would not be where I am today. From a teacher to a true friend, the only person who believed in me at the age of 15 and pushed me to aim high. I am very thankful for all your guidance, help and most importantly friendship. I could not have done it without you!

Finally, I am immensely grateful to my parents, Dipak and Divia, and my brother, Kapil for their love, support and putting up with my mood swings throughout my student years. I extend my gratitude to my wider family and friends for their love and encouragement during this journey. I hope I continue to make you all proud♥

Contents

List of Figures

List of Tables

List of symbols, acronyms and abbreviations

%	percent
^{o}	degree
θ	theta
n	carrier concentration
μ	mobility
ρ	resistivity
Ω	ohms
$\square^{-1}$	per square
R_{sh}	sheet resistance
$^{o}\mathrm{C}$	degrees Celsius
K	kelvin
Å	angstroms
nm	nanometer
eV	electron volt
E_{A}	activation energy
E_{f}	Fermi energy
E_{g}	band gap
Kn	Knudsen's number
Re	Reynold's number
Tc	texture coefficient
ppm	parts per million
ppb	parts per billion
$\mathrm{V_o}$	oxygen vacancy
$\mathrm{Sn_i}$	tin interstitial
at.%	atomic percent
mol.%	mole percent
AACVD	aerosol assisted chemical vapour deposition
AFTO	antimony and fluorine co-doped tin(IV) oxide
AFZO	aluminium and fluorine co-doped zinc oxide
AGZO	aluminium and gallium co-doped zinc oxide
ALD	atomic layer deposition
ALE	atomic layer epitaxy

APCVD	atmospheric pressure chemical vapour deposition
ATO	antimony doped tin(IV) oxide
A.U.	arbitrary units
AZO	aluminium doped zinc oxide
CBM	conduction band minimum
CIGS	copper indium gallium selenide
CMOS	complementary metal-oxide semiconductors
CVD	chemical vapour deposition
DFT	density functional theory
DMD	dielectric/metal/dielectric
EDX	energy dispersive X-ray spectroscopy
EXPGUI	experiment graphical user interface
FFT	fast Fourier transform
FT-IR	Fourier transform infrared spectroscopy
FTO	fluorine doped tin(IV) oxide
FV	Frank-van der Merwe
FWHM	full width half maximum
FZO	fluorine doped zinc oxide
GC-MS	gas chromatography mass spectrometry
GFZO	gallium and fluorine co-doped zinc oxide
GSAS	general structure analysis system
GZO	gallium doped zinc oxide
ICSD	inorganic crystal structure database
IR	infrared
ITO	tin doped indium oxide
LDA	local density approximation
LPCVD	low pressure chemical vapour deposition
MOCVD	metal organic chemical vapour deposition
PECVD	plasma enhanced chemical vapour deposition
PV	photovoltaics
PVD	physical vapour deposition
SEM	scanning electron microscopy
SK	Stranski-Krastonov
TCO	transparent conducting oxide

TGA	thermogravitational analysis
UV	ultraviolet
VB	valence band
VBM	valence band maximum
VW	Volmer-Weber
WDX	wavelength dispersive X-ray spectroscopy
WFTO	tungsten and fluorine co-doped tin(IV) oxide
WTO	tungsten doped tin(IV) oxide
XPS	X-ray photoelectron spectroscopy
XRD	X-ray diffraction

1

Introduction:
Transparent conducting oxides

Transparent conductive oxides (TCO) are optically transparent materials with high electrical conductivity. TCO's are best described as having a transmittance above 80% in the visible spectrum characterised by a band gap of greater than 3.1 eV, and an electrical resistivity of no more than 10^{-3} Ω cm.[14, 15] The electrical conductivity is a consequence of the number of available charge carriers (preferably 10^{20} cm^{-3} or higher) and their mobility.[15, 16] The combination of properties in one material has established an essential role for TCOs in the production of optoelectronic devices such as flat screen displays, photovoltaic cells, gas sensors and light emitting diodes.[17, 18]

Badekar reported the first TCO, a thin film of CdO, in 1907[19] but very little progress was made on developing a practical use for it probably because of its low transparency due to a band gap of 2.3 eV.[7] Since then, a number of TCO materials have been made such as In_2O_3, ZnO and SnO_2. Of these the most successful films have been made using indium or tin based oxides, however, indium and tin (to a lesser extent) are in limited supply and relatively expensive.[15] Thus, there is a need to find alternative materials that can be employed in optoelectronic devices.

This thesis explores the current developments in the fabrication of TCO thin films focussing on the use of aerosol assisted chemical vapour deposition (AACVD) and the role of dopants and deposition conditions on the optical and electrical properties of films.

1.1 Optical properties

To be transparent and conductive would normally be contradictory since transparency requires a wide band gap, which would otherwise hinder the formation of charge carriers. A TCO with 100% transmission would only be possible if there were no free electrons that could be excited from the conduction band minimum (CBM) to higher conduction band states. Obviously, transparency is not the only desired property of a TCO. A compromise is therefore required in which the transparency and the concentration of charge carriers are as high as possible. Transmittance of TCOs can be divided into three regions: ultraviolet (UV) (10-400 nm), visible (400-700 nm) and near-infrared (>700 nm) (Fig. 1.1). An increase in charge carrier concentration would increase absorption in the near-infrared. A high electron density in the conduction band would increase the absorption and reflection by the free electron gas (plasma) and hence reducing transmittance for wavelengths higher than the plasma wavelength. This type of optical profile is generally seen in thin films consisting of FTO and is a requirement of heat mirrors (Section 1.6.3).[20, 21] The blue shifting of the plasma band onset of an increase in reflectance is also dependent on the dielectric constant (a measure of capacitance; the ability of a material to store electrical energy in an electrical field) and the mean free relaxation time of the material (which is directly proportional to conductivity) i.e. the higher the electron density and lower the effective electron mass, the lower the free relaxation time.[14] However, the thin films remain optically transparent in the visible region since the conduction band is unaltered. The number of and depth of the interference fringes is a function of film thickness which is a consequence of a thickness variation across a film. Interference fringes can also be present as a result of multiple reflections that occur at the interfaces between the air and the thin film, the thin film and the substrate and the barrier coating and glass of the substrate.

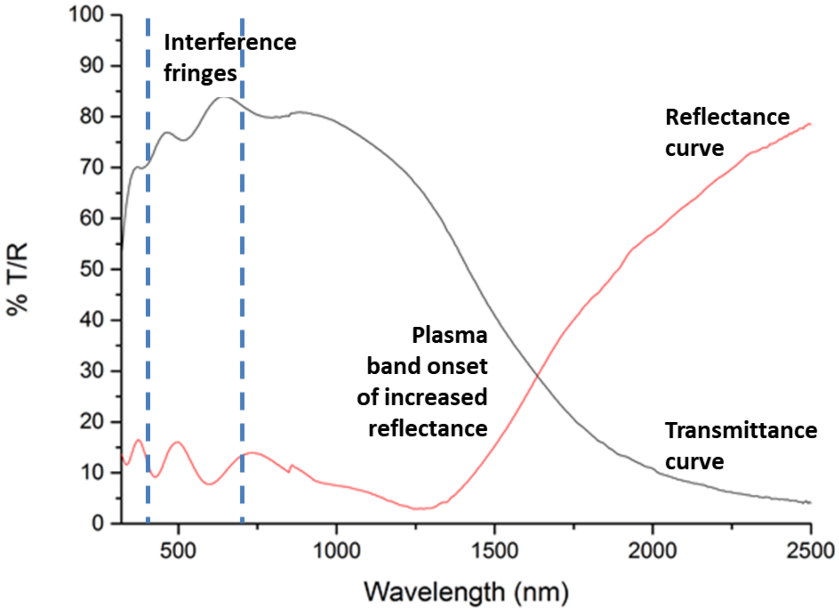

Fig. 1.1. A UV vis spectra showing some characteristics seen in thin films.

1.1.1 Band gaps

The band gap arises from the splitting and overlapping of energy levels when atoms come close together forming the valence and conduction bands. The band gap energy, E_g, is the energy required (provided by a photon) for electrons to flow from the valence band maximum (VBM) to the conduction band minimum (CBM). Typical values for different materials are given in Table 1.1. Several factors affect the band gap of semiconductors.[22] A large band gap is a feature of small interatomic spacing and large differences of electronegativity.[23, 24] The hybridization of orbitals and most notably, doping, also have measurable effects on the band gap.

Table 1.1. The band gap energies for different materials.

Type of material	Band gap energy /eV
metal	<0.3
semiconductor	<4
insulator	4-12

Semiconductors can be one of two types: direct band gap or indirect band gap (Fig. 1.2). In a direct band gap semiconductor the VBM and the CBM have the same momenta (the highest and lowest energy points of the valence and conduction bands respectively line up vertically) but this is not true for indirect band gap semiconductors, such as silicon. However, conservation of momentum is a requirement because the electrons from the conduction band must recombine with the holes in the valence band. This recombination could be radiative or non-radiative. The former is required for the material to have optical properties. In indirect band gap semiconductors, the recombination requires phonons, vibrations of the crystal lattice.[25] However, indirect semiconductors have poor optical properties because the probability of interaction between electrons and phonons is low resulting in a lower rate of radiative emission.

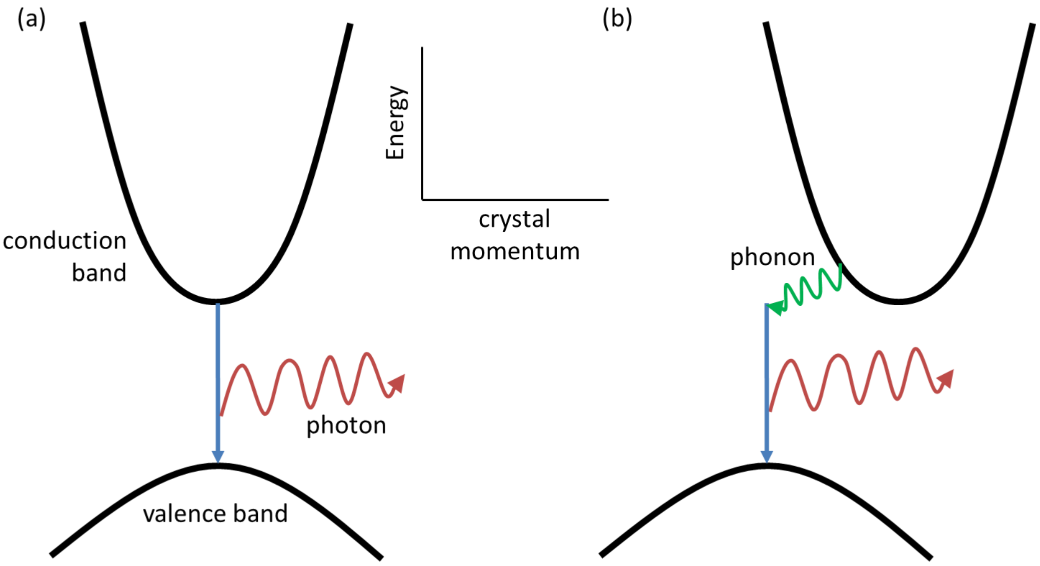

Fig. 1.2. The electronic band structure of (a) direct band gap and (b) indirect band gap semiconductors. Crystal momentum is a momentum-like vector that refers to the electrons in the lattice.

1.1.1.1 Electronegativity

It is not unreasonable to assume that the band gap of a semiconductor or insulator is a function of the difference in electronegativities of the anion and cation in a binary compound. The movement of electrons from the valence band (mostly orbitals of the anion) to the conduction band (mostly orbitals of the cation) would therefore be expected to be affected by the relative electronegativities of the two elements. For example, a smaller difference in electronegativities would presumably produce a smaller band gap. The Pauling scale of electronegativities is not based on individual atoms but on the dissociation energies (D), in electronvolts, of chemical bonds between two atoms (A and B) in the gaseous state and is defined by equation 1.1.[26]

$$|\chi_A - \chi_B| = 0.102\{D(A-B) - \frac{1}{2}[D(A-A) + D(B-B)]\}^{1/2} \qquad \textbf{(Eq. 1.1)}$$

However, the differences in Pauling electronegativities have been used to calculate the band gaps of a number of binary oxides[27] but this does not allow consideration of the degree of covalency found in some oxides, e.g., ZnO and CdO. Therefore, the newer concept of optical electronegativity, which is based on electron promotion in the solid state, is a more realistic measure.[27] What is apparent is the electronegative behaviour of oxygen is highly influenced by the polarising ability of the cation. So is there a correlation between the optical electronegativity and band gap energy? One study comparing experimental band gap data with calculated optical electronegativities found no correlation in TCOs[27] which highlights the multiplicity of factors that affect the band gap.

1.1.1.2 The hybridization of the orbitals

Chalcopyrite semiconductors are made from three elements (ternary compounds) such as $CuAlS_2$, $AgAlS_2$ and $ZnSnP_2$, and have smaller band gaps than binary semiconductors such as ZnO and TiO_2.[28] This anomaly is due to the effect of p-d hybridization, cation electronegativity and structural distortion although the hybridization is seen as the main factor in chalcopyrites made from group I-III-VI_2 elements but not those consisting of elements of group II-IV-V_2 where cation electronegativity is the dominant factor.[28] The study by Mishra and Ganguli shows that d-electrons contribute significantly to a reduction in the band gap through p-d hybridization which arises from the overlap of the p-orbital (from the anion) and d-orbital (from the metal, i.e. Cu or Ag or Zn) that exhibit the same symmetry.[28] This leads to the formation of a lower bonding state attributed to the lower energy cation d-states and an antibonding state, which is at the top of the valence band produced by the higher energy anion p-states. According to perturbation theory, states adopting the same symmetry will repel each other by an amount inversely proportional to the energy difference between the two states.[28] Hence, the reduction in the band gap is a consequence of the repulsion between the p-states and the d-states that have the same symmetry, pushing up the VBM.

In general, the band gap is expected to decrease as a function of an increase in lattice parameters however, there are instances, as in $CuAlS_2$ and $AgAlS_2$ (S could also be replaced with Se) where this is not the case. This has been attributed to p-d hybridisation (the repulsion in Cu chalcopyrites is much larger because of the shallower d-orbital energy) and the fact that Ag is much larger than Cu which means that the anion in Ag chalcopyrite is further away from the Ag than the group III cation. The effect is a lowering of the VBM.[29]

1.1.1.3 Doping

Other factors can also cause light absorptions in the TCO, such as defects in the band gap which arise from imperfections in the structure.[30] Fig. 1.3 shows the different forms of defects commonly found in the crystal lattice: vacancies (sometimes referred to as the Schottky defect) are created by the absence of an ion in the ordered lattice; interstitials are atoms that reside within the normal crystal structure where an atom is not usually found; a Frenkel pair arises when an ion moves from its usual position within the lattice to an interstitial space close by thus creating a vacancy and substitutional defects (also known as impurities) arise when an ion or atom (larger, smaller or the same size and isovalent or aliovalent), replaces an ion or atom normally found in the lattice. The aim of doping is to improve conductivity and increase the band gap (Section 1.2).

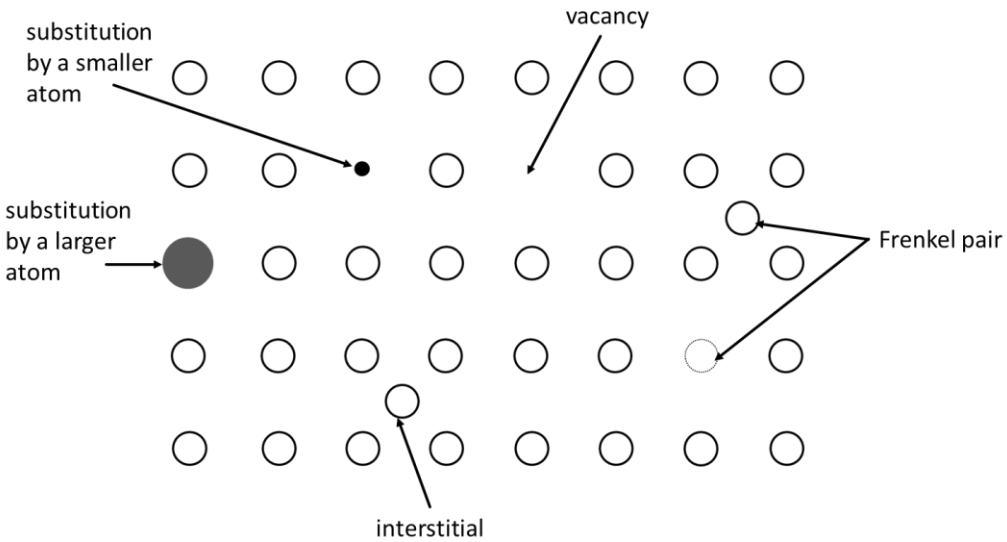

Fig. 1.3. The types of defects found in a crystal lattice.

1.2 Electrical conductivity

Electrical conductivity is one of many properties that depends on the thermal excitation of electrons from the ground state. The Boltzmann distribution describes the number of particles in the excited state at a particular temperature, according to equation (1.2).

$$N_i \propto e^{-\frac{E_i}{kT}} \qquad \textbf{(Eq. 1.2)}$$

Where N_i is the number of particles in a given state, i; E is the energy of a state, k is the Boltzmann constant and T is the temperature. However, the Boltzmann distribution is not appropriate for electrons in a solid as it does not account for the fact that electrons are totally indistinguishable and that they obey Pauli's exclusion principle that two electrons occupying an orbital must have opposite spins. Hence, the Fermi-Dirac distribution gives a better representation, as given in equation (1.3).

$$f(E) = \frac{1}{1+e^{\left[\frac{(E-E_f)}{kT}\right]}} \qquad \textbf{(Eq. 1.3)}$$

The function, *f(E)*, is the fraction of the allowed levels with energy *E* which are occupied. The Fermi level or Fermi energy, E_f, is the cut-off between completely filled levels below E_f and completely empty levels above it. It can also be defined as the maximum energy level an electron can occupy at zero K. For a metal, the Fermi level is within a band which is why they are such good conductors.

In a semiconductor the electrons have to move from the valence band to the conduction band, i.e. the electrons need to gain sufficient energy to overcome the band gap, E_g (Fig. 1.4). If this is achieved in a pure semiconductor at room temperature, then the semiconductor is called an intrinsic semiconductor (Fig. 1.4b). In a pure semiconductor, at any given temperature, the number of electrons excited into the conduction band would be equal to the number of holes left behind in the valence band. Hence, the Fermi level is placed half-way in the band gap. However, the conduction of semiconductors can be increased by doping in which case the semiconductor is called extrinsic, and can be n- or p-type if the doped atom is of greater or lower valency than the host atom, respectively. The Fermi level in extrinsic semiconductors moves away from its ideal mid band gap position: it is closer to the conduction band in n-type and moves down to the valence band in p-type (Section 1.3).

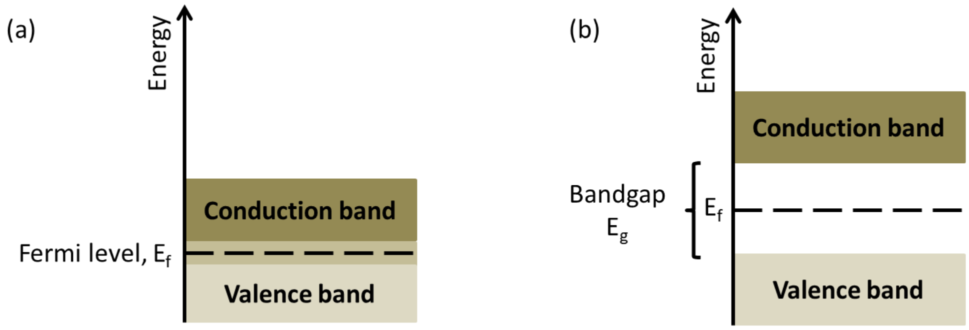

Fig. 1.4. Energy band gaps and the Fermi level in a (a) metal and (b) pure semiconductor.

In intrinsic semiconductors, conduction has long been attributed to the presence of unintentionally introduced donor centres (native defects) due to metallic interstitials or oxygen vacancies that produce donor levels below the conduction band. The premise behind this is based on the fact that the oxide ion is smaller than the cations however, to consider oxygen vacancies as the primary cause of conductivity is still very much contentious.[31] Density-functional theory (DFT) has been used to calculate the energies required to explain the mobility of the electrons. However, it must be noted that these calculations make a number of assumptions including that the calculations are only valid at zero K.[31] The conductivity of the TCO, ZnO, has been investigated using DFT. According to DFT, the 0/+2 transition takes place as the Fermi level increases. However, calculations and experimental data suggest that the donor level is deep, well below the conduction band. This suggests that oxygen vacancies are not the main cause of conduction in TCOs.[32, 33] The role of metallic interstitials in the conductivity of TCOs at room temperature, based on experimental and theoretical calculations, has largely been dismissed due to the unlikelihood that such interstitials are present in sufficient concentrations or are unstable.[31]

Hydrogen has also been put forward as a unintentional donor.[31] In n-type semiconductors (section 1.3), where the Fermi level is just below the conduction band, the hydrogen acts as a compensating acceptor. Thus, the hydrogen would counteract the conducting properties of the semiconductor. However, DFT calculations based on ZnO have shown that interstitial hydrogen could also act as a donor in n-type semiconductors because it can transit between -1 and +1, with no neutral state.[31] Therefore, hydrogen could play an important role in the conductivity of ZnO, as observed when hydrogen diffuses into ZnO.[31] Since hydrogen is an unintentional impurity in the formation of almost all TCOs it would not be possible to assess if it is a dominant player in conductivity. The more likely scenario is that a combination of impurities, native defects and deliberate doping are accountable for the conductivity of TCOs.[31, 34]

1.3 n- and p- type semiconductors

Doping produces extrinsic semiconductors. The objective of doping is to increase the carrier concentration in order to achieve greater conductivity. Extrinsic semiconductors can be n- or p-type depending on whether the majority charge carrier is negative or positive, respectively; these semiconductors are produced by doping the TCO with an atom with a greater valency (donor impurity) or lower valency (acceptor impurity), respectively, than the atoms in the lattice (Fig. 1.5).

Tin doped indium oxide (ITO) produces an n-type semiconductor because indium, a group III element, is doped with Sn, a group IV element. In n-type semiconductors, the electrons are the majority charge carriers because visible photons can excite electrons from the high lying donor level to the conduction band. In p-type semiconductors a group IV element, for example, would be doped with a group III element resulting in holes. These holes are the majority charge carriers since the visible photons have enough energy to excite holes from the low-lying acceptor band to the valence band.[18]

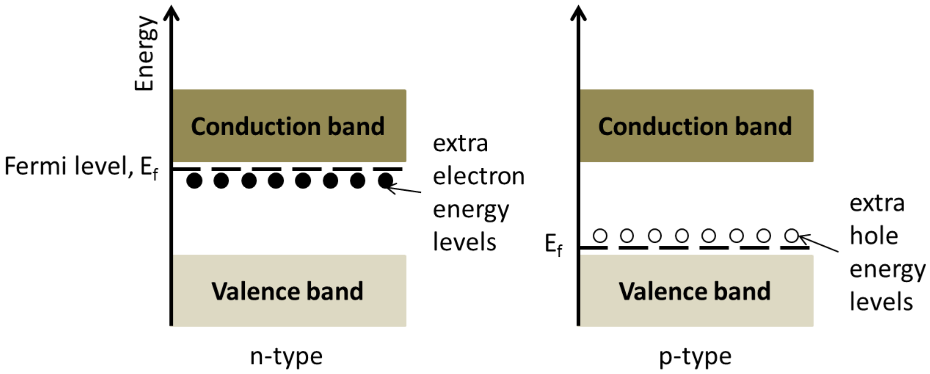

Fig. 1.5. Energy band gaps in n- and p-type semiconductors.

In an intrinsic semiconductor, the concentration of electrons and holes are equal to the intrinsic concentration, i.e., $n = p = n_i$, making the material electrically neutral. n and p can be changed by adding an n-type or p-type impurity, respectively. However, the product of n and p is a constant independent of the doping type and the doping level, as shown in equation 1.4.

$$np = n_i^2 \qquad \textbf{(Eq. 1.4)}$$

This relationship is called the mass-action law. To illustrate this, without the involvement of thermodynamic analyses, let's consider increasing the number of donors by a large factor, N. This would mean that the number of free electrons will increase by a factor N to Nn_i and the recombination rate with holes will also increase by a factor of N. Hence, the density of holes will decrease from n_i to n_i/N and the number of electrons will decrease from Nn_i to $Nn_i - n_i/N$. The product of electron concentration and hole concentration is given in equation 1.5.

$$(Nn_i - n_i/N)(n_i/N) = n_i^2(1 - 1/N^2) \approx n_i^2 \qquad \textbf{(Eq. 1.5)}$$

There are three general considerations of doping:[6]

- the dopant is soluble in the lattice structure;
- the shallowness of the dopant level since deep donor levels require more energy to generate the charge carriers;
- the dopant should not act as a compensatory acceptor (a low energy electron killing defect).

Furthermore, this has to be achieved without impairing the transparent properties of the film. Adding a dopant to the oxide can widen or narrow the band gap particularly at higher doping concentrations.[7, 35] The increase in the band gap is called the Moss-Burstein effect and is due to the Fermi level moving into the conduction band caused by an increase in the carrier concentration. The electrons can only be excited to levels above the Fermi level because all the states below this are occupied.[6] Although, in some cases increasing dopant concentration can increase the band gap there is a limit after which conductivity becomes compromised due to a deterioration in film structure resulting in the reduced mobility of the free electrons.[23, 36] Conversely, band gap narrowing has also been observed after doping accompanied by significant increases in conductivity and mobility of charge carriers.[37, 38] Band gap narrowing is still poorly understood.[35] However, in heavily doped films, the most likely cause is the creation of energy levels near the conduction band and the valance band by shallow level donor impurities and shallow acceptor level impurities, respectively. This phenomenon is called band gap renormalisation. Several attempts have been made to model the narrowing, more recently, from data on doped ZnO films.[35]

1.3.1 n-type TCOs

The majority of TCOs in use are n-type semiconductors.[18] Most have been based on the binary oxides of Sn, In, Zn and Cd but two-binary system oxides (e.g., ZnO-SnO_2) and ternary (e.g., $ZnSnO_3$) or quaternary oxides (e.g., Cu_2ZnGeO_4) have also been made. All types have also then been doped with a diverse range of elements or compounds.[15, 39] Highly conducting and transparent films, with free electron concentrations of 10^{20} cm^{-3} or greater, can be made without doping but such films are not stable at high temperature (Table 1.2).[15]

Table 1.2. Band structures of n-type binary oxides.[6, 7, 8]

Oxide	**Lattice structure**	**minimum band gap /eV**
SnO_2	rutile	3.6 direct
In_2O_3	bixbyite	2.9 direct
ZnO	wurzite	3.3 direct
Ga_2O_3	complex	4.5-4.9 direct
CdO	rock-salt	0.8 indirect; 2.3 direct

Metal cation doping has been successful in increasing electrical conductivity particularly using dopants with an electronic configuration of $(n\text{-}1)d^{10}(n)s^0$ (where n, the quantum number, is ≥ 5).[40] The doping of In_2O_3 with Sn to form ITO significantly reduced the resistivity from the order of 10^{-3} Ω cm to 10^{-5} Ω cm.[15, 41] Doping of binary compounds using metallic dopants can increase the density of conducting electrons because the dopants act as electron donors. In terms of carrier concentrations, compare 2.22×10^{19} cm^{-3} measured in In_2O_3 with 2.5×10^{21} cm^{-3} in ITO. Fluorine has been widely used as a non-metallic dopant with oxides of Sn, Zn and In because it increases the conductivity of the film by acting as a donor since F^- replaces the O^{2-} ion.[14]

1.3.2 p-type TCOs

p-Type oxides are essential in the production of complementary metal-oxide semiconductors (CMOS). Nickel oxide, NiO, was the first reported p-type TCO but transmittance of the films was only 40%, resistivity was 1.4×10^{-1} Ω cm and the films were stable for use at temperatures below 100 °C.[42] A few years later, in 1997, the discovery of a highly transparent p-type TCO was announced.[43] The thin film in question consisted of copper aluminium oxide, $CuAlO_2$, with a maximum transmittance in the visible range of ~60%, however, the resistivity was about 1 Ω cm which was 3-4 orders of magnitude greater than the n-type ITO, one of the better TCOs used in industry.[44] Since then, several different methods have been used to produce Cu-Al-O p-type thin films, including sputtering, chemical vapour deposition, sol-gel deposition and chemical solution.[45] Table 1.3 summarises the electrical and optical properties of $CuAlO_2$ films deposited by some of these methods. It is worth noting that some studies have produced films but have not published a complete characterisation.[46, 47, 48] The table highlights that while transmittance in the visible range can be achieved at values 80% or above, the resistivity of all the films is significantly greater than desired for commercial applications.

Table 1.3. Optical and electrical properties of Cu-Al-O p-type thin films.

Method of deposition	**Temperature used for deposition /°C**	**Resistivity / Ω cm**	**Carrier concentration /cm^{-3}**	**% transmittance over visible range (390 – 700 nm)**	**Band gap /eV**
Laser ablation (pulse laser)[44]	700	10.5	1.3×10^{17}	27-57	3.50
PE-MOCVD[49]	745	0.50	1.8×10^{19}	22-42	3.75
Radio frequency Magnetron sputtering[50]	22 (annealed at 950)	90.90	3.7×10^{16}	65-70	4.7
DC sputtering[51]	200	4.55	4.4×10^{17}	30-92	3.75
Chemical solution (CS)[52]	400 (annealed at 900 – 1000)	152	6.7×10^{16}	≤ 70	3.48
Sol-gel (dip coating)[45]	100-120	250	not given	80-90	3.94
Sol-gel (spin-on)[53]	400	0.42	5.4×10^{18}	25-60	3.75

Computational studies using DFT theory has been adopted to explore TCOs that have the potential to be p-type semiconductors, including SnO.[54, 55]

1.3.3 p-n junctions

The use of n-type TCOs for making conducting films is well established but to make circuit components such as diodes, a material made of p- and n-type semiconductors is needed; only then will invisible circuits become a real possibility.[17] Therefore, the current goal is to fabricate a transparent p-n junction which transmits visible light and generates electricity by absorption of UV.[18] n-Type and p-type semiconductors are conducting but the interesting part of the p-n junction is the interface where there is no conduction. However, manipulating the voltage of the two types allows for a one-way flow of current. The electrons from the n-type region diffuse to the p-type region filling the holes and leaving behind positive charged ions (donors). Similarly holes in the p-type region move to the n-type region leaving behind negatively charged ions. This results in the formation of a depletion region that acts as a barrier to the further diffusion of electrons since the negatively charged ions in the p-type region repels electrons from the n-type region (Fig. 1.6a). To overcome the barrier, a potential difference, called the barrier potential, is applied in order to bias the junction. A forward bias is produced when the n-type region conduction band is raised higher than the p-type region conduction band (Fig. 1.6b). Hence, the electrons that have diffused across are at a higher energy level than the holes in the p-type region. These electrons combine with the holes and continue to move along by jumping from hole to hole. This results in a continuous forward current from right to left across the junction.[56]

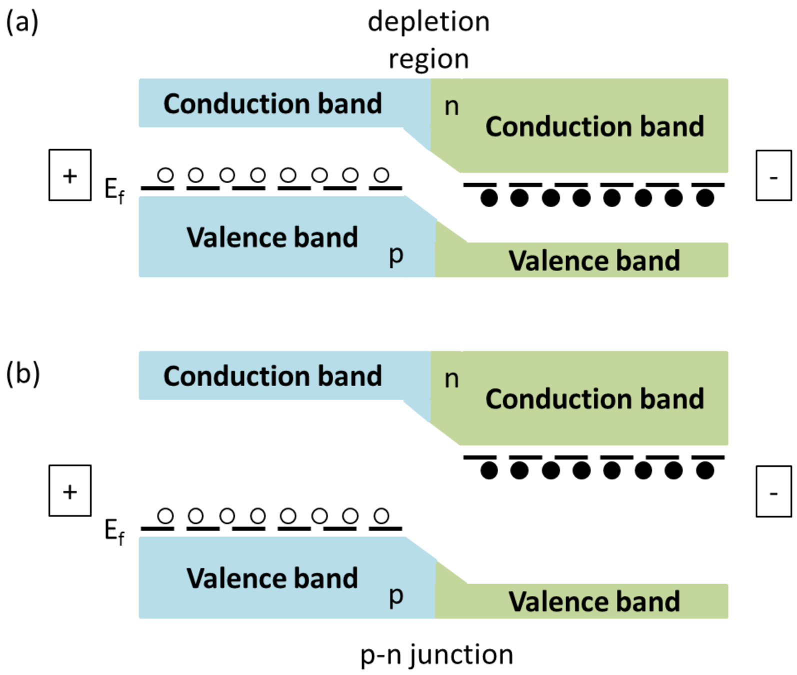

Fig. 1.6. (a) p-n Junction at equilibrium (unbiased) (b) Forward bias conduction in a p-n junction.

While n-type TCOs thin films have been well characterised, the same is not true of their counterpart p-type films, notably because so few reports of their fabrication are known. Of these, the most well-known is ZnO which can exhibit p-type conductivity when deposited under certain conditions or doped with N, Sb or As.[57] However, it is not easy to manufacture and decays too rapidly to be of any use.[57, 58] In contrast, SnO is a more promising p-type semiconductor which can form a p-n junction with the n-type SnO_2 thin film, with features favourable in their use as a p-n diode.[40, 58] Clearly, the formation of TCO p-n junctions is an area requiring further research.

1.4 Zinc oxide

Zinc oxide is a wide band gap (3.37 eV) n-type semiconductor. ZnO has three possible crystal structures: hexagonal wurtzite, cubic zinc blende or cubic rock salt. Under ambient conditions, the wurtzite structure is the most thermodynamically stable (Fig. 1.7). The zinc blende symmetry is only stable when grown on cubic substrates. The wurtzite structure can be transformed into the rock salt structure under high pressures.[59] However, under decompression, the rock salt does not revert to the wurtzite structure at room temperature, only at elevated temperatures. The wurtzite structure belongs to space group C_{6v}^{4} with unit cell constants $a = b = 3.249$ Å and $c = 5.207$ Å, where $\alpha = \beta = 90^\circ$ and $\gamma = 120^\circ$.[59, 60] Each zinc atom is surrounded by four oxygen atoms at the corners of a tetrahedron and vice versa, adopting a hexagonal closed pack structure. The ionic radii for Zn^{2+} and O^{2-} are 0.74 Å and 1.24 Å, respectively.

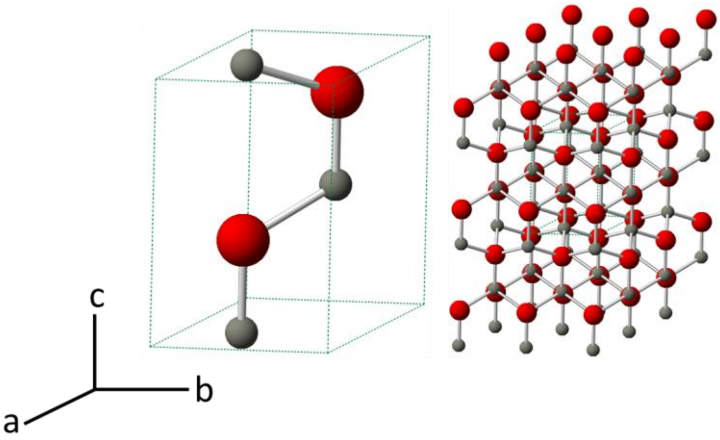

Fig. 1.7. The unit cell of the wurtzite crystal structure and the wurtzite lattice of ZnO (grey = Zn^{2+} and red = O^{2-}).

The band structure calculations for ZnO have been performed by several research groups using the local density approximation (LDA).[61, 62] The valance band consists of 6 bands between −5 to zero eV and two low energy (-20 eV) core-like states representing O 2p and O 2s bonding states, respectively. In the conduction band, the first two states are strongly Zn localised and correspond to empty Zn 3s levels while the higher conduction bands are free-electron-like.

Electrical conductivities comparable to ITO are achieved when the ZnO lattice is doped with trivalent elements. Minami[15] summarised, from the past thirty years, resistivity values of impurity doped binary compound TCO films and found that the minimum resistivity of impurity doped ZnO films is still decreasing whereas SnO_2 and In_2O_3 films have essentially remained the same. Hence, ZnO is a promising alternative to the "industry champion" ITO having the added benefit of being inexpensive, non-toxic, and abundant.[63]

1.5 Tin(IV) oxide

Tin(IV) oxide (stannic oxide), SnO_2, is probably the simplest of the TCOs and the most attractive since tin is less expensive and more abundant than indium.[6] Furthermore, SnO_2 is environmentally stable and has good mechanical strength.[64] Most architectural glass on building windows use tin-oxide based TCOs.[65] It is a wide band gap n-type semiconductor with a direct value of 3.6 eV. The main ore of tin is cassiterite in which the SnO_2 adopts a tetragonal rutile structure with space group D_{4h}^{14} ($P4_2/mnm$) (Fig. 1.8).[66] The unit cell contains two tin atoms and four oxygen atoms with lattice constants $a = b = 4.737$ Å and $c = 3.185$ Å, where $\alpha = \beta = \gamma = 90^{\circ}$.[65, 66] Each tin atom is surrounded by six oxygen atoms which are coordinated in an octahedral manner and each oxygen atom is neighboured by three tin atoms, essentially forming an equilateral triangle. Thus the structure has 6:3 coordination. The ionic radii for Sn^{4+} and O^{2-} are 0.69 Å and 1.24 Å, respectively.

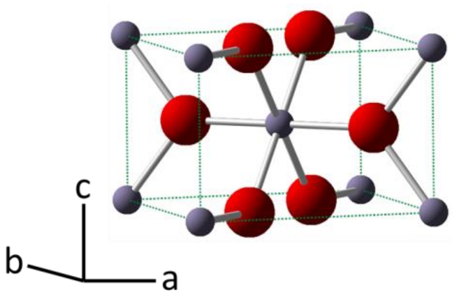

Fig. 1.8. The crystal structure of cassiterite SnO_2 (grey = Sn^{4+} and red = O^{2-}).

Stoichiometric tin(IV) oxide is in fact an insulator; it is the presence of defects in the lattice that contributes to the electrical properties. Hence, in undoped SnO_2 conductivity could arise from either oxygen vacancies, V_o, or interstitial tin atoms, Sn_i, behaving as donors, as shown in (A) and (B).[66]

(A) $SnO_2 \leftrightarrow Sn_{Sn}^{4+} + O_o^{2-} + V_o^{2-} + \frac{1}{2}O_2$
(B) $SnO_2 \leftrightarrow Sn_i^{4+} + O_{2(g)}$

It has long been accepted that the transparent conductivity arises from a large concentration of V_o due to the existence of shallow donor levels near the conduction band.[31, 67] However, in more recent years this has been questioned as vacancies usually form deep (i.e. non-conductive) levels in the band gap. Kiliç and Zunger[67] carried out first-principles calculations to investigate this concept. They found that Sn_i actually plays a significant role in undoped SnO_2, concluding the following statements:

- Sn_i produces a donor level *inside* the conduction band allowing instant donor ionization and conductivity; in contrast to the outer electrons of the V_o which produce a level inside the band gap.

- Sn_i exists in significant quantities as it has a very low formation energy (electrons around the Sn orbitals are weakly bound) and is stable due to the multivalence character of tin. Furthermore, V_o become more favourable in the presence of Sn_i due to the strong inter-defect interaction between them hence explaining the resultant oxygen deficiency and hence the non-stoichiometric nature of SnO_2.

- A characteristic of the band structure of SnO_2 is the absence of inter-conduction-band absorption resulting in a large internal gap in the conduction band, eliminating optical transitions in the visible range.

Singh *et al.* reported that the above conclusions are unlikely and that the incorporation of hydrogen contributes to intrinsic SnO_2 conduction.[68] As well as occupying interstitial sites, hydrogen may also replace oxygen in the SnO_2 lattice, forming multicentre bonds with the three neighbouring tin atoms. Interstitial hydrogen has a low formation energy and is reported to be a shallow donor (Section 1.2) hence increasing the number of charge carriers.[68]

1.6 Optical and/or electronic applications

Optical and/or electronic applications mainly include photovoltaics (PV), flat-panel and touch screen displays, light emitting diodes, heat mirrors and gas sensing. Comprehensive reviews on the applications of TCOs are available.

1.6.1 Photovoltaics

In photovoltaics (PV) the TCO has the role of the front electrode or contact which allows solar radiation to be transmitted to the absorber layer(s) below and to conduct (extract) the electrons to the external circuit. A range of TCOs, including, ITO, FTO and ZnO, are in current use in the production of PV depending on the cell type, ranging from amorphous Si to copper indium gallium selenide (CIGS), CdTe, dye-sensitized, organic and quantum-dot solar cells.[69] The typical efficiencies range from 5 to 15% although efficiencies of 20% and greater have been reported under laboratory conditions.[70] Silicon based PV are the most widely used in which the TCO employed is ITO which apart from requiring a high deposition temperature is also somewhat costly. The future development of PV is focusing on tuning alternative TCOs, in terms of morphology and work function, to improve efficiency.[34, 69]

1.6.2 Flat panel displays

ITO is almost exclusively used as the transparent electrode in flat panel displays, in both rigid and flexible applications.[19] However, efforts are underway in using aluminium doped zinc oxide (AZO) as an alternative.[71]

1.6.3. Heat mirrors

Heat mirrors are thin films that are used to reflect or reduce the transmission of infrared radiation and transmit only visible light.[72] For an ideal heat mirror, the transmittance in the visible (400-700 nm) should be 100% and reflectance 0% and in the infrared region (>700 nm) the converse would be expected (Fig. 1.9). However, a compromise or a trade-off is a more realistic goal in the production of thin films, particularly as infrared reflectance increases with increasing conductivity. However, film thickness is correlated with free carrier concentration but as thickness increases the transmittance decreases and if film thickness is too low the infrared reflectivity is degraded.[72] The sheet resistance of commercial heat mirrors is 8-15 $\Omega\ \square^{-1}$.[73] Applications include low-emissive (low-e) windows that aid temperature control and hence energy efficiency.[74] If the heat mirror is needed to gain solar energy for heating in winter then the optimum heat mirror would transmit visible and infrared (the plasma band onset of increased reflectance or plasma edge) at an approximate wavelength of 2000 nm (blue line) but if all infrared is to be reflected, for cooling applications, then the plasma edge is at an approximate wavelength of 750 nm (red line).[72] Multi-layered thin film dielectric/metal/dielectric (DMD) materials and TCOs including ITOs have been used to produce heat mirrors. DMD materials have mainly used Ag films sandwiched between layers of dielectrics such as TiO_2, WO_3 and ZnS;[75, 76] DMDs have the advantage over doped TCO single layered films in broad wavelength tunability[77] but obviously lacking the conductivity sought after in TCOs. Layered TCO films such as TiO_2/ITO have optical properties more suited to heat mirrors; layering increased the reflectance by ~45 % and the sheet resistance was about ~20 $\Omega\ \square^{-1}$.[73]

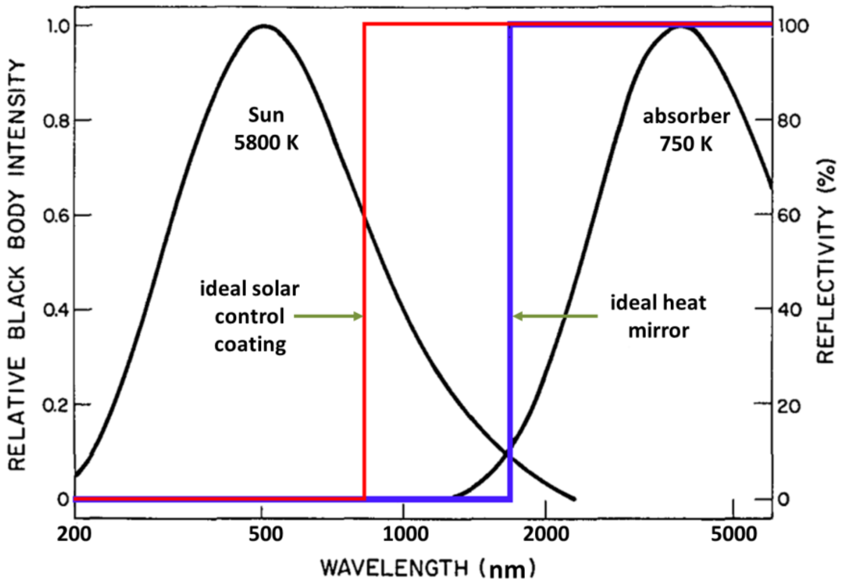

Fig. 1.9. Normalised spectra for the radiation from the Sun with a blackbody temperature of 5800 K and for the radiation emitted by a black absorber heated to 750 K. Also shown are the spectra for the idealised low emissivity heat mirror (blue line) and solar control coating (red line); adapted from Fan and Bachner.[1]

1.6.4 Gas sensors

Gas sensing technologies can be broadly classified into electrochemical, optical and chemoresistive.[60] While optical sensing TCOs has received some interest, the affordability and simplicity in manufacture, have accounted for the widespread use of chemoresistive TCO based sensors.[78] The TCO gas sensor works on the principle that a measurable change in the resistivity or electrical conductivity occurs on exposure of the thin film to a target gas which acts as either a donor or an acceptor of electrons. The most common solid state metal oxide gas sensors are based on the materials: SnO_2, TiO_2, Cr_2O_3 and WO_3 with sensitivities as low as ppm and even ppb for some gases. The limitations of using TCOs in gas sensing is the lack of specificity which is particularly troublesome when encountering a mixture of gases which contain oxidising and reducing species, and prolonged response times and the return of the signal to the base line. Added to this, the best performance is usually achieved at elevated temperatures (300-500 °C) which is not ideal for most situations.

1.7 Thin film deposition routes

A variety of methods have been used to deposit thin films based on wet chemical[79, 80], physical vapour deposition (PVD)[81, 82] and chemical vapour deposition (CVD)[12] (Fig. 1.10).

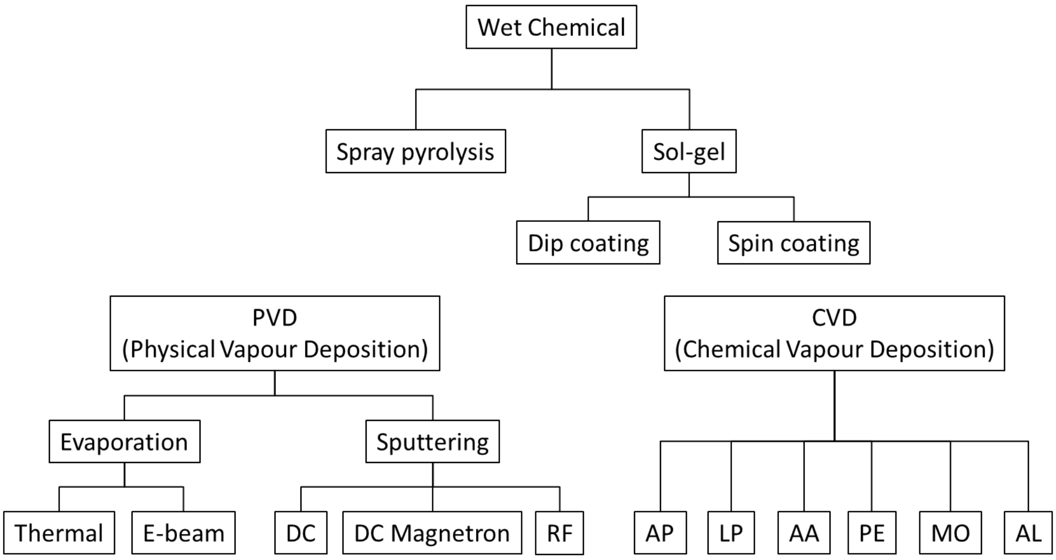

Fig. 1.10. The main methods of wet chemical, and physical and chemical vapour deposition of thin films. DC, direct current; RF, radio frequency; AP, atmospheric pressure; LP, low pressure; AA, aerosol assisted; PE, plasma enhanced; MO, metal organic; AL, atomic layer.

1.7.1 Wet chemical

Wet chemical routes to film deposition generally involve the desired material species to be dispersed in a liquid medium *via* the reaction of the precursors. The most common wet chemical deposition methods are spray and sol-gel deposition.

1.7.1.1 Spray pyrolysis

Spray pyrolysis deposits thin films by spraying a solution onto a heated substrate, generating droplets, which in turn thermally decompose. It is important that the chosen chemical reactants produce by-products that are volatile at the temperature needed for the deposition of the desired film.[79] Hence, the film properties, such as film crystallinity and morphology, are strongly influenced by the choice of starting materials. Atomisation is achieved by applying pressure, by using a nebuliser, ultrasonic or electrostatic methods. The growth kinetics, and in turn the quality of the film, depend on which method is used as all of them have different effects on the droplet size distribution and velocity, and the rate of atomisation.[83] Viguié and Spitz[2] classified chemical spray deposition processes according to the type of reaction as a function of temperature (Fig 1.11). They are as follows:

- *Process 1*: a droplet lands on the heated substrate; solvent evaporates leaving behind a solid, which decomposes.

- *Process 2*: the solvent evaporates before the droplet reaches the surface; solid impinges upon the surface where decomposition occurs.

- *Process 3*: the solvent vaporises as the droplet approaches the substrate; the solid then melts and vaporises. Vapour diffuses to the substrate to undergo a heterogeneous reaction (they refer to this process as true CVD).

- *Process 4*: the entire reaction takes place in the vapour state.

Most spray pyrolysis depositions are type 1 or 2.[79]

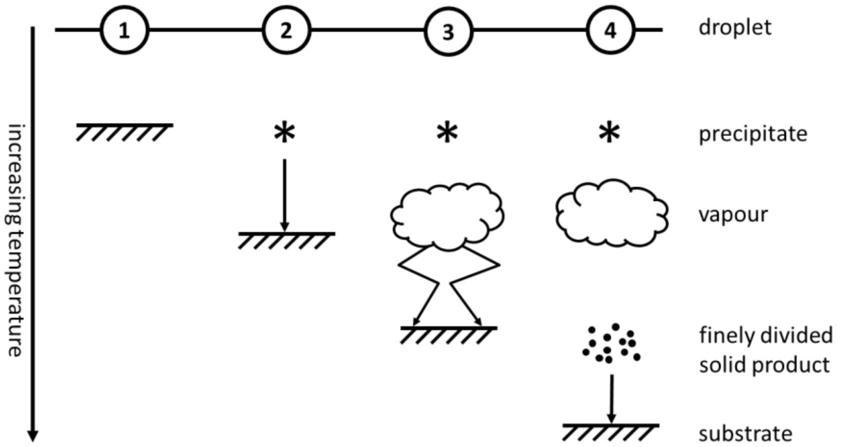

Fig. 1.11. Description of the chemical spray deposition processes as a function of increasing substrate temperature. Adapted from Viguié and Spitz.[2]

1.7.1.2 Sol-gel

Sol-gel usually involves the reaction of chemical precursors to form a colloidal solution (sol), which agglomerates together to form a continuous network (gel) of the desired material for film deposition.[80] The sol can spread over a substrate by different techniques. The chemical precursors that make up the sol have a decisive role in which deposition method is ideal, having a direct influence on film properties including structural, optical and mechanical properties.[83] The two most common techniques are:

- *Dip-coating:* a clean substrate is dipped into a precursor solution and then removed at a particular speed under controlled temperature and atmospheric conditions. Films deposited *via* this method are usually X-ray amorphous and require an annealing step to achieve crystallisation.

- *Spin-coating:* the precursor solution is dropped onto a flat substrate. The substrate is then rotated at high speed allowing the solution to spread across the surface, covering the substrate. Airflow removes the solvent leaving behind a dry solid layer.

Both these processes are sensitive to environmental conditions i.e. temperature and humidity.

1.7.2 Physical vapour deposition

Physical vapour deposition (PVD) is essentially a vaporisation coating technique (also referred to as a 'line of sight' method) whereby the solid material is first vaporised by evaporation or sublimation before transporting, under vacuum, into a chamber where it then deposits onto the substrate without chemically changing although reactions may occur with other gases present.[11] In most applications, the main coating is usually the precursor solid. The aim is to produce a thin coating which has additional properties such as reduced friction, improved stability, etc.

However, the method requires expensive high vacuum equipment. PVD uses physical processes such as heating or sputtering (Fig. 1.12):

- *Evaporative deposition:* involves heating the precursor by electrical resistance (thermal) or electron bombardment (E-beam). The material vapour then condenses onto the substrate to form a solid layer. The vapours used in thermal evaporation are directional therefore leading to poor coverage. Rate of growth can be monitored *in situ* using a number of methods including mass spectroscopy, electron induced emission spectroscopy and glow-discharge optical spectroscopy.[84] Defect-free thin films are achieved *via* molecular beam epitaxy (MBE), an evaporative process carried out under ultrahigh vacuum.

- *Sputtering:* uses a plasma as the form of energy to vaporise the desired material for subsequent deposition. The power supply is usually DC for conductive materials or RF for insulators. DC magnetron sputtering uses a closed magnetic field to trap electrons which allows a plasma to be generated at lower pressures which can help reduce costs. The rate of sputtering depends directly on the flux of ions hitting the target, which is itself related to the density of ions in the gas. Therefore, the rate of sputtering increases with increasing the density of ions.[84] DC sputtering is used to produce ITO – one of the most widely used TCO material.[85]

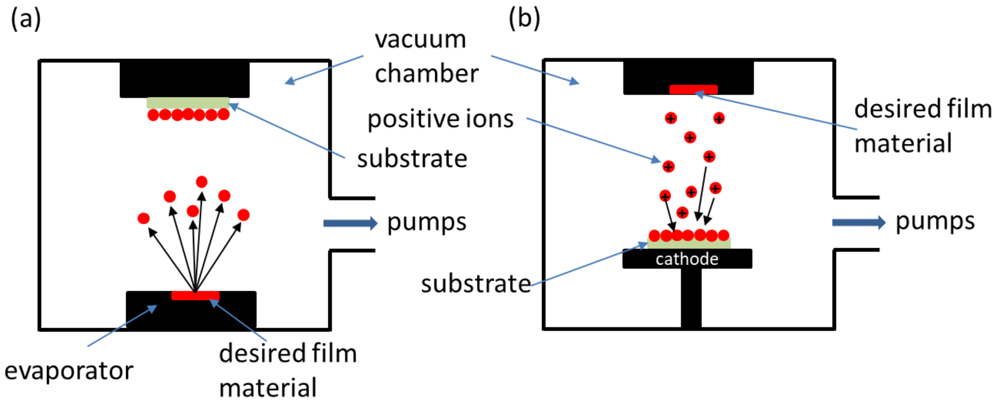

Fig. 1.12. Simplified schematic of the PVD processes showing only the major parts of: (a) evaporative and (b) sputtering.

1.7.3 Chemical vapour deposition

Chemical vapour deposition (CVD) involves the formation of a thin solid film on a substrate material by a chemical reaction of vapour-phase precursors.[86] One of the most widely used commercial TCO, FTO, is deposited *via* this method with a sheet resistance in the range 7-15 Ω $\square^{-1}$ (Pilkington NSG).[87] In CVD, there is the requirement that the precursors are volatile and thermally stable in order to be converted into the gaseous state. CVD requires the delivery of precursors in the gas phase, the transportation of the precursor gas stream to the substrate and the application of energy to cause a reaction. The key steps in a CVD process are (Fig. 1.13):

1. Precursors, in the gas phase, are transported into the deposition chamber using a carrier gas (or a pressure gradient if it is low pressure CVD (LPCVD));
2. Adsorption takes place on the hot surface – a physisorption process;
3. Decomposition reaction of the precursor;
4. Diffusion of atoms across the surface until they reach a strong binding site (chemisorption);
5. Nucleation and film growth;
6. Desorption of the unwanted organic molecules from the surface;
7. Transportation of the waste material to the exhaust.

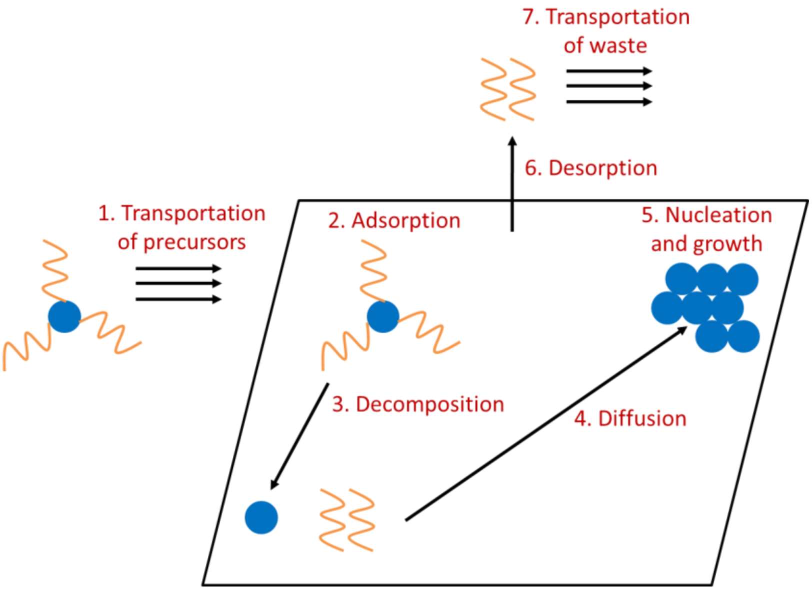

Fig. 1.13. A schematic showing the key stages of the CVD process.

Reactions can be promoted or initiated leading to variations in the method. Six main methods utilising CVD have been identified from the literature (Fig. 1.10), each categorised based on parameters, such as source gases and deposition conditions (temperature and pressure). Conventional CVD uses thermal energy to activate chemical reactions as in atmospheric pressure (AP) and low pressure (LP) CVD. APCVD proceeds *via* a diffusion-limited surface reaction where the rate is determined by the diffusion of the gaseous molecules to the substrate surface which can result in non-uniformities due to variation in gas flow rates. In contrast, LPCVD is a surface reaction limited regime such that although the reactants maybe present in sufficient amounts the rate of surface reactions is limited by temperature and/or availability of surface.

Alternative energy sources such as plasma and light can be used to activate the reactions. Plasma Enhanced (PE) CVD uses electrical energy to produce a glow discharge or plasma that when transferred to the gaseous reactants forms ionised species or radicals which react more readily at a lower activation energy. PECVD has a distinct advantage of allowing reactions to take place at lower temperatures than thermal CVD methods permitting the use of temperature sensitive substrates to be used, although film quality and stoichiometry can be compromised.

Metal-organic CVD utilises metal organic rather than inorganic precursors used typically in conventional CVD, which contain a direct metal-carbon bond (sigma or pi). However, in more recent years, the definition of MOCVD has broadened to include precursors containing metal-oxygen or metal-nitrogen bonds, and even metal hydrides.[86] The organic based precursors are more labile which allows the reactions to take place at relatively lower temperatures.[88]

Atomic layer CVD (ALD) (also known as atomic layer epitaxy (ALE)) proceeds by alternating self-limiting surface reactions called ‘half-reactions’. Pulses of precursors are transported into the reaction chamber under vacuum intermitted with periods of purging with inert gas or vacuum to limit further reactions. The process usually produces a monolayer at the surface and repeated cycles build up to the desired thickness.[89]

Aerosol assisted CVD (AACVD) improved upon the conventional use of heated bubblers in CVD which relied on the evaporation of the precursor by bubbling in a carrier gas.[86] Instead, AACVD generates an aerosol of a solution of the precursors that is transported with the aid of inert or reactive carrier gas.[14] The main advantage of this method is that the precursors do not have to be volatile but only soluble in any solvent that can be aerosolised.[14]

Other than the pressure, the form of energy supplied to initiate the chemical reaction and the method used to introduce the precursor into the gas phase, other parameters of importance differentiating the methods include the number of precursors required (single source or dual-/multi-source system) and the type of reactor (hot or cold walled).

Consistency in film thickness and conformity, high deposition rates and control of crystal structure makes CVD the preferred process over PVD for large scale applications.[12] The advantages and disadvantages of wet chemical, PVD and CVD are summarised in Table 1.4.

Table 1.4. The important advantages and disadvantages of wet chemical,[9] PVD[10] and CVD[11, 12].

	Advantages	Disadvantages
Wet Chemical	• Low cost and non-vacuum technique; • Easy control of composition; • Produce multi-component materials of high purity; • Depositions at moderate temperatures (100-500°C);	• Possible oxidation of precursors; • Large amounts of solvent needed; • Difficulty in controlling particle size and size distribution; • Large volume shrinkage of the film during drying; • Difficulty with growth temperature determination; • Spray nozzle may become cluttered; • Film quality may depend on droplet size and spray nozzle; • High precursor costs;
PVD	• A wide range of substrates can be coated; • Coatings are hard; • Can generate highly crystalline defect-free thin films (MBE);	• Requires a line-of-sight between source and substrate; the film will not deposit consistently on any surface that isn't; • Low deposition rates; • A high vacuum is required; • Relatively higher costs as well as use of complex machines requiring skilled operators; • Poor adhesion – atoms are not always firmly chemically bound to the substrate;
CVD	• Films are conformal – the thickness of film is consistent and will follow the contours of the substrate; • a wide variety of materials can be deposited with very high purity; • High deposition rates with good reproducibility; • A high vacuum is usually not needed; • Can use precursors that are difficult to evaporate;	• Precursors need to be volatile and thermally stable which reduce the variety of potential precursors and hence can increase the cost; • Precursors can be highly toxic, explosive or corrosive; • By-products can be hazardous; • Films are deposited at relatively high temperatures which restricts the types of substrates used; • The heating process can put stress on the films deposited leading to mechanical instabilities.

1.7.3.1 Precursor requirements for CVD

The key step in a CVD process is the thermal decomposition of a precursor for film formation, and ideally the ligands associated with the precursor are cleanly lost into the gas phase.[86] It is important to note that the ligands can also fragment and lead to unwanted impurities in the film and therefore it is a good idea to do some studies on the precursor decomposition mechanism using techniques such as gas chromatography mass spectrometry (GC-MS), Fourier transform infrared spectroscopy (FT-IR), and thermogravitational analysis (TGA).[86] When selecting suitable precursors, it is important to keep in mind the following factors:

- *Precursor purity*: precursors with high level of purity will prevent contamination of the thin film;

- *Precursor reactivity*: the precursor needs to react on the substrate surface but not be too reactive that it will react in the vapour phase during film deposition. In liquid injection systems, thermal stability is an important parameter as precursors may decompose in the heated evaporators leading to flow blockage and contamination;

- *Volatility*: It is a CVD requirement for a precursor to be volatile (unless it is AACVD) at a temperature well below that of its decomposition. Lowering the pressure inside the reaction chamber (as with LPCVD) compensates for lower volatility potentially at the cost of a reduction in the growth rate;

- *Stability in air*: precursors are easier to handle and store without the need for specialist equipment and storage, respectively;

- *Toxicity*: low toxicity is favoured, avoiding the need for special procedures during deposition and specialist storage;

- *Synthesis*: the number of synthetic steps should be kept to a minimum and produce at least a few grams of product at a time. The synthesis should easily be able to be scaled up without major problems;

- *Environment and cost*: precursors and waste materials should have minimal toxicity and the cost of the precursors and disposable of waste should ideally allow the production of economically viable films.

1.7.3.2 Thin film growth and morphology

Films produced *via* CVD exist in one of three structural forms: amorphous, epitaxial (single layer or single crystalline) and polycrystalline.[12, 86] The type produced depends on surface diffusion and nucleation during deposition, which in turn are determined by the deposition conditions.

Amorphous means that the crystallisation is completely absent and is generally obtained at low temperatures where there is a high number of adatoms (adsorbed atoms) with low mobility thus preventing nucleation (slow surface diffusion) resulting in the formation of a film consisting of unorientated grains. The lack of grain boundaries makes amorphous films ideal for use in applications such as transistors.[90] Epitaxial films are single layer crystalline films which have lattice spacing that matches that of the substrate. Therefore, for this type of growth it is vital that the substrate is free from defects and contamination. The epitaxial film can be homoepitaxy where the substrate and film are made of the same material or heteroepitaxy where the substrate and film materials are different. In both cases, the single crystalline structure is obtained as a consequence of high temperatures and low growth rates permitting faster surface diffusion resulting in nucleation provided that the surface energy of the interface is lower for the epitaxial orientation than for other orientations. The high temperature as well as a low pressure also facilitates the desorption of impurities. Epitaxial films are favoured for semiconductor and superconductor applications.[91] Polycrystalline films are usually produced at intermediate temperatures and growth rates between those used for amorphous and epitaxial films. The polycrystalline nature of films arises from nucleation of isolated crystals taking place at different sites on the surface that coalesce to form a polycrystalline layer; crystallinity being a function of temperature.

There are three classical growth modes: Frank-van der Merwe (FV: 2-D layer-by layer growth), Volmer-Weber (VW: 3-D island growth) and Stranski-Krastonov (SK) (Fig. 1.14). In FV growth, a new layer is nucleated only after the completion of the layer below hence two-dimensional. This happens because the adatoms are more strongly bound to the substrate rather than each other, hindering the formation of clusters. Diffusion is generally fast and film coverage is atomically smooth and conformal to the substrate. This type of growth usually forms the most crystalline films. In VW growth, the adatom-adatom interaction is stronger than the interaction between the adatom and the surface resulting in cluster or island formation hence three-dimensional. The islands grow and eventually coalesce to form a continuous film. Diffusion is generally slow and films are rough. SK growth is a combination of FV and VW growth mechanisms. Initially film growth occurs *via* layer-by-layer, which in turn is followed by island growth. The transition between the growth modes is dependent on the chemical and physical properties of the substrate and film.

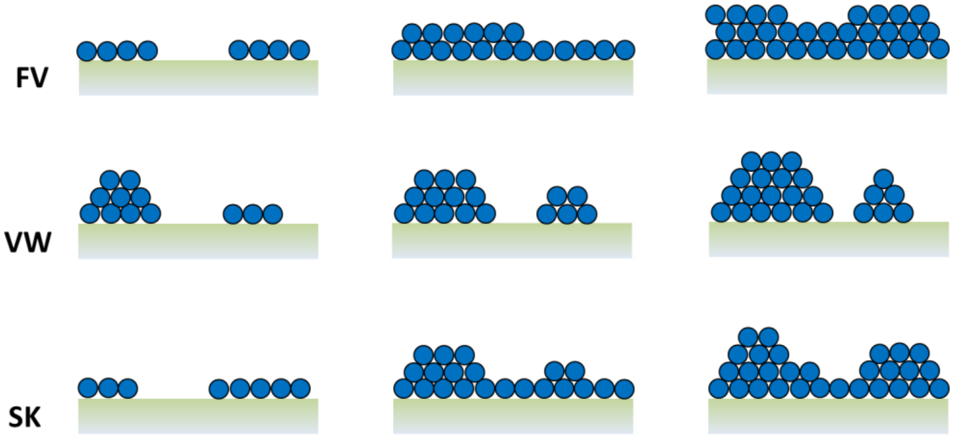

Fig. 1.14. Thin film growth modes: FV, Frank-van der Merwe; VW, Volmer-Weber; SK, Stranski-Krastonov.

The thickness of layers deposited by CVD can vary from single atomic layers (as in ALD) to greater than 100 μm depending on the application of the film.[86] Layer thickness is dependent on the CVD technique and the deposition conditions used. Generally, thick films are a consequence of high growth rates resulting from high temperatures and pressures. Thin films are obtained from low growth rates. The density of the films is also an important parameter for film application. It measures the quality and the potential functionality of the film; the denser the film the better film quality. Film density tends to increase with growth temperature or by annealing the film at high temperatures. Low-density films suffer from high levels of impurities in the crystal lattice and porosity possibly due to the incomplete decomposition of the precursor, a common trait observed in films deposited at low temperatures. The refractive index can give an indication of how dense a film is, denser films tend have a higher refractive index.[86] To have any commercial use, CVD layers must adhere well to the substrate but what influences the extent of adherence is not well understood. It is thought that having a clean and impurity free surface helps adherence as this can influence the growth mode and the amount of nucleation sites for the depositing material. The presence of impurities can lead to a discontinuous loosely bound layer.

Adherence can also be negatively affected by the process of decomposition and cluster formation occurring in the homogeneous gas phase resulting in the snow down of particles onto the growing film. This can lead to loosely adhered films and defects. This phenomenon can happen if the solvent evaporates too quickly leaving behind solid particles of the precursor in the aerosol. Cluster formation can also take place due to the thermophoretic force imposed on particles in the gas-phase. The larger clusters are thus repelled from the hotter surface, as they cannot diffuse through the thermal boundary layer, and are attracted to the cooler top surface. In general, films which are powdered or have low adherence are not desired but such films can sometimes be made adherent by annealing which also tends to form more crystalline films.[92]

1.7.3.3 Fluid dynamics

The flow of gas molecules through a tube is influenced by the nature of collisions that occur between the molecules. The two extremes are: molecules move around without colliding or they collide. The nature of gas flow can be characterised using dimensionless parameters. One such parameter is the *Knudsen's number*, *Kn*, a ratio of the mean free path of intermolecular collisions, λ, and the tube diameter, *L*, of channel in which the gas is flowing, according to equation 1.6.

$$Kn = \frac{\lambda}{L} \qquad \textbf{(Eq. 1.6)}$$

The *Knudsen's number* depends on the nature of the gas. Three scenarios are commonly considered when interpreting the *Knudsen's number*:

- *$Kn < 0.01$: viscous (or continuum) flow* – the gas flow is determined by gas-gas collisions. The molecules undergo many collisions among themselves before they travel any distance in the tube. The gas transports energy, momentum and heat by random diffusion. The flow of gas is smooth and orderly due to the molecules dragging each along by intermolecular frictional forces and maximum velocity is achieved in the centre of the tube with zero velocity at the walls. Low flow rates result in laminar flow (desired; low Reynolds number) whereas high flow rates result in turbulent flow (avoided). The viscous nature of the flow requires a greater vacuum or higher pressures to move the molecules.

- *$Kn > 1$: molecular flow* – the gas molecules rarely collide with each other so the gas flow can be considered collision-less flow. However, whilst the molecules may not collide with each other they do collide with the wall of the tube. The gas molecules can flow in any direction including returning back to the inlet although the overall flow is a result of the restrictions imposed by the walls. Hence, this system can operate at low pressures.

- *$0.01 > Kn > 1$: transition flow* – the molecules do not reflect off from the wall but instead momentarily reside at the wall before randomly entering the gas flow.

At room temperature, the transition from viscous to molecular flow occurs roughly at a pressure of 10^{-3} torr (mean free path ≅ 5 cm). Many CVD reactors are operated with $Kn > 1$ and hence do so without a carrier gas whilst other systems that use a carrier gas or high vapour pressure precursors have a $Kn < 0.01$.[3] For $Kn < 0.01$ (viscous flow), the gas velocity and temperature, and reactant concentration vary with position in a hot-wall tubular flow reactor (Fig. 1.15).[3]

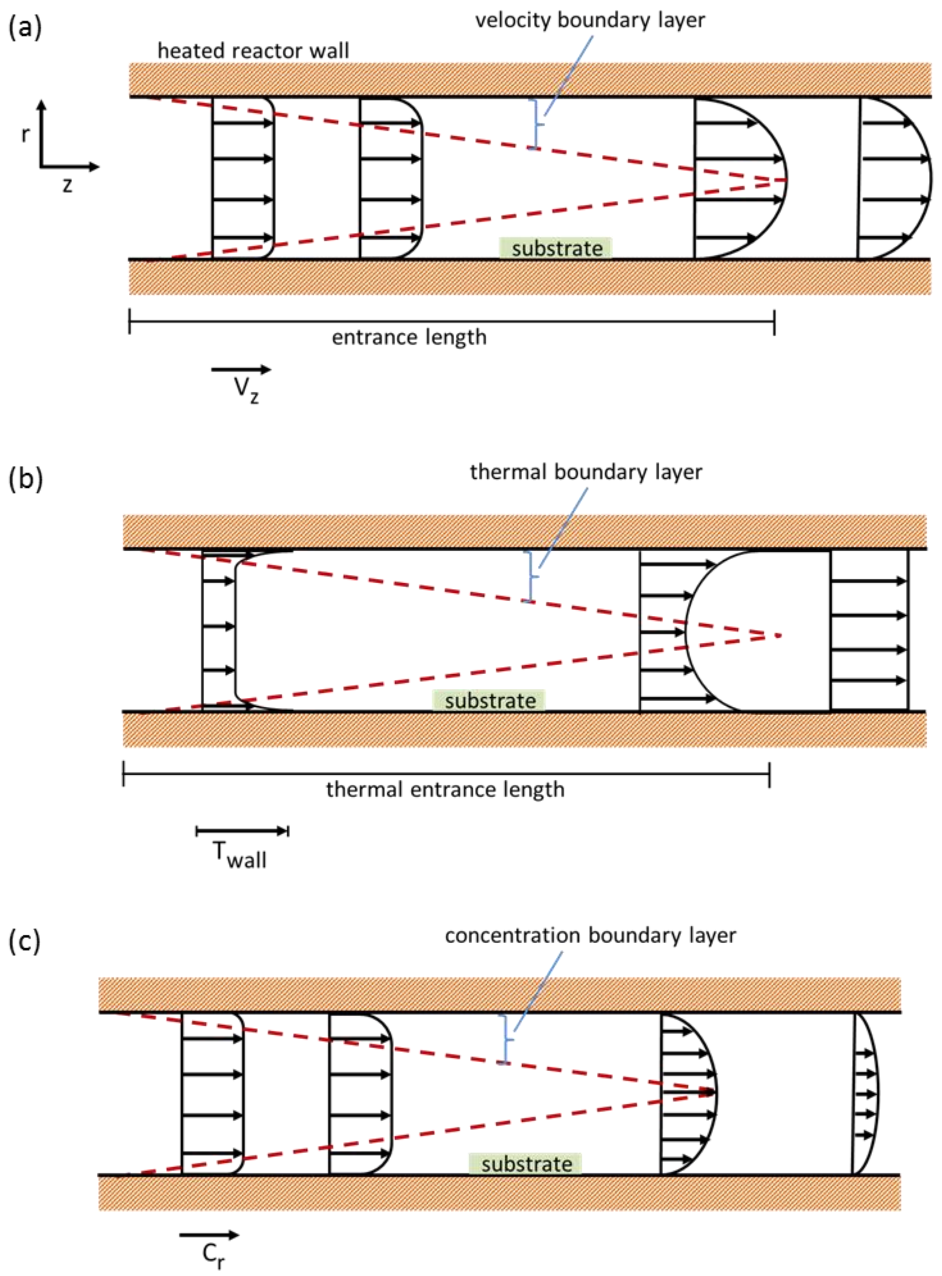

Fig. 1.15. Boundary layer profiles along a hot-walled tubular reactor. (a) Velocity profile (length of arrows represents V_z); (b) Temperature profile (arrows indicate magnitude of temperature at a given location); (c) Reactant concentration profile (lengths of arrows indicate reactant concentration). r, radial direction; z, direction of flow.[3]

The velocity profile (Fig. 1.15a) can change with the direction of flow (z) in the reactor. Due to the viscosity of the gas, gas closest to the reactor walls as it enters sticks to the surface (non-slip conditions). Gas close to the centre of the reactor moves at a velocity governed by the decrease in pressure through the reactor. A velocity gradient (or velocity boundary layer) forms where the velocity at the walls changes from zero to the velocity of the free stream (velocity varies in radial direction, r). The distance from the reactor entrance to this constant velocity is referred to as the 'entrance length' which varies depending on the gas viscosity, gas flow rate and the reactor diameter. After the entrance length, the profile becomes parabolic and the velocity no longer changes along the reactor.[3]

When the gas enters the hot-walled reactor a thermal boundary layer can also be formed (Fig. 1.15b). As soon as the gas enters the reactor, the gas close to the walls heat up but not enough time has passed for the gas further away from the wall to heat up. Moving down the reactor, more and more of the gas becomes heated due to the heat transferred from the hot surfaces and the thermal conductivity of the gas. This results in the formation of a thermal boundary layer – variation in the temperature of the gas at the wall and middle of the reactor. The distance from the reactor entrance to when the gas reaches a constant temperature is called the 'thermal entrance length' which depends on the gas flow rate, gas thermal conductivity and the reactor diameter.[3]

A reactant concentration profile (Fig. 1.15c) shows the depletion of reactants over time. Reactants at the reactor walls are converted into products first. The reaction concentration is close to zero at the reactor wall if the chemical reaction is fast and transport of reactants from centre to the wall is slow. As the gas flows further down the reactor, more and more of the reactant is turned into product at the heated surface. The concentration boundary layer thickness increases with distance along the reactor. However, a concentration boundary layer does not exists under all conditions, even if it is the viscous flow regime. For example, if reactants move rapidly in the radial direction to the surface but the rate of reaction at the walls is slow then no boundary layer exists. The distance it takes for all the reactants to be used up in a rapid reaction (diffusion-limited surface reaction) depends on gas flow rate, reactant/carrier gas diffusion coefficient and the reactor diameter. For sufficient long reactors, all reactant is consumed.[3]

The above is described for hot-walled reactors but the same concepts also apply to cold-walled reactors with other geometries (e.g., horizontal or vertical). The only changes are the shapes in the profiles (Fig. 1.16).

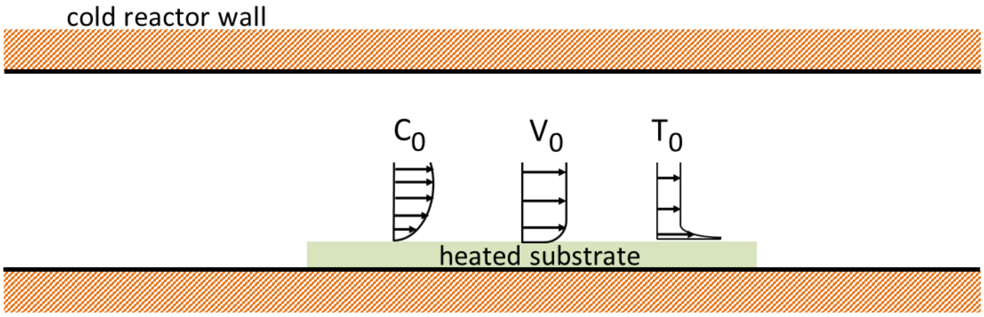

Fig. 1.16. The reactant concentration, velocity and temperature profiles for a cold walled reactor with a heated substrate. The inlet gas has reactant concentration (Co), velocity (Vo) and temperature (To).[3]

A second dimensionless parameter is the *Reynold's number*, *Re*, which can be given as:

$$Re = \frac{U\rho L}{\eta} \quad \textbf{(Eq. 1.7)}$$

where U is the gas stream velocity, ρ is the density of the gas, L is the diameter of the tube and η is the viscosity of the gas. Therefore, the *Reynold's number* is a measure of the relative quantity of gas flowing in a pipe. $U\rho$ gives the bulk velocity, U_∞, so

$$Re = \frac{U_\infty L}{\eta} \quad \textbf{(Eq. 1.8)}$$

The bulk velocity, U_∞, is estimated from the mass flow rate of the carrier gas since the flow rate of the carrier gas is several magnitudes higher than that of the precursor. Typically, the Reynold's number is low (Re < 100) in CVD indicating laminar flow as a consequence of low precursor flow rates. The transition to turbulent flow only occurs when the Reynold's number exceeds 2100. Turbulent flow is not ideal for film growth *via* CVD as the precursor can become trapped within the flow resulting in localised high concentrations which can decompose and form clusters in the homogeneous gas phase.

The characterisation of fluid flow can be investigated using other dimensionless parameters such as Prandtl, Schmidt, Grashof, Peclet and Damkohler.[12]

1.7.3.4 Reaction kinetics

Film growth rates *via* CVD are highly influenced by the substrate temperature, pressure of the reactor and the composition and chemistry of the gas phase.[12, 86] CVD is a non-equilibrium process hence the gas phase precursors react irreversibly on the surface. The kinetics is controlled by the mass transport of these precursors to the substrate. In general, the CVD process involves four key steps: (1) introduction of precursor; (2) precursor transported to the substrate surface; (3) surface reaction and (4) desorption. The slowest step determines the rate-limiting step of the overall process.[12]

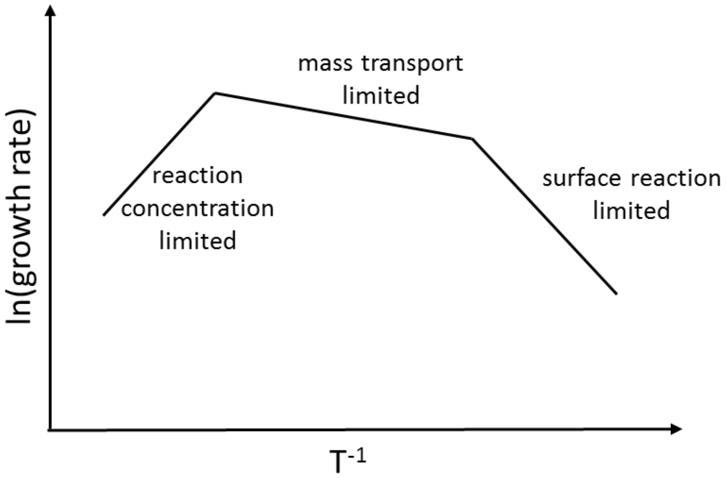

Fig. 1.17. Growth rate of CVD films as a function of temperature.

Three apparent growth modes are shown in Fig. 1.17 as a function of temperature. At low growth temperatures, the film growth rate is determined by the chemical kinetics in the gas phase or at the substrate surface. This region is referred to as *surface reaction limited* (or *kinetic growth control*) and growth rates increase in an exponential, which can be described by the Arrhenius equation:

$$Growth\ Rate = Ae^{-\frac{E_A}{RT}} \qquad \textbf{(Eq. 1.9)}$$

where A is a constant, E_A is the activation energy, R is the gas constant and T is the deposition temperature. As the growth rate is determined from chemical kinetics, so as long as the temperature remains constant over the whole substrate, uniform film thickness can be achieved.[86] As the temperature increases, growth rate depends weakly on temperature but is now controlled by the mass transport of precursors. The region is referred to as *mass transport limited* (or *diffusion controlled growth*). This is the favoured mode for systems that suffer from uniform substrate heating e.g. cold-walled reactors. As temperature is further increased, the growth rate decreases as a result of increased desorption rate and depletion of reactants on the reactor walls (*reaction concentration limited*). Gas-phase reactions become more dominant with increasing temperature, which can lead to unfavourable particle formation rather than desired film formation, hence depleting reactant concentration in the gas phase and can also in turn reduce the rate of reaction.[3, 86] When precursors are delivered in an aerosol (i.e. aerosol assisted CVD) at high temperatures, the system suffers from thermophoresis resulting in a reduced growth rate. The deposition rate for AACVD is limited by the rate of vaporisation of the precursor from the aerosol particles.[3]

The pressure of the CVD reactor determines the importance of each mode. A decrease in pressure results in a decrease in gas-phase reactions; with pressures less than 1 torr resulting in film growth controlled by surface reactions. At very low pressures (e.g., $<10^{-4}$ torr) mass transport growth is completely absent and film growth is controlled by the temperature of the gas and substrate and by the desorption of precursor fragments from the growth surface.[86]

There is also a possible dependence of the reactant concentration when gas-phase particle formation occurs on deposition rates. Generally, deposition rate increases with reactant concentration. However, once critical conditions (e.g., reactant concentration or temperature) are reached gas-phase reactions can take place, resulting in particle formation and reactant depletion, which in turn reduces the deposition rate.[3]

1.7.3.5 Aerosol assisted chemical vapour deposition

Aerosol assisted chemical vapour deposition (AACVD) deviates from conventional CVD in the manner by which the precursor is transported to the deposition substrate (Fig. 1.18). AACVD generates the aerosol by atomising the solution of the chemical precursors, using a well of a nebulizer, into liquid droplets (the aerosol) instead of relying, as in conventional CVD, on evaporation when the carrier gas passes through the liquid in a heated bubbler. The aerosol is then transported into the deposition chamber by the carrier gas. The main advantage of this method is that the precursors do not have to be volatile but only that they must be soluble in any solvent used to generate the aerosol.[14] In fact existing precursors used in CVD can be utilised to great effect including the production of multicomponent materials from single source precursors.[12, 82] Other advantages include the use of thermally unstable precursors widening the choice of precursors, the simplification of the delivery and vaporisation of the precursor and the operation of the reaction system at low or atmospheric pressures (hence no need for a sophisticated reactor or vacuum system).[12, 14] The outcome is a low-cost method for the production of thin films.

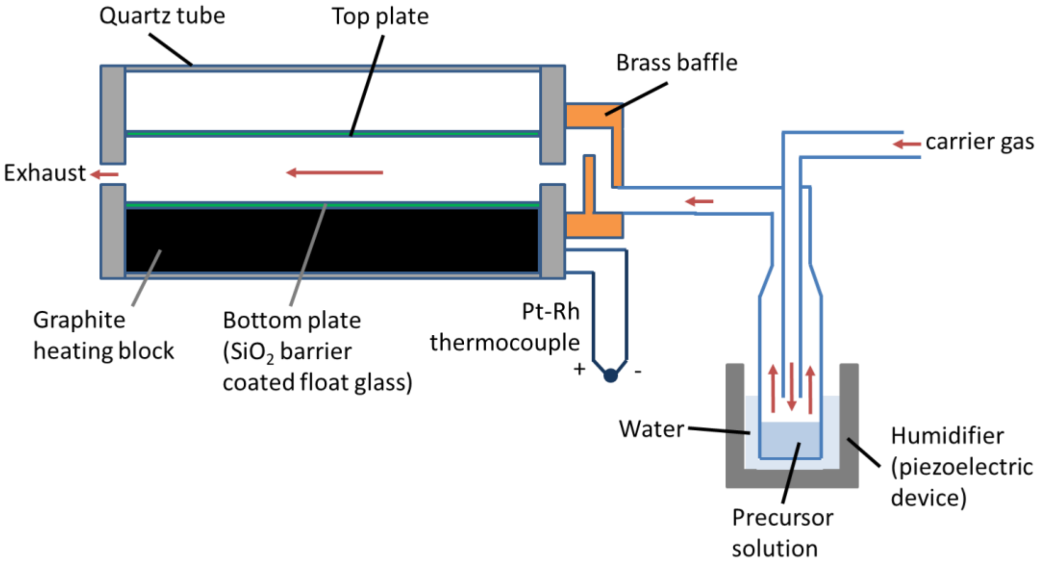

Fig. 1.18. Schematic of an AACVD rig. The precursor solution consists of either an organic solvent or water. The aerosol is generated at room temperature using ultrasound in the humidifier. The carrier gas forces the aerosol droplets into the mixing chamber. Deposition is achieved by heating the horizontal bed to the desired temperature and then allowing the precursor mixture to enter until all of it is used up. This can be typically 20 to 90 minutes depending on the initial amount of solvent used and the required film thickness. The film is cooled under a lower flow rate of the carrier gas.

AACVD has also been referred to as spray pyrolysis but as already described the two methods differ significantly in the transport and reaction of the precursor. In spray pyrolysis the precursor decomposes from the liquid phase on the substrate whereas in AACVD the reactions take place in the gas phase.[4]

Aerosols can be produced using pneumatic spray nozzles (nebuliser) or humidifier units.[93] Pneumatic spray nozzles involve spraying liquid into the reactor with high velocity gas. The liquid atomises and the aerosol droplets move towards the heated substrate. However, in AACVD, a piezoelectric ultrasonic humidifier operated at a specific frequency to generate aerosols is favoured when nanostructured films are desired. This is because the aerosol produced have a narrow size distribution which leads to better aerosol uniformity and in turn coating quality.[93] The mechanism of atomisation is not clearly understood. Proposed hypotheses have been based on capillary waves or cavitation, or a combination of the two.[94] Atomization or droplet formation achieved by capillary waves involves the inducement of standing waves created by the vibrating surface on which the liquid in the bubbler sits at ultrasonic frequencies. These standing waves are called capillary waves which continue to gain energy from the sound waves. Eventually, as their amplitude grows, droplets start to form at the apex which break away forming the aerosol. In the cavitation hypothesis, a gas bubble forms driven by ultrasonic frequencies. These gas bubbles grow during the compression and rarefaction phases of the ultrasonic waves and accumulate energy. Under certain conditions the bubble will implode resulting in hydraulic shocks which lead to the formation of free droplets.

As mentioned above, the droplet size, distribution and production rate can be influenced by the method used to generate the aerosol which in turn can affect the nature and composition of the film.[12] The droplet diameter, *d*, of the aerosol can be determined by Lang's equation:

$$d = 0.34\left(\frac{8\pi\sigma}{\rho F^2}\right)^{\frac{1}{3}} \qquad \textbf{(Eq. 1.10)}$$

where σ is the surface tension coefficient of the liquid, ρ is the density of the liquid and F is the sound frequency of the humidifier.[95] Simulations, using water, have found that the variation in droplet size generally follows that of a normal distribution.[93, 96] It must be stressed that the droplet size estimated from equation 1.10 only applies to the aerosol generated in the bubbler. The droplets can change size during their transportation to the reactor due to the increase in temperature experienced by the aerosol.[4]

The mechanism for film deposition *via* AACVD has not been modelled mathematically. Three possible qualitative scenarios have been proposed which may not necessarily be mutually exclusive which complicates our understanding further (Fig. 1.19).

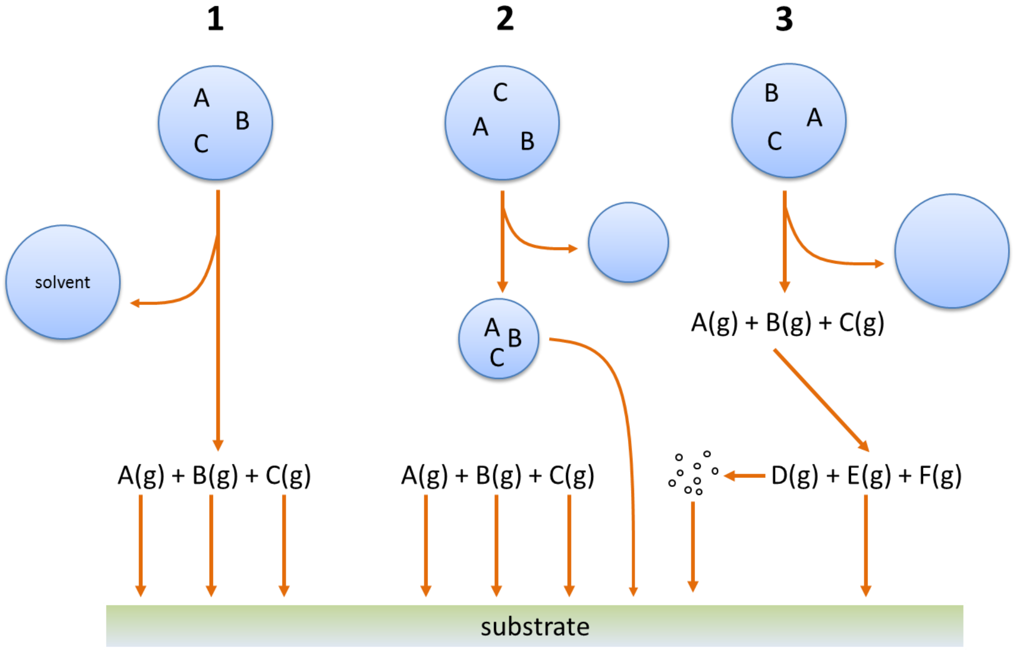

Fig. 1.19. Possible scenarios for the mechanism of aerosol reaction in a AACVD reactor. (1) complete evaporation; (2) incomplete evaporation; (3) complete evaporation and particle formation. Three precursors, A, B and C, are used to illustrate the versatility of AACVD in delivering multiple precursors simultaneously *via* single- or multi-source precursors and/or single or dual bubbler systems (to allow different solvents to be employed).[4]

In the first and simplest scenario (Fig. 1.19(1)) the solvent completely evaporates and the precursor molecules adsorb and decompose on the substrate. This type of decomposition is termed ‘heterogeneous’.[97] In the second scenario (Fig. 1.19(2)), incomplete evaporation take place leading to gas-phase and liquid-phase reactions on the substrate surface. When using an organic solvent, the liquid-phase reactions could account for the presence of carbon contamination that is occasionally observed in the deposited film. The final scenario (Fig. 1.19(3)) involves the complete evaporation of the solvent and the gas-phase reaction of A, B and C to form products D, E and F which can then react or deposit onto the substrate, or react further in the gas phase to form particles that eventually snow down onto the film. The decomposition taking place in the gas-phase only is termed ‘homogeneous’. The nature of the decomposition process, heterogeneous or homogenous, is considered to have a bearing on the morphology of the films, for example, a rough and granular film surface is attributed to homogeneous deposition.[97] Additional complications arise when the precursors have different vapour pressures, different rates of reaction in the gas phase or at the substrate surface.

1.8 Aims

Transparent conducting oxides (TCOs) are an essential component in modern technology. They exhibit both optical transparency and electrical conductivity and as such they are used as transparent electrodes. One of the major challenges in the area is the need to find alternatives to the expensive tin doped indium oxide (ITO) – the champion TCO. Doped ZnO and SnO_2 are suitable candidates but the focus in literature has been to single dope these metal oxides with either a cation or anion such as Al, Ga and Sb or F and Cl, respectively to enhance conductivity. Here, the aim is to use a co-doping method using both cationic and anionic dopants together in an effort to increase the carrier concentration and obtain competitive conductivities for both ZnO and SnO_2 based thin films. Co-doping has not been widely investigated in literature due to processing limitations during synthesis.

The films will be deposited *via* a novel route using aerosol assisted chemical vapour deposition (AACVD), a simple, low-cost and reliable technique for depositing high quality thin films. Two of the attractive features of AACVD are its versatility in allowing the use of precursors that are not suitable to be used in other CVD methods and the facility to use multiple precursors simultaneously within one system.

All films will be tested for their optoelectronic properties using UV/Vis/Near IR spectroscopy and Hall effect measurements. The novel co-doped films produced in this study will be tested against singly cation and/or anion doped counterparts to show that significant enhancements can be made. It is important to note, the use of the TCOs produced from this work as electrodes in devices is beyond the scope of this study. This thesis sets out the preliminary development of co-doped thin films *via* AACVD.

2

Experimental and characterisation methods

This chapter describes the deposition technique used to deposit the thin films as well as giving some background information on the analytical methods used for film characterisation. For a solid to be thoroughly characterised the following information needs to be collected:[86]

- Crystal structure: *unit cell, cell dimensions and coordinates of the atoms present;*
- Crystal defects: *their presence, nature, number and distribution;*
- Crystallinity: *the number, size, shape and distribution of the particles;*
- Surface structure: *includes inhomogeneities, absorbed surface layers or structural differences between surface and interior.*

However, no single technique can give all this information hence a combination of techniques are used. There are three main optical techniques to characterise solids: diffraction, microscopic and spectroscopic. As well as these, thermal analysis and physical property measurements can also be employed to further characterise the films. The techniques used to analyse the thin films are described below.

2.1 Aerosol assisted CVD set-up

The schematic diagram of an AACVD rig set-up is shown in Fig.1.18. This was a cold-walled reactor consisting of an open-ended quartz tube caped at both ends with stainless steel plates. The steel plates support the upper plate which was placed about 5 mm above the glass bottom plate. The glass substrate was heated in the rig on top of a graphite heating block containing a Whatman® cartridge heater. The substrate temperature was controlled and monitored using a Pt-Rh thermocouple.

The inlet steel plate was attached to a brass baffle which directed the flow of the aerosol in the carrier gas into the chamber and together with the top plate ensured a laminar gas flow. Any unreacted chemicals and reaction by-products leave *via* the exhaust in the outlet end steel plate. The glass substrate consisted of SiO_2 barrier coated float-glass (Pilkington Ltd).[98] The coating prevents the ions from within the glass to diffuse to the surface. This ensures that the deposited film is not contaminated with metals such as sodium and calcium. The glass substrate was first cleaned with detergent and water, followed by propan-2-ol, propanone, and then air dried. The aerosol of the precursor solution was generated by bubbling nitrogen gas or air (99.9%; supplied by BOC) through the solution held in a bubbler (Drechsel bottle). The aerosol was generated using a Vicks® ultrasonic humidifier.

The deposition process was started by heating the bottom substrate to the desired temperature under a low flow rate of nitrogen gas or air, monitored and controlled using a flow rate meter. The aerosol was then diverted through into the reactor at a fixed flow rate and the time allowed for the deposition varied according to the solvent used. Once the precursor solution was completely used up, only the carrier gas, at a reduced flow rate, was passed into the chamber. The gas was turned off when the bottom plate had cooled to ~70 °C and then the coated substrate was removed for analysis.

When more than one precursor solution was used a two-pot system was employed which involved aerosols mixing in a Y-junction before entering the deposition chamber (Fig. 2.1).

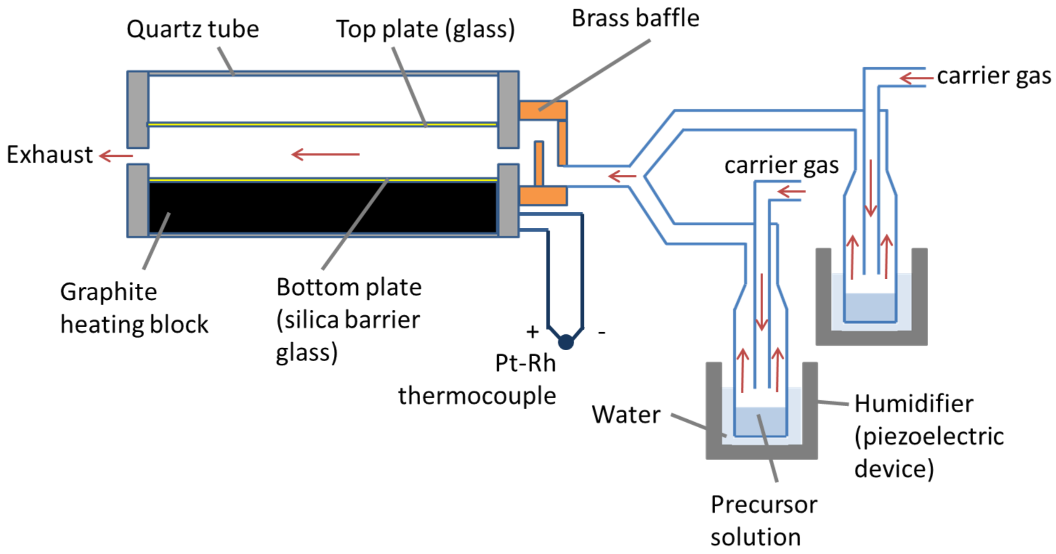

Fig. 2.1. Schematic of a dual-source AACVD rig.

2.2 Film analysis

2.2.1 X-ray diffraction (XRD)

XRD is mainly used for the fingerprint characterisation of crystalline materials and structure determination. Unlike spectroscopic methods, which absorb radiation of certain wavelengths, diffraction employs radiation with a single wavelength i.e., monochromatic radiation.[99] X-rays are produced when a beam of electrons are accelerated towards a metal target causing an inner electron from the metal to be ejected and an outer electron drops to fill the vacancy that is created. The X-rays interact with matter that are scattered in different directions and the radiation is collected by a detector to produce a characteristic X-ray pattern. The brighter the radiations the more intense the peaks on the pattern which is a result of constructive interference (Fig 2.2). This was explained by W. L. Bragg in 1912 when he found that some X-rays diffract from the atoms at the surface whereas others penetrate through the crystal. The penetrating X-ray travels to the next layer of atoms, diffracts and travels back the same distance before reaching the surface again; hence this X-ray travels further than that diffracted off the surface. The difference in distance, d, depends on the spacing between the two planes and the angle, θ, of incidence. For the two rays to combine they must be in-phase (constructive interference) with each other i.e., their path difference ($2d\sin\theta$) must be a whole number of wavelengths ($n\lambda$).[99]

This is Bragg's Law:

$$n\lambda = 2d\sin\theta \quad \textbf{(Eq. 2.1)}$$

Bragg's equation correctly predict that a diffracted X-ray will be observed only at certain angles of incidence. Penetrating rays that do not obey Bragg's Law will be partly or completely out of phase (destructive interference) and hence will show faint/broad peaks or be absent completely from the X-ray diffraction pattern, respectively. The broadness of a peak is usually taken as the peak width. The peak width is described as the full width half maximum (FWHM) of the peak. The unit cell parameters are calculated from the position of a diffracted peak and the intensity of a diffracted peak informs about the atomic positions.

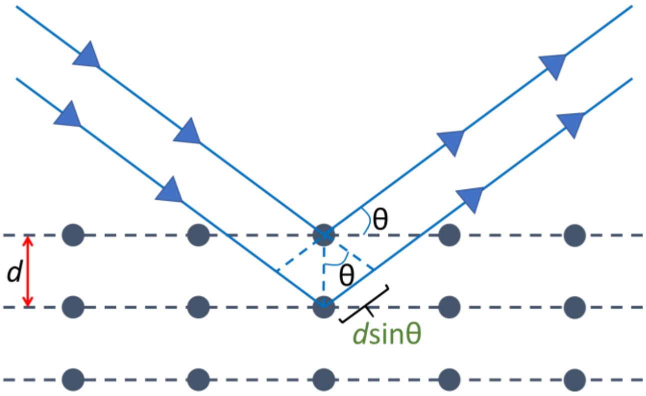

Fig. 2.2. The generation of constructive interference following the interaction of a crystallite with incoming X-rays.

The measurement of reflection intensities was pioneered by Rietveld and reported in 1969.[100] The Rietveld method uses a least squares approach to refine user-selected parameters to minimise the difference between high quality observed data and a calculated pattern, based on a theoretical crystal structure. The Le bail refinement method extends the Rietveld method of obtaining reflection intensities from powder diffraction data to situations without an initial structural model.[101] In the Le Bail method an iterative approach, using the intensity values obtained from the previous least squares cycle, is used to observe the reflection intensities which are at first set arbitrarily to equal values. The unit cell and approximate space group must be predetermined as they are included as part of the fitting technique. The Le Bail was fitted to the powder diffraction data using the general structure analysis system (GSAS) and experiment graphical user interface (EXPGUI) suite.

The lattice parameters are used to determine the crystal structure and hence the type of Bravais lattice (Table 2.1).

Table 2.1. The crystal structure and the associated Bravais lattices. *Monoclinic I – most stable at room temperature; Monoclinic II – only stable at sub-zero temperatures (rarely encountered).

Crystal structure	Symmetry	Lattice constants	Lattice angles	Bravais lattices
Triclinic	C_i	$a \neq b \neq c$	$\alpha \neq \beta \neq \gamma \neq 90°$	Primitive
Monoclinic*	C_{2h}	$a \neq b \neq c$	$\alpha = \gamma = 90°$ $\beta \neq 90°$	Primitive Base-centred
Orthorhombic	D_{2h}	$a \neq b \neq c$	$\alpha = \beta = \gamma = 90°$	Primitive Base-centred Body-centred Face-centred
Tetragonal	D_{4h}	$a = b \neq c$	$\alpha = \beta = \gamma = 90°$	Primitive Body-centred
Hexagonal (rhombohedral)	D_{3d}	$a = b = c$	$\alpha = \beta = \gamma \neq 90°$	Rhombohedrally-centred
Hexagonal (hexagonal)	D_{6h}	$a = b \neq c$	$\alpha = \beta = 90°$ $\gamma = 120°$	Primitive
Cubic	O_h	$a = b = c$	$\alpha = \beta = \gamma = 90°$	Primitive Body-centred Face-centred

The mean crystallite size in a crystal in the form of a powder can be calculated using the Scherrer equation (Eq. 2.2). The formula relates the size of crystallites in a solid to the broadening of a peak in a diffraction pattern, according to the following equation:

$$D = \frac{k\lambda}{\beta cos\theta} \qquad \textbf{(Eq. 2.2)}$$

where D is the crystallite size; λ is the wavelength of radiation used; k is a constant that varies with the shape of the crystallite but usually taken as 0.9; β is the peak broadening at half the maximum intensity (FWHM), in radians; and θ is the Bragg angle in radians. The equation is limited to nano-sized particles.

Depending on deposition parameters, especially with thin films, it is common to find preferred orientation of the crystallites. Hence, at certain angles there are fewer reflections being observed at the detector. The peak intensities observed are compared to a bulk standard to calculate the degree of preference towards a particular plane. Barrett and Massalski[102] derived a formula to calculate preferred orientation and called it the texture coefficient equation:

$$Tc_{(hkl)} = \left[\frac{I_{(hkl)}}{I_{0(hkl)}}\right] \cdot \left[\frac{1}{n}\sum_{1}^{n}\frac{I_{(hkl)}}{I_{0(hkl)}}\right]^{-1} \quad \textbf{(Eq. 2.3)}$$

where Tc is the texture coefficient for the *hkl* plane, $I_{(hkl)}$ is the measured intensity, $I_{0(hkl)}$ is the intensity of the bulk standard and *n* is the number of reflections observed. If the $Tc_{(hkl)}$ value is greater than one, it shows that the crystallites in this (*hkl*) plane are preferentially orientated.

Thin film measurements were obtained using a modified Bruker-Axs D8 diffractometer with parallel beam optics equipped with a PSD LynxEye silicon strip detector to collect diffracted X-ray photons. X-rays were generated using a Cu source with Cu $K_{\alpha 1}$ and Cu $K_{\alpha 2}$ radiation of wavelengths 1.54056 and 1.54439 Å, respectively, emitted with an intensity ratio of 2:1, a voltage of 40 kV, and current of 30 mA. The incident beam angle was kept at 1°, and the angular range of the patterns collected was $10° < 2\theta < 66°$ with a step size of 0.05° counted at 4 s/step unless stated otherwise. The patterns were analysed for crystallinity, mean crystallite sizes and preferred orientation. Peak positions were compared to patterns from the inorganic crystal structure database (ICSD). The lattice parameters were calculated from powder X-ray diffraction data using the software GSAS and EXPGUI *via* the Le Bail refinement.

2.2.2 Film adherence

Film adherence was confirmed using the Scotch™ tape test.[103] A strip of the scotch tape was applied onto the film and removed. The film was considered adherent if the film did not break up upon removal of the tape.

2.2.3 Scanning electron microscopy (SEM)

SEM uses a high-energy electron beam to trace over a material to obtain an image based on electron density. An electron gun produces electrons by heating a filament or by the application of a strong electric field to it. The electrons are accelerated towards the sample by an anode, passing through magnetic lenses to ensure a narrow beam of electrons hits the sample. The electron beam traces over the material resulting in the formation of secondary and backscattered electrons (reflected electrons) (Fig. 2.3). The secondary electrons are detected and are responsible for the images presented in this thesis. Secondary electrons are generated due to the scattering interaction between the incoming electron beam and the valence electrons of the material. Additional sensors detect backscattered electrons and X-rays (emitted from underneath the samples surface). Backscattered electrons are electrons that have scattered off the samples surface and their intensity increases with atomic number due to regions of higher electron density which in turn result in brighter images.

SEM was performed to determine the film morphology (top-down) and film thickness (side-on). Both the JEOL JSM-6700F and JEOL JSM-6301F Field Emission instruments were used for top down and side on configuration, respectively, unless stated otherwise, with accelerating voltages ranging from 3-10 keV. The images were recorded using a software called SEMAfore. This program was also used to calculate the range in particle sizes and the thickness of the films given in Chapters 3-6. The samples (1 × 1 cm) were mounted to the holder with carbon tape and sputter coated with a layer of gold for 1-2 minutes at 25 mA followed by contacts being made using silver paint or copper tape. The gold layer and contacts reduces charging (the gathering of electrons at the surface) from occurring and allows images to be taken more easily and clearly as it increases the signal to noise ratio due to the increased number of secondary electrons detected at the surface.

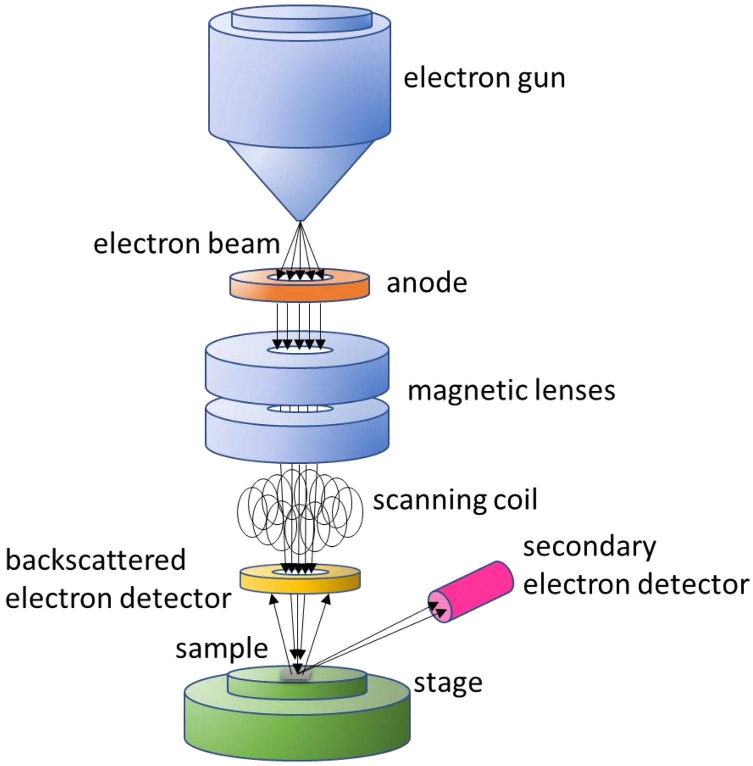

Fig. 2.3. Schematic of the scanning electron microscope (SEM).[5]

2.2.4 Energy dispersive X-ray spectroscopy (EDX)

EDX is used for elemental analysis of the bulk. EDX involves using an electron beam to bombard a sample ejecting a low energy electron from the core shell leaving behind an electron hole. This hole is filled with an electron from a higher energy shell and the difference in energy between the shells is released in the form of an X-ray. The energy and number of X-rays (characteristic to an element) are measured by the spectrometer, hence elemental composition of a sample can be known. EDX calculations were carried out using the JEOL JSM-6301F field emission instrument with an acceleration voltage of 20 kV and a programme called INCA. Unlike SEM, samples were coated with a thin layer of carbon to avoid charging as carbon does not inhibit the detection of light elements. Analytical accuracy for EDX measurements for major elements is ±2% (relative).

2.2.5 Wavelength dispersive X-ray spectroscopy (WDX)

WDX is also a method used for elemental analysis of the bulk especially for the detection and quantification of lighter elements (between boron and oxygen) as this technique is more sensitive. Unlike EDX, WDX only counts X-rays of a single wavelength at one time and does not produce a broad spectrum of wavelengths simultaneously. WDX analysis was carried out on a Phillips ESEM. Analytical accuracy for WDX measurements for major elements is ±1% (relative).

2.2.6 X-ray photoelectron spectroscopy (XPS)

XPS gives elemental composition and the oxidation states at a surface of the material. XPS irradiates the sample with X-rays in a vacuum causing core electrons to be ejected (Fig. 2.4). The kinetic energy of the ejected electrons depends on the binding energy of the atomic orbital from which they originated from (hence element specific) and the incident X-ray. The intensity and position of the peak gives information about the concentration and identity of the species present. Only electrons less than 10 nm deep are likely to reach the detector hence XPS is a surface sensitive technique.

Analysis of the films were carried out using a Thermo Scientific κ-Alpha spectrometer fitted with a monochromatic Al-K_α (0.834 nm, 1486.6 eV) source. X-rays were focused on a 400 μm spot on the sample surface. Sample charging was avoided by using a dual beam flood gun. Survey scans were collected in the range 0–1100 eV (binding energy) at a pass energy of 200 eV. Higher resolution scans were recorded for the main core lines at a pass energy of 20 eV. For depth profiling, an argon ion gun was used. The peaks were modelled using CasaXPS software with binding energies adjusted to adventitious carbon (284.5 eV) in order to compensate for the effects of charging.

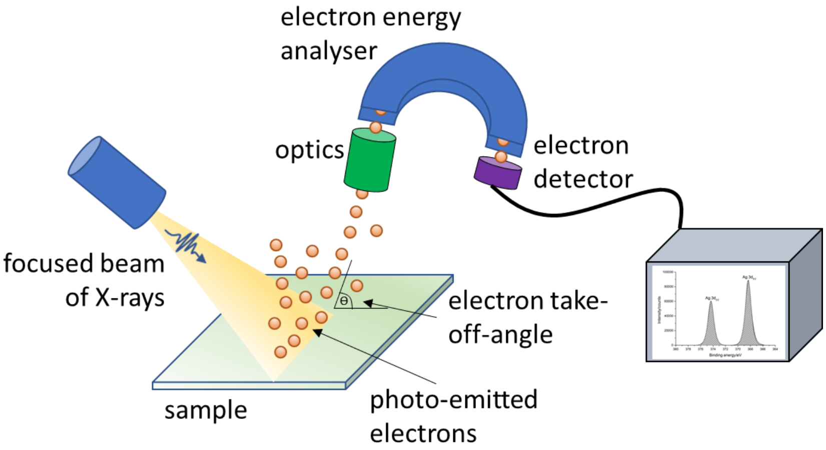

Fig. 2.4. Schematic of a photoelectron spectrometer.

2.2.7 UV-visible-near infrared spectroscopy

Optical properties are measured using a UV-vis/IR spectrometer. A beam of light is separated into its component wavelengths by diffraction grating or a prism. The grating is rotated so that only a specific wavelength of light can reach the aperture. The light interacts with the sample and reaches a detector which in turn results in a spectra we collect (Fig 2.5). The programme used to record the data was called UV WinLab. The absorption and reflectance in the visible range affects the perceived colour of a material. UV/Vis/Near IR transmittance and reflectance spectra were measured using the Perkin Elmer Lambda 950 UV-vis/IR spectrometer with an air background. Spectra were recorded between 320-2500 nm. The band gap was calculated from transmittance and reflectance data using the Tauc plot method.[13] A graph of $(\alpha h\nu)^n$ against $h\nu$ is plotted where α is the absorption coefficient and $n = 2$ or 0.5 depending on whether it is a direct or indirect band gap, respectively. The graph is then extrapolated linearly from the steepest part of the Tauc plot towards the x-axis to obtain a value for the band gap.

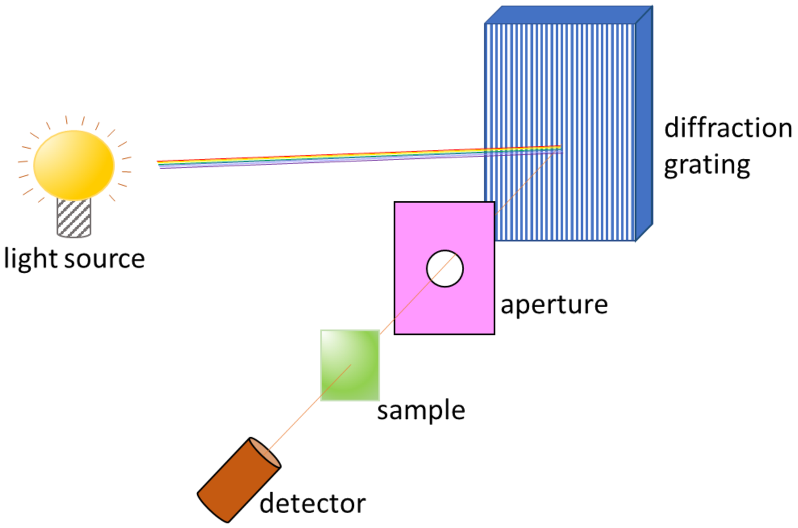

Fig. 2.5. Schematic of a UV-Visible-Near Infrared spectrometer.

2.2.8 Optical measurements of film thickness

Film thicknesses were measured using the Filmetrics F20 machine operating in reflectance mode in air against an as supplied FTO standard (Chapter 3). The machine measures the amount of light reflected from the sample over a range of wavelengths (350-1000 nm) and this data is computed *via* the fast Fourier transform (FFT) technique by calibrating it with a series of calculated reflectance spectra for a silica standard substrate. The output is a graph of oscillations which is fitted, using a goodness of fit approach, to a theoretical model.

2.2.9 Electrical testing

Hall effect measurements were carried out on an Ecopia HMS-3000 set up in the Van der Pauw configuration to determine the resistance (ρ), free carrier concentration (*n*) and mobility (μ). Samples of 1 cm^2 were prepared and silver paint (Agar Scientific) was used to form ohmic contacts which were tested on the in-built software prior to measurement. The samples were then subjected to an input current of 1 mA and a calibrated magnetic field of 0.58 T (Fig. 2.6). The magnetic field is present perpendicular to the flow of current and when a sample is subjected to this, a potential difference is observed. This is the Hall voltage and together with film thickness allows the calculation of the wanted electrical parameters.

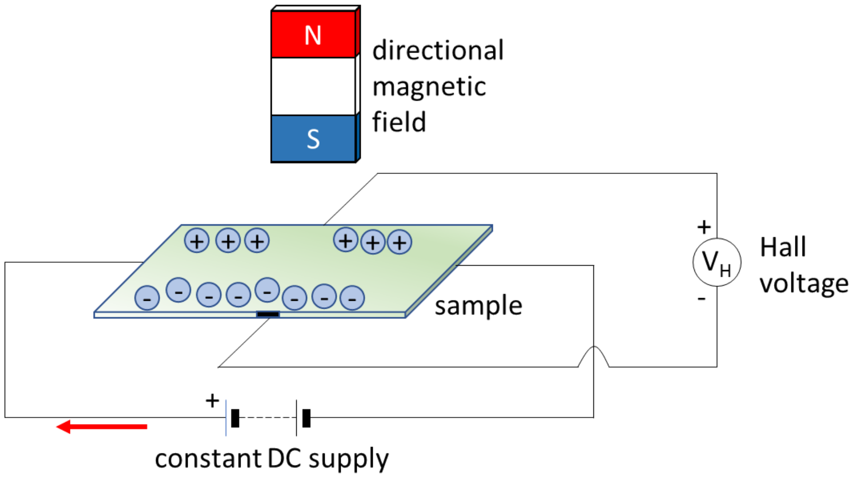

Fig. 2.6. Schematic of the Hall effect instrument used for electrical testing.

3

Aluminium or/and fluorine doped zinc oxide thin films

This chapter focuses on the production of conductive and transparent aluminium and/or fluorine doped zinc oxide thin films deposited *via* a dual source route. The films were colourless and adherent, with no noticeable degradation over a prolonged storage time. Doping films with a cation has attracted a lot of attention however anion doping has not been as common, with reports of co-doping being even scarcer.

3.1 Introduction

The most widely used commercial TCO films have been made using indium or tin based oxides.[15] Tin doped indium oxide (ITO) is the most commonly produced TCO followed by fluorine doped tin oxide (FTO).[75] However, indium is in limited supply and relatively expensive, and the price of tin has risen rapidly in the past few years.[104] Thus, there is a need to find alternative materials that can be employed in optoelectronic devices. Zinc oxide films have been recognised as suitable alternatives based on the low cost, greater earth abundance and comparable optoelectronic properties.[63, 105, 106]

Doping increases the carrier concentration in order to achieve greater conductivity. It can also widen or narrow the band gap particularly at high doping concentrations.[7, 107] The band gap is widened or blue shifted (frequency of phonons interacting with the incident photon increases) because of the lower states in the conduction band being blocked. However, band gap narrowing is attributed to the shallow level donor impurities creating energy levels in the band gap near the conduction band edge and shallow acceptor impurities create energy levels near the valence band edge, effectively narrowing the gap by merging of the donor level and the conduction band.[35, 63] Nevertheless, over doping is not desirable as it has a detrimental effect on conductivity as a result of deterioration in the film structure leading to a reduction in the mobility of the free electrons.[23, 108] Zinc oxide with a wurtzite structure is a wide band gap semiconductor (3.37 eV).[105] The incorporation of dopants into the ZnO lattice is known to alter its properties.[109] Intrinsic ZnO can satisfy the optical properties of a TCO however the carrier concentration is about 10^6 cm^{-3} at room temperature hence, too low for a TCO for practical applications.[63]

Incorporating group III elements into the ZnO lattice as shallow donors, have also shown promise in the production of TCOs.[110, 111, 112, 113, 114, 115] Aluminium doped ZnO films involve Al^{3+} (0.54 Å) occupying a Zn^{2+} (0.74 Å) site leading to a reduction in the lattice parameters. Hu and Gordon deposited AZO films *via* APCVD and found improved conductivities compared with undoped ZnO, with aluminium dopant amounts between 0.3-1.2 at.%.[116] In contrast, Olvera *et al.*[113] deposited AZO films *via* a chemical spray technique producing a film with 3 at.% Al at 450 °C and found that the electrical conductivity value was lower than their undoped ZnO. This could be attributed to their deposition method and/or significantly greater Al dopant amounts leading to over-doping. However, film transparency remained high, at about 85%, for the film.

The degeneracy of crystallinity and variations in lattice constants in zinc oxide due to the difference in ionic radii between the dopants and Zn^{2+} or O^{2-} can be partially resolved by co-doping.[63] Fluorine acts as a shallow donor and is incorporated into the lattice by substituting an O^{2-} site with F^- (O^{2-}: 1.24 Å; F^-: 1.17 Å) resulting in one more free electron making fluorine a suitable dopant for n-type conductivity.[115, 117] Doping with fluorine is known to improve electrical properties since the conduction band is not too disrupted as it is the valence band that is made up of the oxide ion.[63, 118] Choi and Park[119] deposited FZO thin films *via* ALD incorporating up to 1.2 at.% fluorine. They found the lowest resistivity was when the film contained 1 at.% F with a transmittance of 83%. Over-doping with fluorine may lead to the ion not occupying the correct site in the lattice thereby being rendered inactive and in turn leading to a reduction in conductivity and mobility by providing more scattering centres.[118]

Co-doping with aluminium and fluorine has the potential to minimise the lattice distortion and lead to TCO ZnO materials with enhanced figures of merit.[63]

3.2 Experimental details

The depositions in this chapter were carried out using a two-pot system in a fume-hood. An undoped zinc oxide film was made from glass bubbler one containing 0.25 g diethylzinc (15 wt.% in toluene) in ~25 mL dry toluene and the second holding ~40 mL dry methanol (an oxygen source) (Scheme 1). When Al-doped ZnO thin films were deposited the required mol% of trimethyl aluminium (2.0 M in toluene) was added to the diethylzinc and toluene mixture (Scheme 2). In contrast, when ammonium fluoride (98%) was used to deposit F-doped ZnO thin films, this precursor was added to the dry methanol bubbler (Scheme 3). For the co-doped film the dopants were added to the respective glass bubblers at the same time (Scheme 4). The precursors were all purchased from Sigma Aldrich. The solvents were purchased from Fischer Scientific. Toluene was stored under alumina columns and dried with Anhydrous Engineering equipment whereas the methanol was dried by distillation over magnesium turnings. All depositions were carried out under Nitrogen gas (≥99.9%) supplied by BOC at a flow rate of 1.0 L min^{-1} and a temperature of 450 °C. The mists produced using humidifiers were transported to and mixed in a Y-joint before entering the reactor. The depositions usually lasted between 50-90 minutes. The films were adherent with an overall substrate coverage of approximately 25% and were transparent and colourless with no evidence to the naked eye (brown tints) of carbon contamination.

$$\mathrm{ZnEt_2 + MeOH \xrightarrow[450\ ^{\circ}C;\ N_2]{dry\ toluene} ZnO} \qquad \text{(Scheme 1)}$$

$$\mathrm{ZnEt_2 + MeOH + AlMe_3 \xrightarrow[450\ ^{\circ}C;\ N_2]{dry\ toluene} AZO} \qquad \text{(Scheme 2)}$$

$$\mathrm{ZnEt_2 + MeOH + NH_4F \xrightarrow[450\ ^{\circ}C;\ N_2]{dry\ toluene} FZO} \qquad \text{(Scheme 3)}$$

$$\mathrm{ZnEt_2 + MeOH + AlMe_3 + NH_4F \xrightarrow[450\ ^{\circ}C;\ N_2]{dry\ toluene} AFZO} \qquad \text{(Scheme 4)}$$

To avoid using air sensitive precursors, preliminary experiments tested the viability of using zinc acetate, zinc 2-ethylhexanoate, aluminium nitrate and aluminium acetylacetonate as precursors. However, the conductivities of the resultant films were too low.

The films discussed in the following chapter will be referred to as the amount of dopant(s) found in the bulk of the film rather than the amount present in the precursor solution.

3.2.1 Instrumental conditions

The XRD patterns shown in this chapter were collected at an incident beam angle of 0.5° (AZO and AFZO) or 1° (undoped ZnO and FZO), with an angular range of $10° < 2\theta < 66°$ with a step size of 0.05° counted at 0.5 s/step (AZO and AFZO) or 1 s/step (undoped ZnO and FZO). Lattice parameters were calculated by fitting a Le Bail model to the XRD patterns using general structure analysis system (GSAS). The cell parameters used for the modelling were a = 3.249860 Å, b = 3.249860 Å and c = 5.206620 Å.

WDX analysis was carried out on a Phillips ESEM. The Zn, Al and F at.% was derived from the Zn-K_α line (8638 eV), Al-K_α (1487 eV) and F-K_α (676.8 eV) X-ray emission lines, respectively.

3.3 Results and discussion

3.3.1 AACVD of AZO films

AZO films were deposited on SiO_2 barrier coated glass using various mol.% amounts (10, 20 and 30 mol.%) of the aluminium dopant, trimethyl aluminium, in the diethyl zinc and toluene mixture.

The reaction of diethylzinc with methanol when the two aerosol flows combine in the Y-joint is expected to yield zinc methoxide[120] and various clusters, including cubanes, similar to those discussed by Jana *et al.* and Sokolowski *et al.*[121, 122] These species then go on to decompose in the CVD reactor to form the ZnO film. The addition of dopant quantities of trimethyl aluminium and/or ammonium fluoride into the AACVD solution(s) results in the incorporation of aluminium and/or fluorine into the cluster compounds such of those seen by Peterson *et al.*[123]

Wavelength dispersive X-ray spectroscopy was used to determine the at.% of aluminium in the bulk of the film. It was found that 10, 20 and 30 mol.% films, which represent the dopant amounts in the precursor solution, contained 0.3 ($Zn_{0.997}Al_{0.003}O$), 0.5 ($Zn_{0.995}Al_{0.005}O$) and 1 ($Zn_{0.99}Al_{0.01}O$) at.%, respectively (Table 3.1). WDX is an ideal technique for detecting dopant amounts present in small quantities due to its sensitive nature as it produces spectra for specific elements (unlike energy dispersive X-ray spectroscopy (EDX) which does a survey scan of all the elements) with better peak resolution. Hu and Gordon also produced AZO thin films with aluminium dopant in low quantities.[116] One possible explanation for the low efficacy of the aluminium dopant in film deposition could be a consequence of the relatively low mass of Al^{3+} ions. In contrast, the deposition efficacy of a dopant solution containing a heavier +3 ion, Ga^{3+}, was substantially greater (Chapters 4), an observation made by others too.[63]

Table 3.1. The relationship between mol.% in solution and at.% of aluminium in the films, deposited at 450 °C, determined by wavelength dispersive X- spectroscopy.

mol.% in solution	at.% determined by WDX
10	0.3
20	0.5
30	1

3.3.1.1 Crystal structure

X-ray diffraction patterns of the AZO thin films with varying dopant amounts are presented in Fig. 3.1. All films were polycrystalline and as expected crystallinity decreases with increasing dopant amounts due to the disruption of the crystal structure. The diffraction patterns all confirm a hexagonal wurtzite structure of zinc oxide. No peaks for any secondary ZnO_x, AlO_x or $AlZnO_x$ phases were observed. However this does not rule out the presence of small amounts of these phases, as they would not be visible in the XRD pattern due to dampening by the more intense ZnO peaks. Furthermore, any X-ray amorphous secondary phases would also not be detected by XRD.

The Scherrer equation was used to calculate the mean crystallite diameter in the films (Table 3.2). No apparent correlation was found between the crystallite size and dopant amount. Lattice parameters calculated by fitting a Le Bail model to the XRD patterns using general structure analysis system (GSAS) showed a contraction in unit cell volume compared with the standard ZnO and undoped ZnO. The observed trend in contraction would be attributed to the substitution of Zn^{2+} (0.74 Å) with Al^{3+} (0.54 Å).[124, 125]

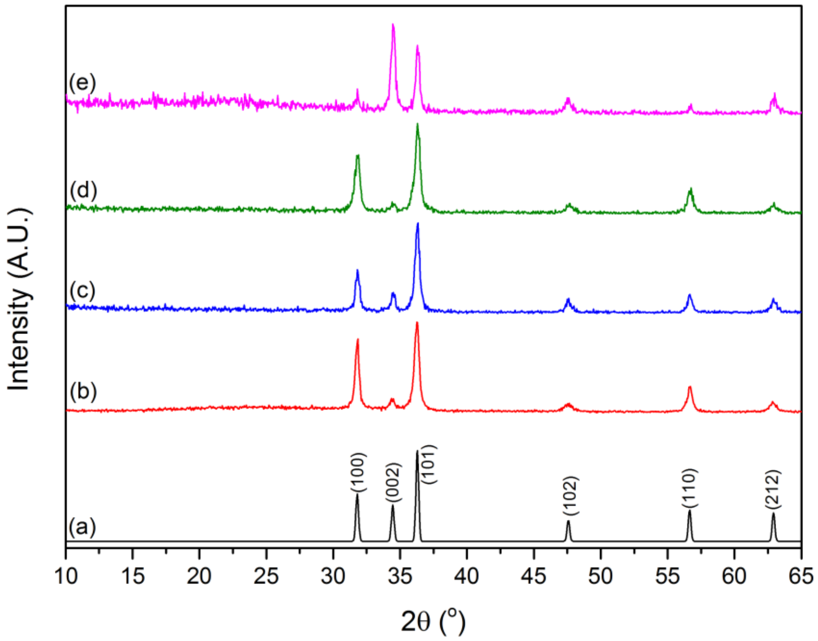

Fig.3.1. XRD patterns of ZnO and AZO thin films deposited *via* dual source AACVD at 450 °C (a) standard ZnO[126] (b) undoped ZnO (c) $Zn_{0.997}Al_{0.003}O$ (d) $Zn_{0.995}Al_{0.005}O$ (e) $Zn_{0.99}Al_{0.01}O$.

Table 3.2. Variation in the mean crystallite diameter and unit cell parameters of ZnO and AZO thin films with varying dopant concentrations of $AlMe_3$.

Film	**Mean crystallite diameter /nm**	**a /Å**	**c /Å**	**Unit cell volume /Å³**	**Volume contraction /%**
ZnO	18	3.2510(2)	5.2145(10)	47.730(9)	
$Zn_{0.997}Al_{0.003}O$	18	3.2475(4)	5.2010(11)	47.558(11)	0.36
$Zn_{0.995}Al_{0.005}O$	17	3.2477(4)	5.2042(16)	47.538(14)	0.40
$Zn_{0.99}Al_{0.01}O$	22	3.2467(7)	5.2054(10)	47.519(17)	0.44

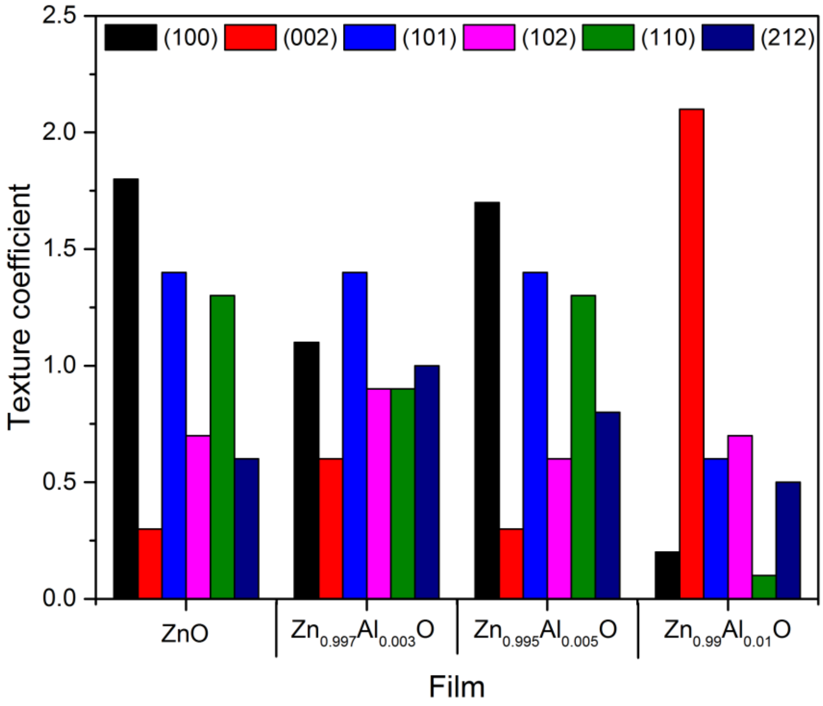

Fig. 3.2. Variation of the texture coefficient (Tc) of each plane with different aluminium dopant amounts.

Preferred orientation was determined using the texture coefficient equation (Equation 2.3) and is shown in Fig. 3.2. The undoped zinc oxide film showed preferred orientation along (100), (101) and (110) planes. The most significant departure of the texture coefficient from the undoped ZnO was found in the film that contained 1 at.% Al, in particular, the prominence of the (002) peak. This has previously been seen in literature when ZnO is doped with cations and/or anions. This is due to the (002) plane having the lowest surface energy in the ZnO crystal therefore growth in the (002) direction is preferred and occurs perpendicular to the substrate.[124, 127,128] Changes in preferred orientation is also influenced by the amorphous substrate.[129]

3.3.1.2 Surface morphology

The surface morphology of the films was studied using a scanning electron microscope (Fig. 3.3). The images show all AZO films having good particle connectivity with no apparent void spaces. The undoped ZnO film (Fig. 3.3a) featured a dense rough morphology with relatively fine irregular particles. Addition of aluminium dramatically alters the surface morphology, most notably is the increase in general particle size and definable shapes compared with the undoped ZnO film. This is common for ZnO based films that are grown by various techniques and is attributed to low surface energy planes that grow perpendicular to the substrate.[14, 130] At the lowest Al dopant amount (Fig. 3.3b) a mixture of irregular shapes, ranging from 150-400 nm, have formed with only a few protruding plates which were roughly 200 nm long. With increasing dopant levels there was a reduction in the variety of irregular shapes (Fig. 3.3 c and d) and at the greatest dopant level of aluminium there was greater consistency in particle shape and size (likened to grass seeds) as well as more protruding plates.

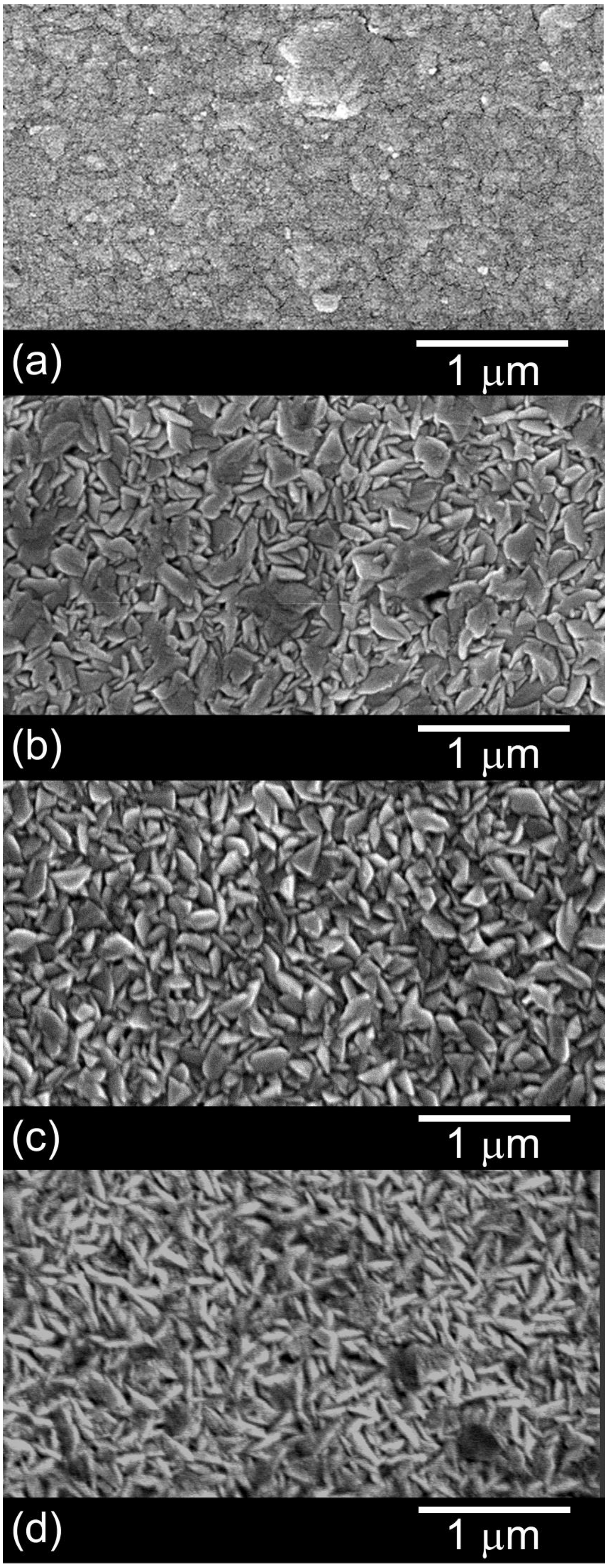

Fig. 3.3. SEM images of ZnO and AZO thin films deposited *via* dual source AACVD at 450 °C. (a) undoped ZnO (b) $Zn_{0.997}Al_{0.003}O$ (c) $Zn_{0.995}Al_{0.005}O$ (d) $Zn_{0.99}Al_{0.01}O$.

3.3.1.3 Optical measurements

Ultraviolet/visible/near infrared spectroscopy was used to investigate the transmittance and reflectance properties of the undoped ZnO and AZO films. The spectra shown in Fig. 3.4 indicate all films have high transparency across the visible. At 550 nm, the aluminium doped films had transparencies >80% whereas the undoped ZnO film was slightly below this. All films displayed poor reflectance in the infrared, reaching a maximum of ~17% at 2500 nm for the film with 1 at.% Al. The number of and depth of the interference fringes is a function of film thickness. Undoped ZnO film presented interference fringes as a consequence of a thickness variation across the area analysed. Interference fringes can also be present because of multiple reflections that occur at the interfaces between the air and the thin film, the thin film and the substrate and the barrier coating and glass of the substrate.

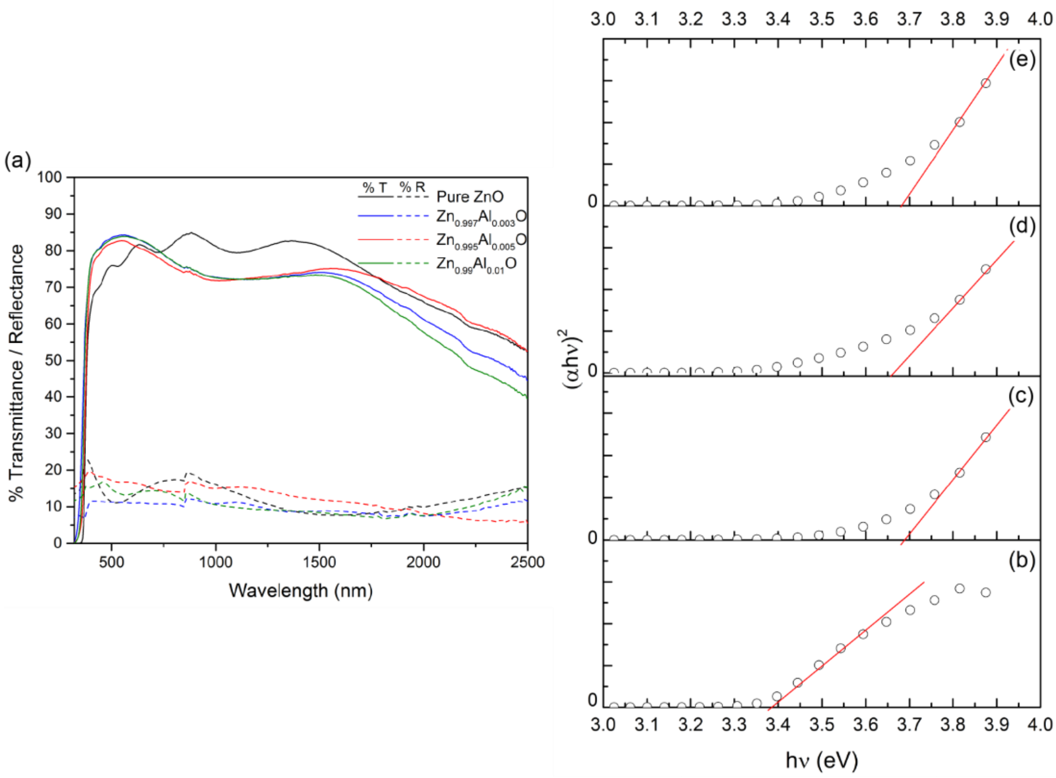

Fig. 3.4. (a) Optical transmittance and reflectance spectra taken with an air background for ZnO and AZO thin films deposited at 450 °C. The Tauc plots to obtain the band gap for (b) undoped ZnO (c) Zn$_{0.997}$Al$_{0.003}$O (d) Zn$_{0.995}$Al$_{0.005}$O (e) Zn$_{0.99}$Al$_{0.01}$O.

The band gap was determined from Tauc plot[13] calculations. The undoped ZnO film had the expected direct band gap of 3.4 eV.[8] The band gap increased when films were doped with aluminium, independent of dopant concentration, to 3.7 eV. This phenomenon was due to the Moss-Burstein effect (Section 1.3). This increase correlates with the greater observed transparency (Fig. 3.4) in the visible.

3.3.1.4 Electrical properties

Hall effect measurements were carried out at room temperature using the van der Pauw technique. The films were identified as n-type from the negative Hall coefficients. Overall, the doped films had better electrical properties compared to the undoped ZnO film (Table 3.3). As expected, the charge carrier concentration, n, increased with increasing dopant amounts due to Al being a donor dopant. Carrier concentration is a determinant of conductivity; when the concentrations are in the order of $\times 10^{18}$ cm^{-3} the conductivity is determined only by the grain boundaries whereas at greater magnitudes the conductivity is also determined by the bulk properties.[131] Grain boundaries trap charge carriers hence reducing the mobility, μ. In general, the greater the charge carrier concentration, the lower the mobility due to collisions between charge carriers. The AZO films had an increase in carrier concentration compared with the undoped ZnO film and as such resulted in a decrease in mobility. The sheet resistance, R_{sh}, calculation takes into account the film thickness, d, and it was found that the AZO films were lower than the undoped ZnO film.

Table 3.3. Hall effect measurements and film thicknesses of ZnO and AZO films. d, film thickness; n, charge carrier concentration; μ, charge carrier mobility; ρ, bulk resistivity; R_{sh}, sheet resistance.

Film	d/nm	n/ × 10^{20} cm^{-3}	μ/cm^2 V^{-1} s^{-1}	ρ/×10^{-3} Ω cm	R_{sh}/Ω □$^{-1}$
ZnO	350	1.163	20.4	2.627	75.1
$Zn_{0.997}Al_{0.003}O$	400	1.896	16.0	2.326	58.2
$Zn_{0.995}Al_{0.005}O$	350	1.989	14.1	1.965	56.1
$Zn_{0.99}Al_{0.01}O$	300	2.387	16.0	1.638	54.6

3.3.2 AACVD of FZO films

Thin films of FZO were deposited on SiO_2 barrier coated glass by adding 5, 10 or 20 mol.% of ammonium fluoride into the dry methanol solution. WDX could not detect the presence of fluorine in the film deposited, even after repetition, using the 5 mol.% ammonium fluoride solution. However, this does not mean the fluorine was absent altogether as it is well known that fluorine, being a light element, is difficult to detect especially at low quantities even when a sensitive technique is used like WDX. Therefore, the analysis of the 5 at.% film will not be discussed alongside the other FZO films. It was found that 10 and 20 mol.% in solution gave 1 ($Zn_{0.99}F_{0.01}O$) and 2 ($Zn_{0.98}F_{0.02}O$) at.% in the film, respectively (Table 3.4). This amount of fluorine in FZO films have also been reported using different deposition methods.[118, 119, 132]

Table 3.4. The relationship between mol.% in solution and at.% of fluorine in the films, deposited at 450 °C, determined by wavelength dispersive X- spectroscopy.

mol.% in solution	at.% determined by WDX
10	1
20	2

Fluorine is difficult to incorporate into the ZnO lattice[119] and therefore most studies found in the literature report FZO films with less than 1 at.% F.[118] Furthermore, the likely reaction of NH_4F taking place inside the deposition chamber is given in equation 3.1.

$$NH_4F \rightarrow NH_3 \uparrow + HF \uparrow \qquad \textbf{(Eq. 3.1)}$$

Therefore, the HF gas produced is highly likely to escape with the waste gases, reducing the availability of fluorine for incorporating into the lattice. Hence, this is why relatively small amounts of fluorine are detected in the film lattice even when high dopant concentrations of the fluorine are added to the precursor solution.

3.3.2.1 Crystal structure

The XRD patterns of the FZO thin films are shown in Fig. 3.5. All films were polycrystalline, confirming a hexagonal wurtzite structure of zinc oxide. There was no appreciable difference in the mean crystallite sizes calculated using the Scherrer equation (Table 3.5). The observed trend in contraction would be attributed to the substitution of O^{2-} (1.24 Å) with F^- (1.17 Å).[115, 117]

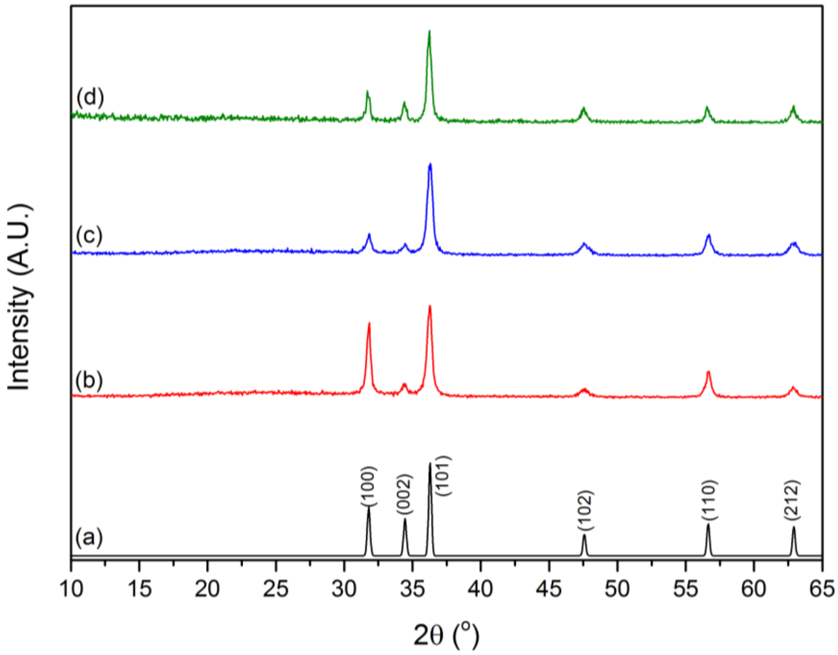

Fig. 3.5. XRD patterns of ZnO and FZO thin films deposited *via* dual source AACVD at 450 °C. (a) standard ZnO[126] (b) undoped ZnO (c) $Zn_{0.99}F_{0.01}O$ (d) $Zn_{0.98}F_{0.02}O$.

Table. 3.5. Variation in the mean crystallite diameter and unit cell parameters of ZnO and FZO thin films with different dopant concentrations of NH_4F.

Film	Mean crystallite diameter /nm	a /Å	c /Å	Unit cell volume / Å^3	Volume contraction /%
ZnO	18	3.2510(2)	5.2145(10)	47.730(9)	
$Zn_{0.99}F_{0.01}O$	16	3.2487(4)	5.2098(11)	47.617(9)	0.24
$Zn_{0.98}F_{0.02}O$	17	3.2491(4)	5.2068(11)	47.603(11)	0.27

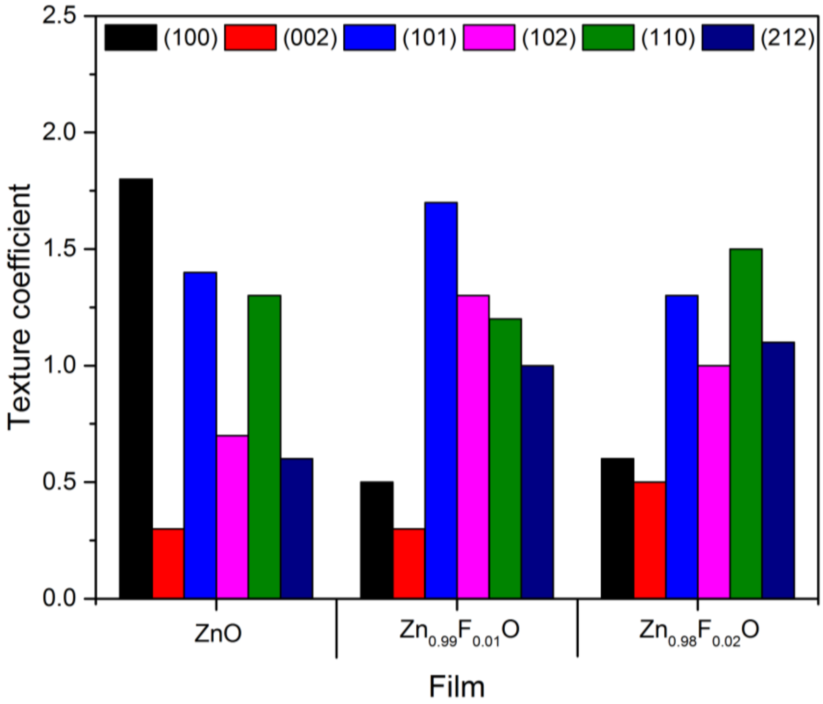

Fig. 3.6. Variation of the texture coefficient (Tc) of each plane with different fluorine dopant amounts.

The results of the texture coefficient calculations are shown in Fig. 3.6. Similar to the AZO study, when ZnO was doped with fluorine there was a reduction in the preference for the (100) plane and an increase in preference for the (002) plane. An increase in preference for the (212) plane was also seen. The consensus in the literature is that the texture coefficient of the (002) plane decreases and the preferred orientation switches to the (100) and/or (101) planes when ZnO is doped with fluorine.[14, 132, 133] The differences between the studies cited and the present study is most likely a consequence of deposition method and the precursors used. Even for an AACVD study on FZO by Bhachu *et al.* found a preference for the (100) plane.[14]

3.3.2.2 Surface morphology

The undoped ZnO film (Fig. 3.7a) featured a dense rough morphology with relatively fine irregular particles. The FZO thin films showed good particle connectivity with no visible glass substrate. The morphology of $Zn_{0.99}F_{0.01}O$ (Fig. 3.7b) and $Zn_{0.98}F_{0.02}O$ (Fig. 3.7c) were different to the undoped ZnO film. The $Zn_{0.99}F_{0.01}O$ film exhibited a uniform distribution of particles of similar size and shape (approx. 170-200 nm) without any protrusions or island growths. The $Zn_{0.98}F_{0.02}O$ thin film showed a more diverse morphology and protruding particles of various sizes up to approximately 320 nm. Again this is typical of doped ZnO films.[14, 130] Also evident are larger structures which appear to sit on top of the film and are therefore assumed to be artefacts as they were not observed consistently or with any distinctive growth morphology.

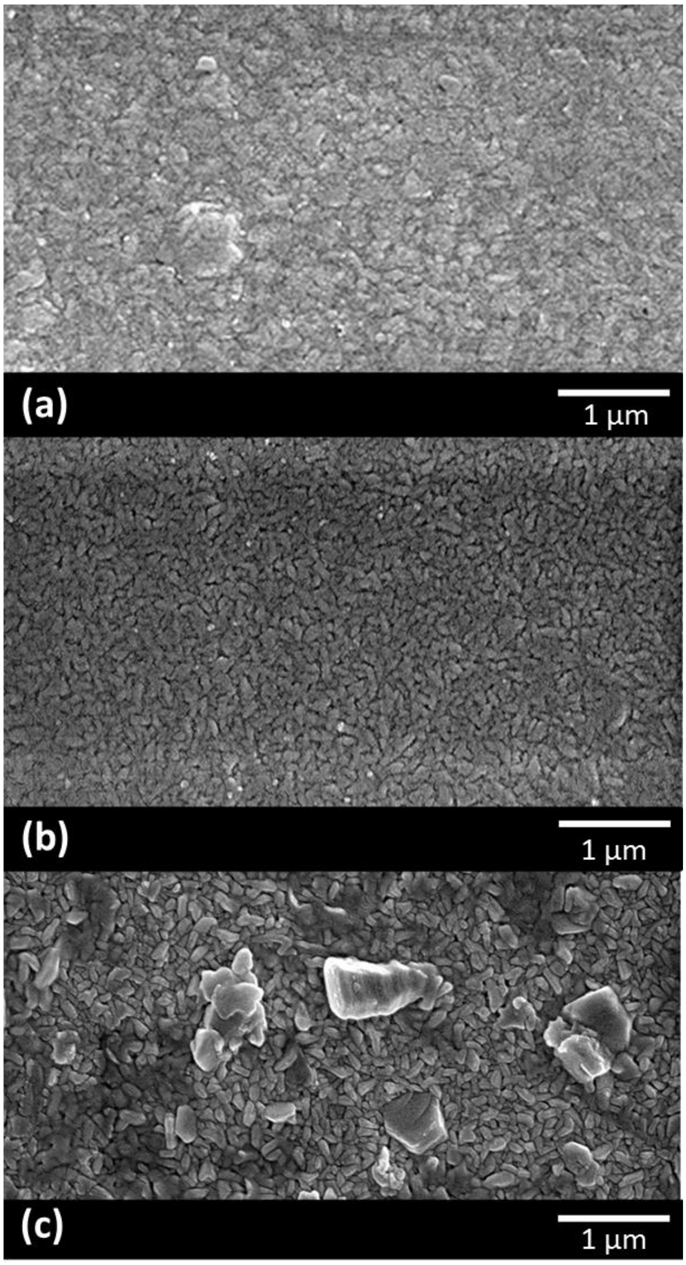

Fig. 3.7. SEM images of ZnO and FZO thin films deposited *via* dual source AACVD at 450 °C. (a) undoped ZnO (b) $Zn_{0.99}F_{0.01}O$ (c) $Zn_{0.98}F_{0.02}O$.

3.3.2.3 Optical properties

The F-doped ZnO films showed a maximum transmittance of 84% in the visible, greater than that seen in undoped ZnO (Fig. 3.8). Reflectance was seen to increase in the infrared region when the films were doped with fluorine. Doping with fluorine caused the onset of the plasma absorption edge to be blue shifted in comparison with the undoped ZnO film. Usually, the shift in the plasma edge is correlated with an increase in charge carrier concentration however, other factors are also known to affect the shift such as the dielectric constant. All the films showed notable interference effects. The band gap for $Zn_{0.99}F_{0.01}O$ and $Zn_{0.98}F_{0.02}O$ increased from 3.4 eV to 3.6 and 3.5 eV, respectively.

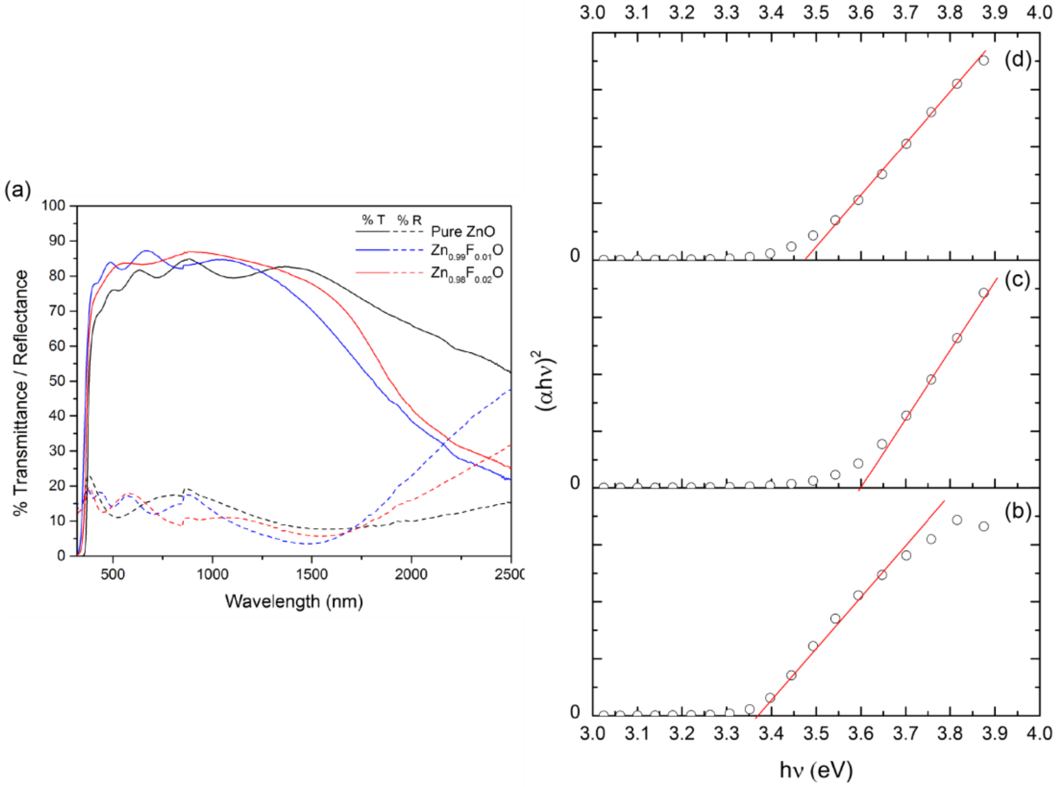

Fig. 3.8. (a) Optical transmittance and reflectance spectra taken with an air background for ZnO and FZO thin films deposited at 450 °C. The Tauc plots to obtain the band gap for (b) undoped ZnO (c) $Zn_{0.99}F_{0.01}O$ (d) $Zn_{0.98}F_{0.02}O$.

3.3.2.4 Electrical properties

The films were identified as n-type from the negative Hall coefficients and had similar film thicknesses. The doped films exhibited better electrical conductivities compared to the undoped ZnO film as expected (Table 3.6). As mentioned above, the higher the charge carrier concentration the lower the mobility and this is what is observed with the FZO films. Both films, $Zn_{0.99}F_{0.01}O$ and $Zn_{0.98}F_{0.02}O$, had similar sheet resistances although one film had double the F amount. Furthermore, the doubled concentration of F detected did not double the carrier concentration, as one would expect therefore suggesting charge compensating mechanisms were taking place after a certain level to limit the carrier concentration. This maybe the primary reason for the levelling off of the sheet resistance after 1 at.% F doping. FZO films displayed lower sheet resistances than the AZO films. In order to investigate the effect of having both a cation and anion dopants present together, co-doped films were deposited.

Table 3.6. Hall effect measurements and film thicknesses of ZnO and FZO films. *d*, film thickness; *n*, charge carrier concentration; *μ*, charge carrier mobility; *ρ*, bulk resistivity; R_{sh}, sheet resistance.

Film	*d*/nm	*n*/ ×10^{20} cm^{-3}	*μ*/cm^2 V^{-1} s^{-1}	*ρ*/×10^{-3} Ω cm	R_{sh}/Ω □$^{-1}$
ZnO	350	1.163	20.4	2.627	75.1
$Zn_{0.99}F_{0.01}O$	350	3.009	17.9	1.157	33.1
$Zn_{0.98}F_{0.02}O$	300	4.057	14.7	1.044	34.8

3.3.3 AACVD of the AFZO film

A co-doped AFZO was deposited on SiO_2 barrier coated glass using 30 mol.% trimethyl aluminium in diethyl zinc and toluene mixture, and 10 mol.% ammonium fluoride in a dry methanol at 450 °C under a flow of N_2. These conditions were used as previously it was shown that when the films were singly doped the aluminium content was found to be the greatest as well as giving the lowest sheet resistance, and the 10 mol.% of ammonium fluoride gave the largest blue shift of the plasma edge, a property ideal for heat mirror applications. Interestingly from WDX, the F at.% in the film remained the same as when it was singly doped but the Al at.% doubled from 1 to 2 at.% using the same mol.% solution giving the film $Zn_{0.97}Al_{0.02}F_{0.01}O$ (Table 3.7). One possibility, although difficult to verify, is that the small aluminium ions were attracted into the lattice by the presence of the small highly electronegative fluoride ions that had already been incorporated into the ZnO lattice.

Table 3.7. The relationship between mol.% in solution and at.% of aluminium and fluorine in the co-doped film, deposited at 450 °C, determined by wavelength dispersive X- spectroscopy.

	mol.% in solution	at.% determined by WDX
Al	30	2
F	10	1

3.3.3.1 Crystal structure

The XRD pattern for co-doped ZnO film, $Zn_{0.97}Al_{0.02}F_{0.01}O$, is shown in Fig. 3.9. The diffraction pattern matched that of the hexagonal wurtzite structure of zinc oxide, as expected, with no secondary phases observed. The mean crystallite size was calculated which reflected the size of the single doped $Zn_{0.99}Al_{0.01}O$ film. The unit cell volume of the co-doped film contracted by 0.78% which would agree with a prediction based on an approximately linear contraction as a function of dopant percentage (Table 3.8). 1 at.% Al contracted by 0.44% and approximately every 0.05 at.% the contraction increases by 0.04% hence the cation contraction would be about 0.52%. 1 at.% F in the ZnO lattice made the unit cell volume contract by 0.24 % hence together a contraction of roughly 0.76% would be expected.

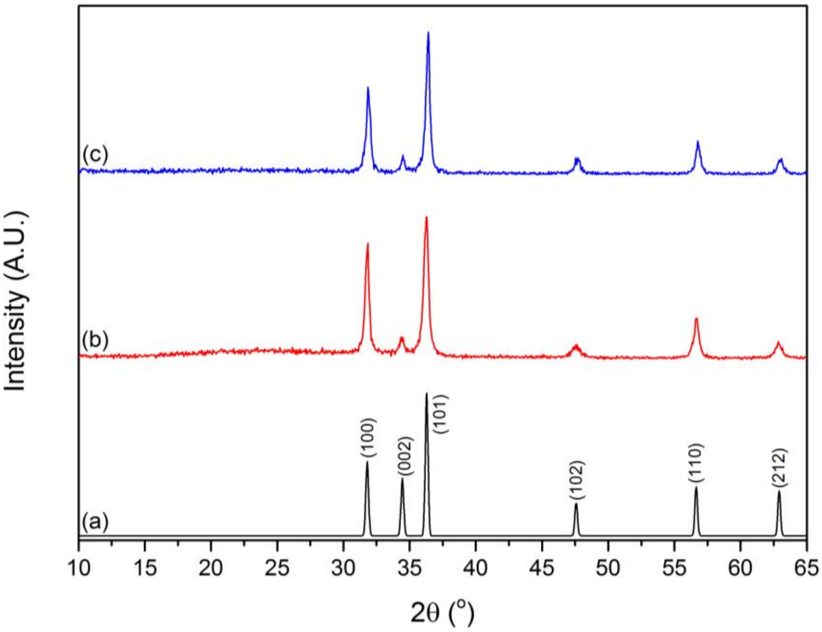

Fig. 3.9. XRD patterns of ZnO and AFZO thin films deposited *via* dual source AACVD at 450 °C. (a) standard ZnO[126] (b) undoped ZnO (c) $Zn_{0.97}Al_{0.02}F_{0.01}O$.

Table 3.8. Variation in the mean crystallite diameter and unit cell parameters of ZnO and AFZO thin films.

Film	Mean crystallite diameter /nm	a /Å	c /Å	Unit cell volume /Å³	Volume contraction /%
ZnO	18	3.2510(2)	5.2145(10)	47.730(9)	
$Zn_{0.97}Al_{0.02}F_{0.01}O$	21	3.2421(3)	5.202(1)	47.360(1)	0.78

There was little change in preferred orientation to the ZnO polycrystalline film upon co-doping with Al and F as shown in Table 3.9.

Table 3.9. Variation of the texture coefficient (Tc) of each plane for ZnO and AFZO thin films.

	Miller planes					
	(100)	(002)	(101)	(102)	(110)	(212)
ZnO	1.8	0.3	1.4	0.7	1.3	0.6
$Zn_{0.97}Al_{0.02}F_{0.01}O$	1.8	0.3	1.4	0.8	1.1	0.6

3.3.3.2 X-ray photoelectron spectroscopy

The oxidation states of the Zn and Al species on the surface of the AFZO was determined through X-ray photoelectron spectroscopy. The Zn $2p_{3/2}$ transition occurred around 1020.9 eV corresponding to Zn^{2+} (Fig. 3.10a). The Al 2p peak has heavy overlap of the $2p_{3/2}$ and $2p_{1/2}$ therefore the double separation is ignored during the fitting process. The Al 2p peak was centred at 73.6 eV, matching literature findings for Al^{3+} (Fig. 3.10b). Depth profile (etched for 1750 seconds) of $Zn_{0.97}Al_{0.02}F_{0.01}O$ film found the Al content to be consistent throughout the film with slightly more Al in the bulk than on the surface as shown in Fig. 3.10c.

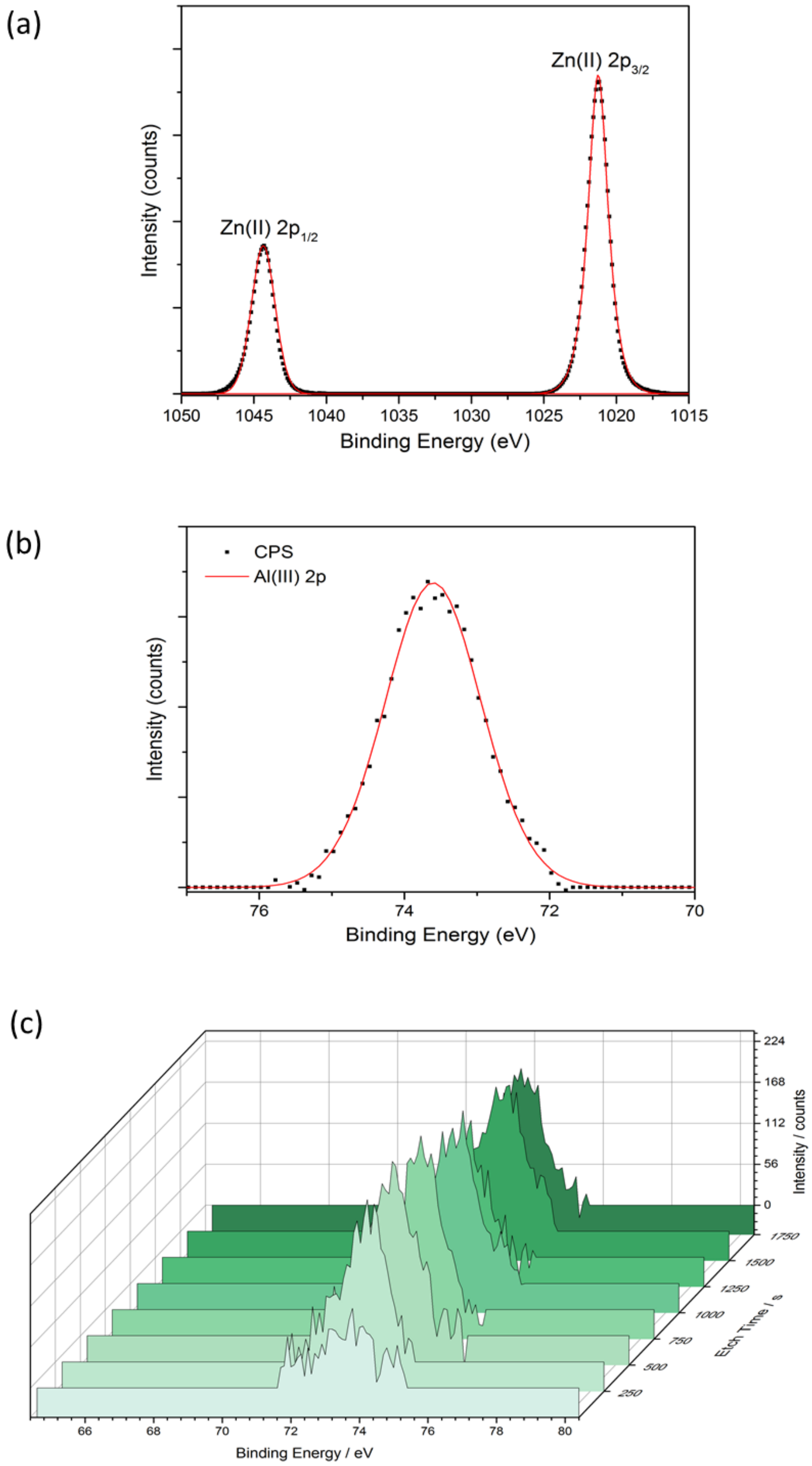

Fig. 3.10. XPS spectra of $Zn_{0.97}Al_{0.02}F_{0.01}O$ showing (a) Zn $2p_{3/2}$ and $2p_{1/2}$ peaks, (b) Al 2p peak and (c) depth profile of the Al content in the film.

3.3.3.3 Surface morphology

The images in Fig. 3.11 show the change in surface morphology from undoped ZnO to the co-doped, $Zn_{0.97}Al_{0.02}F_{0.01}O$, thin film. There is an obvious change in morphology when co-doped as seen by a greater abundance of defined shaped particles (the majority ranging from approx. 140–300 nm) which are similar to the observed morphology of single doped AZO films. This would suggest that the presence of aluminium has a more significant impact on surface morphology, dominating any observable influence of the presence of fluorine.

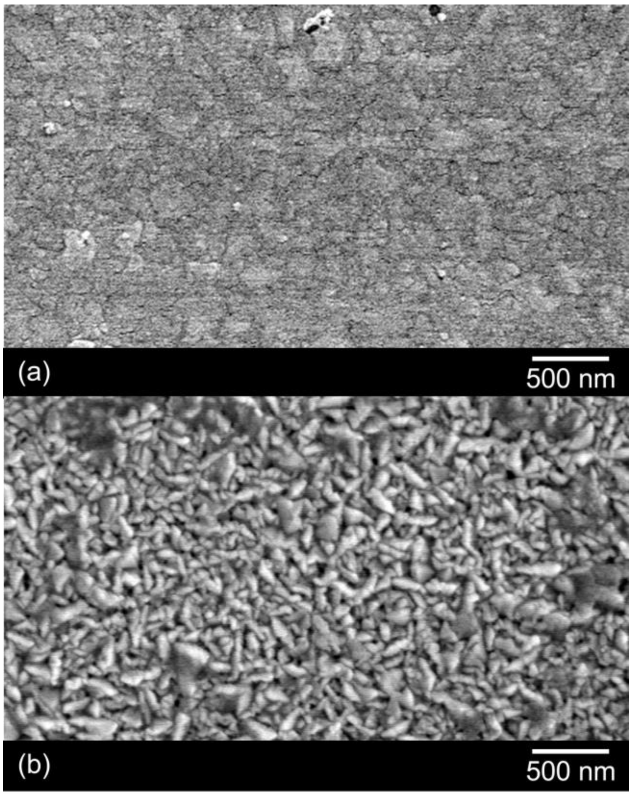

Fig. 3.11. SEM images of ZnO and AFZO thin films deposited *via* dual source AACVD at 450 °C. (a) undoped ZnO (b) $Zn_{0.97}Al_{0.02}F_{0.01}O$.

3.3.3.4 Optical properties

The co-doped film, $Zn_{0.97}Al_{0.02}F_{0.01}O$, maintained the high transparency of 84% at 550 nm seen in the singly doped films and reflectance reached >50% in the infrared (Fig. 3.12). Whilst the onset of the increase in reflectance was at a similar wavelength, the crossover was further blue shifted compared to the FZO films (Section 3.3.2.3) which is mainly a consequence, but not the only reason, of the relatively large concentration of the charge carriers. This shift is suitable for a heat mirror as it enables the transmission of both visible and infrared radiation that would allow solar energy gain for heating purposes in cold climates.[72] The band gap was marginally larger than the single doped AZO and FZO films with a value of 3.7 eV.

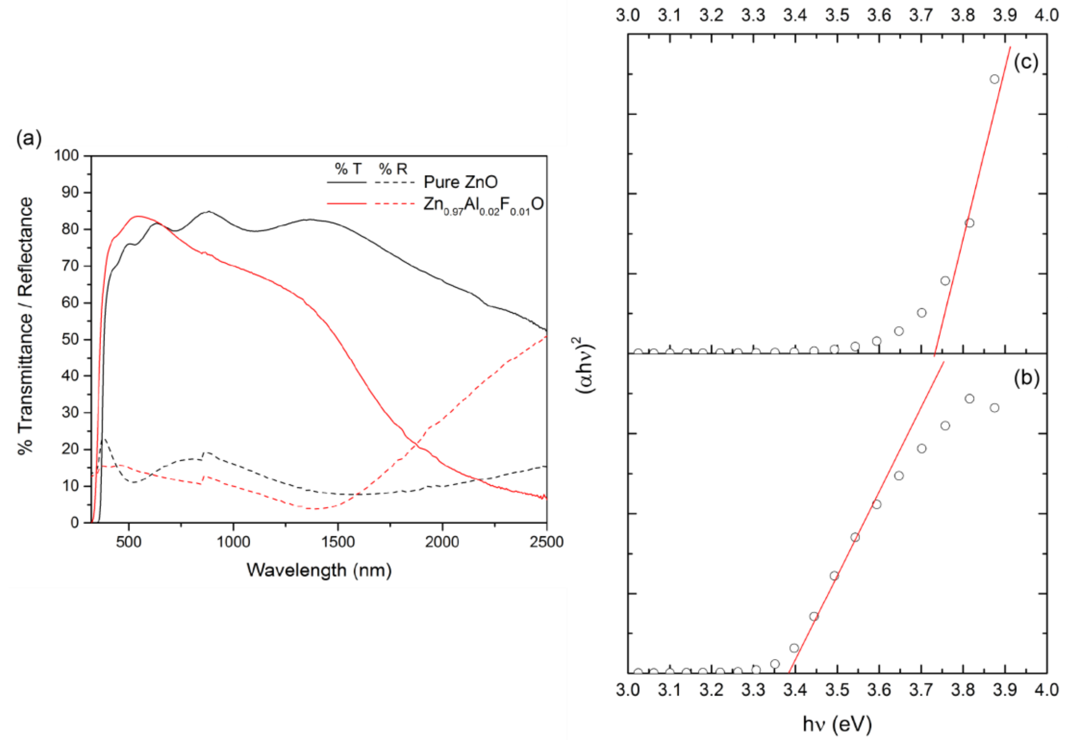

Fig. 3.12. (a) Optical transmittance and reflectance spectra taken with an air background for ZnO and $Zn_{0.97}Al_{0.02}F_{0.01}O$ thin films deposited at 450 °C. The Tauc plots to obtain the band gap for (b) undoped ZnO (c) $Zn_{0.97}Al_{0.02}F_{0.01}O$.

3.3.3.5 Electrical properties

The Hall effect measurement was carried out as before using the van der Pauw technique (Table 3.10). The n-type co-doped film had a lower sheet resistance compared with the undoped ZnO film. As before with the single doped AZO films, the mobility decreased with an increase in the charge carrier concentration. However, despite the presence of two electron-donating dopants, the sheet resistance was not as low as the single doped FZO films.

Table 3.10. Hall effect measurements and film thicknesses of ZnO and AFZO films. *d*, film thickness; *n*, charge carrier concentration; *μ*, charge carrier mobility; *ρ*, bulk resistivity; R_{sh}, sheet resistance.

Film	d/nm	n/ ×10^{20} cm^{-3}	μ/cm^2 V^{-1} s^{-1}	ρ/×10^{-3} Ω cm	R_{sh}/ Ω □$^{-1}$
ZnO	350	1.163	20.4	2.627	75.1
$Zn_{0.97}Al_{0.02}F_{0.01}O$	350	3.297	10.2	1.864	53.3

3.4 Conclusions

Aerosol assisted chemical vapour deposition (AACVD) proved to be a simple and effective method for the deposition of thin films with good coverage and adherence as well as exhibiting commercially attractive optoelectronic properties. AACVD provides a low-cost and flexible approach for the single doping and co-doping of films without a significant alteration to the apparatus.

The singly doped and co-doped ZnO films exhibited high transparency (>80%) and resistivities lower than that of undoped ZnO. The FZO film, $Zn_{0.99}F_{0.01}O$, was found to have the best electrical properties of all the films. However, it was the co-doped film, $Zn_{0.97}Al_{0.02}F_{0.01}O$, that gave the better compromise between electrical and optical properties, shifting the plasma edge (the onset of the increase in reflectance) to lower wavelengths making them more suited for applications such as heat mirrors. There was a dramatic change in the morphology of the film when aluminium was incorporated into the ZnO lattice as a single dopant or co-doped with fluorine. In both cases, resulting in the presence of recognisable shaped structures and scattered morphology making them ideal for photovoltaic devices. X-ray photoelectron spectroscopy confirmed the oxidation state for zinc and aluminium and revealed the dopant aluminium was found not to be surface segregated.

The next chapter deals with the deposition and characterisation of ZnO based films doped with gallium, another group III element. It is not clear cut which dopant, aluminium or gallium, gives the superior optoelectronic properties of the ZnO film as it very much depends on a number of factors including the method and conditions used to deposit the films. Therefore, to allow comparison, AACVD will be used to deposit the films, using the same carrier gas and keeping the same flow rate and deposition temperature as used for the films in the present chapter. The study will be extended to include fluorine as a co-dopant. Again, this is to exploit the reputation that fluorine has as an excellent substituent of oxygen in the lattice resulting in an increase in charge carriers.

4

Gallium doped and gallium-fluorine co-doped zinc oxide thin films

The following chapter analyses films of gallium doped zinc oxide (GZO) and gallium and fluorine doped zinc oxide (GFZO) thin films deposited *via* a dual source aerosol assisted chemical vapour deposition (AACVD) system. The effect of varying dopant concentrations of GZO was analysed and the best film conditions were then used to produce co-doped GFZO films, with the fluorine content varying. All films were investigated focusing on the growth behaviour and optoelectronic properties.

4.1 Introduction

Zinc oxide based films are increasingly finding applications as transparent conducting oxides (TCO) with the potential to replace the most commonly used TCO, tin doped indium oxide (ITO). The success of ITO thin films is down to their high transmittance in the visible spectrum (above 80%), a wide band gap (greater than 3.1 eV) and low electrical resistivity (less than 10^{-3} Ω cm).[15] Adding a dopant to the hexagonal wurtzite ZnO structure, which has a band gap of 3.37 eV and an electrical resistivity of the order 10^{-3} Ω cm, can enhance the optoelectronic properties.[134] Fluorine and the group III elements have successfully been used as dopants.[110, 111, 135, 136, 137, 138]

The slightly smaller ionic radius of the fluoride ion compared with the oxide ion (O^{2-}: 1.24 Å; F^-: 1.17 Å) allows easy substitution of oxygen generating one free electron into the lattice thereby increasing electrical conductivity with minimum distortion to the structure.[14, 139] The carrier concentration can also be increased by substituting the Zn^{2+} ion (ionic radius: 0.74 Å) with a group III trivalent cation such as boron, aluminium, gallium and indium (M^{3+} ionic radius: 0.23, 0.54, 0.62 and 0.80

Å, respectively.[135, 140] The focus has been mainly on the use of aluminium (Chapter 3) and gallium since boron is notoriously difficult to detect due its low mass and indium due to its increasing rarity and high cost resulting in no long-term prospects for viable uses in the production of TCOs.

GZOs have been particularly appealing because of the similar ionic radii of Ga^{3+} and Zn^{2+} which minimises lattice deformation furthermore than in AZOs.[63, 137, 141, 142] It is not clear cut which film, AZO or GZO has the superior optoelectronic properties as it very much depends on the method and conditions used to deposit the films. There are studies that state that aluminium is the better dopant as the energy of the valence s orbital of aluminium matches that of zinc and therefore there is less of a disruption to the conduction band. On the other hand, claims have been made that gallium is better as a consequence of Ga_2O_3 having a less exothermic enthalpy of formation compared with Al_2O_3 and hence more likely for Ga^{3+} to substitute the Zn^{2+} than form a non-conducting oxide.[143] Despite the idea of cation-cation doping does not seem rational due to both dopants competing for the same substitutional site, Al and Ga co-doped ZnO (AGZO) have been deposited by others.[110, 144, 145, 146] The rationale for producing AGZO other than for enhancing optoelectronic properties would be to offset the often-reported instability of AZO thin films produced by some deposition methods, whilst still benefiting from the greater abundance and availability of Al. A few studies have reported AGZO films to have excellent electrical properties. Notably, these studies have used magnetron sputtering to grow the films and reported electrical resistivities in the order of 10^{-4} Ω cm with transmittance greater than 80%[144, 145] however, not all AGZO films have been found to be better than singly-doped films.[110, 144, 146]

The alternative to AGZO films is cation-anion co-doping particularly as the merits of Ga or F doped ZnO films have been widely reported. Co-doping ZnO with Ga and F (GFZO) has been reported once. Shi *et al.* deposited GFZO films by magnetron sputtering with an electrical resistivities reaching orders of 10^{-4} Ω cm.[147] Whilst these values of resistivity are low the method used to deposit the films has key disadvantages including a requirement for a high vacuum and complex machinery which increase the cost of production.[10] PVD methods are also known to produce films with poor crystallinity leading to problems associated with grain boundaries and interfaces.[14] This chapter investigates single doped GZO films for comparison with single doped AZO films from Chapter 3 and explores for the first time co-doped GFZO films deposited *via* a CVD method.

4.2 Experimental

The depositions reported in this chapter were carried out using a two-pot system in a fume hood. An undoped zinc oxide film was made from glass bubbler one containing 0.50 g diethylzinc (15 wt.% in toluene) in ~20 mL dry toluene and the second holding ~25 mL dry methanol (an oxygen source) (Scheme 5). When GZO thin films were deposited the required mol% of triethyl gallium (2.0 M in toluene) was added to the diethylzinc and toluene mixture (Scheme 6). The co-doped GFZO film was deposited in the same manner as GZO with the addition of varying mol% amounts of ammonium fluoride (98%) in the dry methanol bubbler (Scheme 7). The precursors were all purchased from Sigma Aldrich. The solvents were purchased from Fischer Scientific. Toluene was stored under alumina columns and dried with anhydrous engineering equipment whereas the methanol was dried by distillation over magnesium turnings. All depositions were carried out under Nitrogen gas (≥99.9%) supplied by BOC at a flow rate of 1.0 L min^{-1} and a temperature of 450 °C. The baffle was connected to a baffle cooler using a garden pond pump. The mists produced using humidifiers were transported to and mixed in a Y-joint before entering the reactor. The depositions usually lasted between 25-35 minutes. The films were adherent and the coverage overall was approximately 50% of the substrate with the use of the baffle cooler as diethylzinc tends to crash out in the baffle during transportation to the reactor leading to a blockage. The films were transparent and colourless with no evidence to the naked eye (brown tints) of carbon contamination.

$$\mathrm{ZnEt_2 + MeOH \xrightarrow[450\ ^{\circ}C;\ N_2]{dry\ toluene} ZnO + waste} \qquad \text{(Scheme 5)}$$

$$\mathrm{ZnEt_2 + MeOH + GaEt_3 \xrightarrow[450\ ^{\circ}C;\ N_2]{dry\ toluene} GZO + waste} \qquad \text{(Scheme 6)}$$

$$\mathrm{ZnEt_2 + MeOH + GaEt_3 + NH_4F \xrightarrow[450\ ^{\circ}C;\ N_2]{dry\ toluene} GFZO + waste} \qquad \text{(Scheme 7)}$$

To avoid using air sensitive precursors, preliminary experiments tested the viability of using zinc acetate, zinc 2-ethylhexanoate and gallium acetylacetonate as precursors. However, the conductivities of the resultant films were unacceptably low.

The films discussed in the following chapter will be referred to as the amount of dopant(s) found in the bulk of the film rather than the amount present in the precursor solution.

4.2.1 Instrumental conditions

EDX and WDX calculations were carried out using the JEOL JSM-6301F field emission and Phillips ESEM, respectively. The Zn, Ga and F at.% was obtained from the Zn-K_α line (8638 eV), Ga-K_α (1487 eV) and F-K_α (676.8 eV) X-ray emission lines, respectively.

4.3 Results and discussion

4.3.1 AACVD of GZO films

Gallium doped zinc oxide thin films were deposited on SiO_2 barrier coated glass using various mol.% amounts (2.5, 5, 10 and 20 mol.%) of the gallium dopant, triethyl gallium, in the diethyl zinc and toluene mixture. The second bubbler contained dry methanol used as the oxygen source. Depositions were carried out at 450 °C using nitrogen as a carrier gas.

The reaction of the precursors in this chapter forms clusters similar to those mentioned in section 3.3.1.

4.3.1.1 Dopant quantities in the GZO films

Energy dispersive X-ray spectroscopy was used to determine the at.% gallium content in the bulk of the films. It was found that triethyl gallium is an effective dopant precursor as the relationship between the precursor concentrations in solution was approximately proportional to the amount found in the films. X-ray photoelectron spectroscopy found similar quantities of gallium, when etched at 200 seconds, supporting the EDX results (Table 4.1). The surface of the films analysed by XPS showed slightly lower Ga concentrations (between 3-9 at.%) than in the bulk.

The main difference between the two techniques is that EDX looks at the overall composition in the bulk of the film whereas XPS analyses a surface or slice within the film at a depth defined by the etch time.

Table 4.1. The relationship between mol.% in solution and at.% of gallium in the films, deposited at 450 °C, determined by energy dispersive X-ray and X-ray photoelectron spectroscopy at 200 seconds etch time.

mol.% in solution	at.% determined by EDX	at.% determined by XPS
2.5	1	0
5	5	5
10	8	10
20	16	18

From XPS data from the surface the oxidation state of Zn and Ga can also be determined. The Zn $2p_{3/2}$ transition occurred around 1021.4 eV corresponding to Zn^{2+} in a ZnO environment (Fig. 4.1a). The positioning and shape of the Ga $2p_{3/2}$ peak (approximately 1117.5 eV) indicates the presence of Ga^{3+} in an oxide environment (Fig. 4.1b) and there was no observable shift in the peaks with varying dopant concentrations. Fig. 4.1c shows the increasing Ga concentration in the doped films as the triethyl gallium concentration was increased in the precursor solution. For the $Zn_{0.99}Ga_{0.01}O$ film (Fig. 4.1c(i)) the gallium peaks were too small to be quantified. A study by Chen *et al.*[135] suggests that at low gallium loading, although the gallium may be present, XPS does not allow quantification of such low amounts and therefore for their lowest doped film an estimate of the Ga content was taken from an extrapolation of a linear relationship they found between the nominal Ga/Zn molar ratio in the precursor solution and the amount found in the film. This is not necessary here as we have values from EDX that indicates the presence of Ga in the film. The oxygen 1s peak did not alter in peak position when the ZnO lattice was doped, remaining at a value of about 530.2 eV.

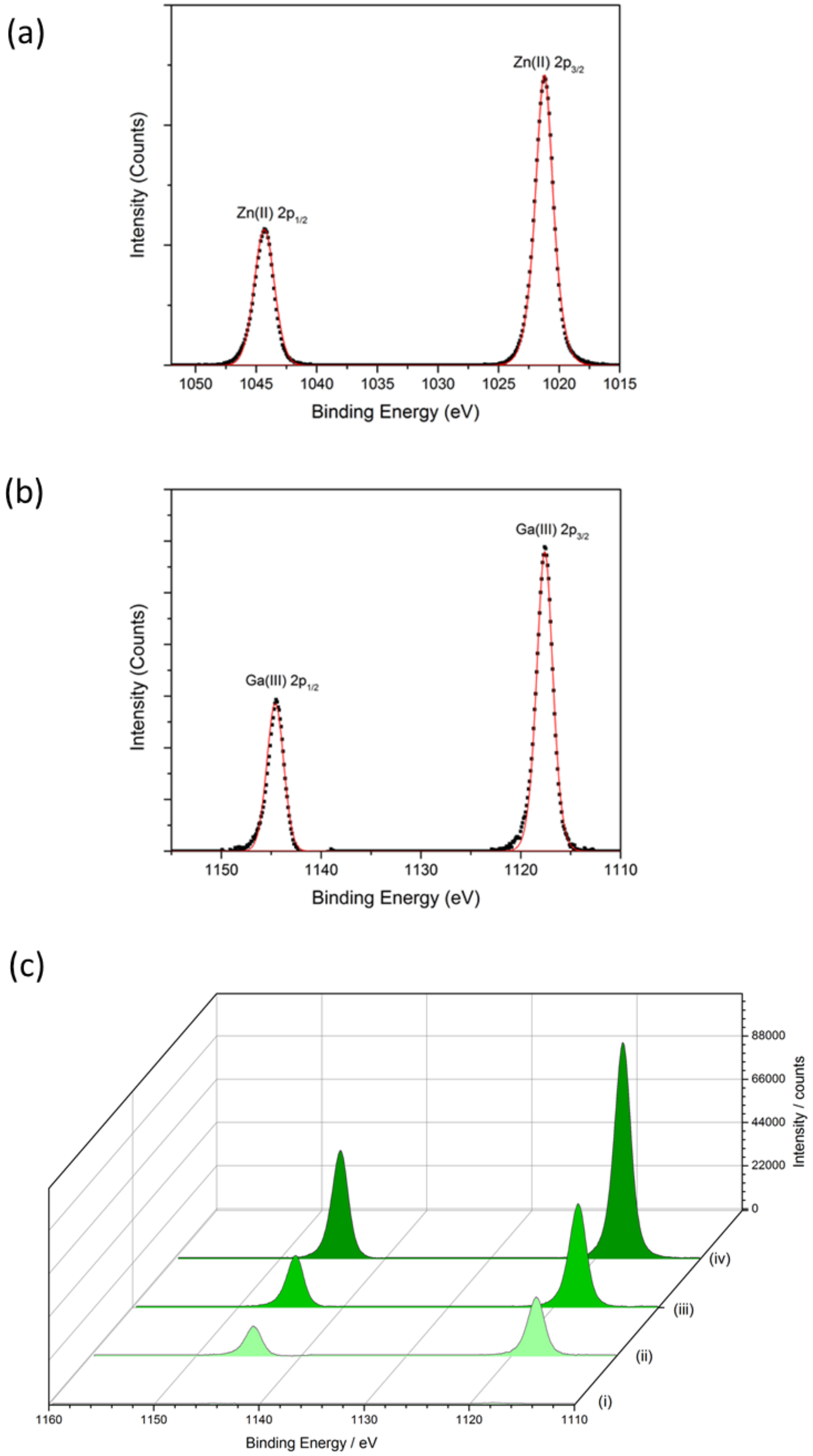

Fig. 4.1. Representative XPS spectra of (a) Zn $2p_{3/2}$ and $2p_{1/2}$ peaks, (b) Ga 2p $2p_{3/2}$ and $2p_{1/2}$ peaks and (c) the variation in Ga content in the films: (i) $Zn_{0.99}Ga_{0.01}O$ (ii) $Zn_{0.95}Ga_{0.05}O$ (iii) $Zn_{0.92}Ga_{0.08}O$ (iv) $Zn_{0.84}Ga_{0.16}O$.

4.3.1.2 Crystal structure

The addition of dopants into a lattice disrupts the crystal structure, the extent depending on the difference in the ionic radii of the dopant ions and those that they replace in the lattice. The crystallinity of a material is seen from X-ray diffraction patterns and Fig. 4.2 shows the patterns for the undoped ZnO and GZO thin films. The patterns were compared to a standard ZnO[126] and all films were polycrystalline, matching to wurtzite zinc oxide. As expected, crystallinity decreased with increasing dopant amounts, most notably at the highest dopant concentration, 16 at.%. The mean crystallite diameters were calculated using the Scherrer equation and are given in Table 4.2. A correlation was seen where the diameter decreased with increasing amounts of dopant incorporation. This fits well with the notion that a decrease in crystallite size reduces overall crystallinity. The Le Bail method was used to calculate the lattice parameters of the films by modelling the XRD patterns. The substitution of the Zn^{2+} ion (0.74 Å) with the smaller Ga^{3+} ion (0.62 Å) resulted in a predictable contraction in the unit cell.

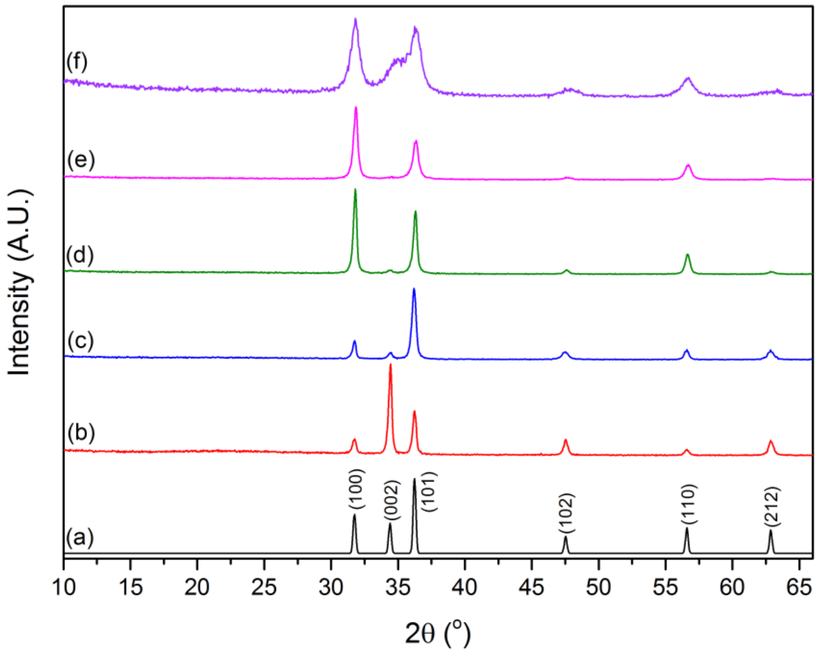

Fig. 4.2. XRD patterns of ZnO and GZO thin films deposited *via* dual source AACVD system at 450 °C. (a) standard ZnO[126] (b) undoped ZnO (c) $Zn_{0.99}Ga_{0.01}O$ (d) $Zn_{0.95}Ga_{0.05}O$ (e) $Zn_{0.92}Ga_{0.08}O$ (f) $Zn_{0.84}Ga_{0.16}O$.

Table 4.2. Variation in the mean crystallite diameter and unit cell parameters of ZnO and GZO thin films with different dopant concentrations of $GaEt_3$.

Film	**Mean crystallite diameter /nm**	**a /Å**	**c /Å**	**Unit cell volume /Å³**	**Volume contraction /%**
ZnO	23	3.2542(2)	5.2110(2)	47.791(5)	
$Zn_{0.99}Ga_{0.01}O$	20	3.2500(1)	5.2063(7)	47.625(6)	0.34
$Zn_{0.95}Ga_{0.05}O$	20	3.2493(1)	5.2058(7)	47.599(6)	0.40
$Zn_{0.92}Ga_{0.08}O$	17	3.2469(2)	5.2013(12)	47.487(10)	0.64
$Zn_{0.84}Ga_{0.16}O$	9	3.2515(5)	5.1685(17)	47.323(18)	0.98

The texture coefficients, based on the undoped ZnO film, were calculated for the $Zn_{0.99}Ga_{0.01}O$, $Zn_{0.95}Ga_{0.05}O$ and $Zn_{0.92}Ga_{0.08}O$ films (Fig. 4.3). The calculation was not performed on the $Zn_{0.84}Ga_{0.16}O$ film due to the relatively poor crystallinity of the film, as seen by the merging of the (002) and (101) peaks. The undoped zinc oxide film showed preferred orientation along the (002) plane and was calculated against a standard ZnO pattern.[126] The film with the lowest dopant incorporated into the ZnO lattice had preference along the (100), (101), (102) and (212) planes. The addition of 5 and 8 at.% Ga resulted in: a reduction in the coefficient of the preferred (101) plane; a four-fold increase in preference of the (100) plane; and a preference in the (110) plane. These findings align well with the patterns reported by Hu and Gordon who although used atmospheric pressure CVD, reported similar gallium quantities[111] and Binions *et al.* who used aerosol assisted CVD to produce films with comparable dopant amounts.[148]

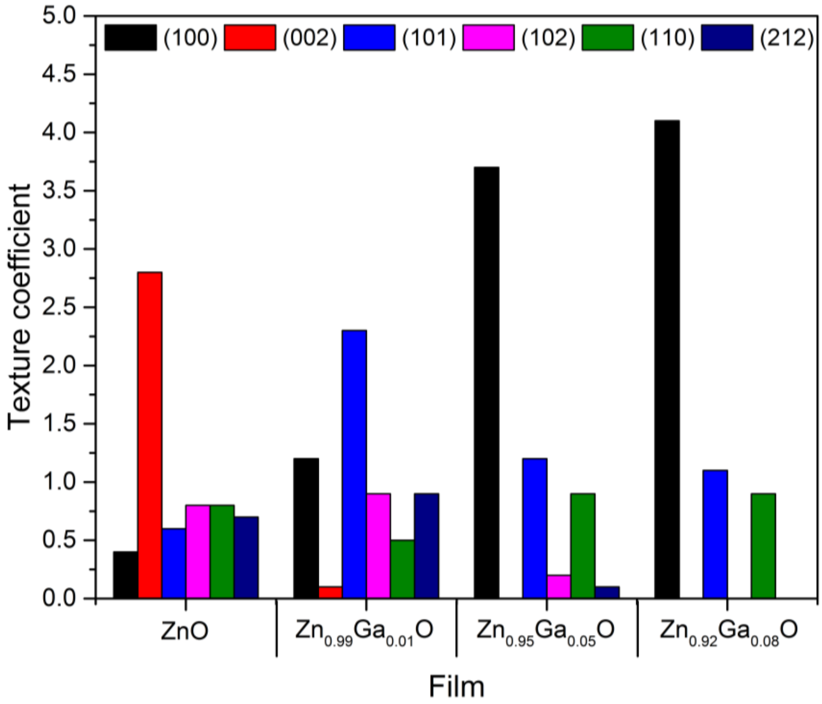

Fig. 4.3. Variation of the texture coefficient (Tc) of each plane with different gallium dopant amounts.

4.3.1.3 Surface morphology

The surface morphology and the thickness of the films were studied using top-down and side on scanning electron microscope, respectively (Fig. 4.4 and Table 4.3). The undoped ZnO thin film consisted of closely packed rounded clusters giving an overall flat morphology. The morphology changed when the ZnO lattice was doped with gallium. At the lowest dopant concentration, $Zn_{0.99}Ga_{0.01}O$, two distinct types of particle shapes are seen: pointed pyramidal (~475 nm) and rice-grain like (~330-520 nm) particles. Pyramidal morphology is known to be suited for solar cell applications as this type of surface texture allows light scattering and trapping.[14] When doped with 5 at.% gallium, the film landscape was dominated by small, mainly triangular, particles (~240 nm). The $Zn_{0.92}Ga_{0.08}O$ film no longer exhibited the defined particle shapes described above but showed particles that were more rounded (~100-240 nm). Doping with 16 at.% resulted in a heterogenous morphology consisting of discrete small particles sitting alongside irregular shaped dense clusters.

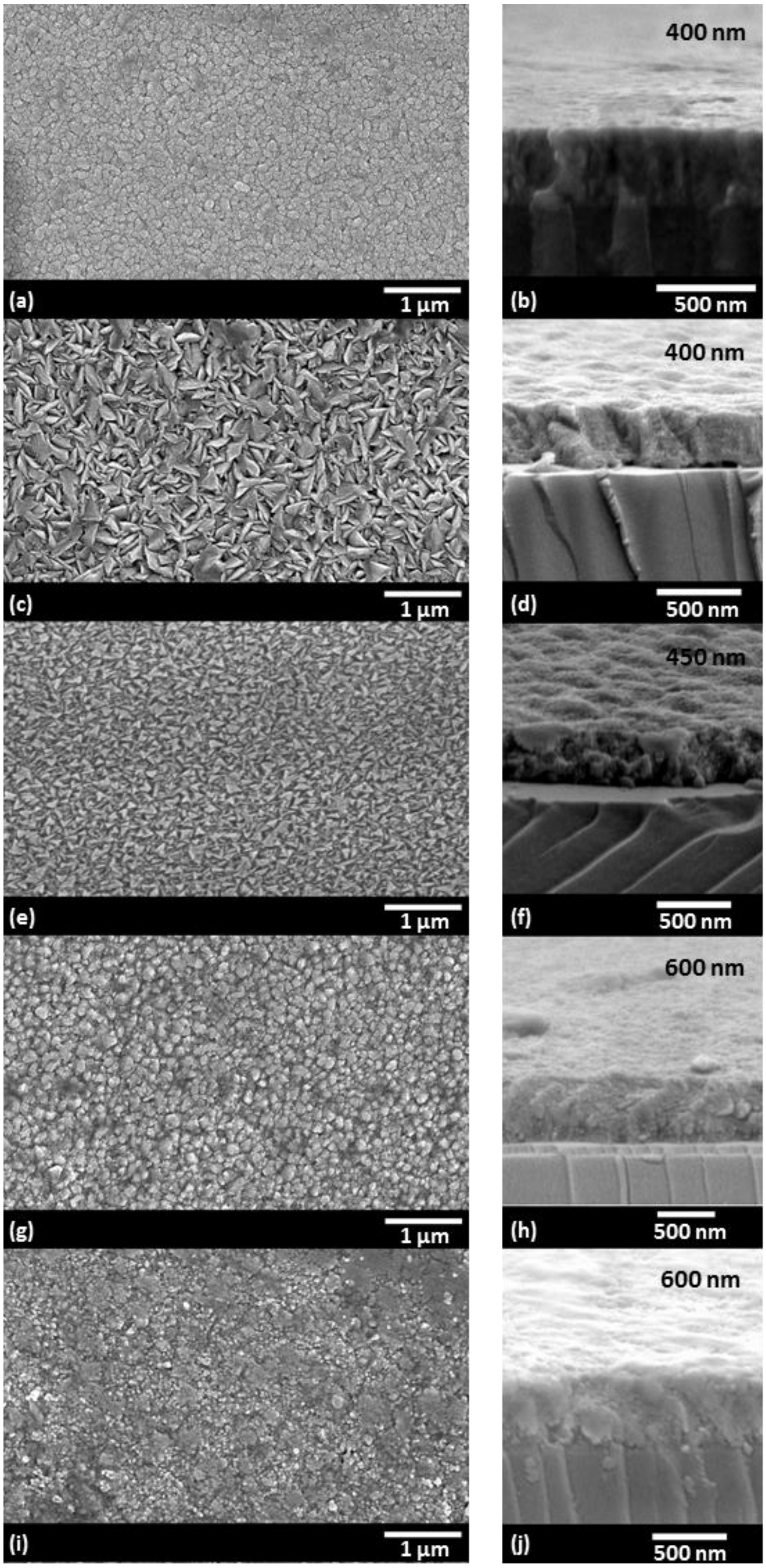

Fig. 4.4. Top down and side on SEM images of GZO thin films deposited *via* dual source AACVD at 450 °C. (a,b) undoped ZnO (c,d) $Zn_{0.99}Ga_{0.01}O$ (e,f) $Zn_{0.95}Ga_{0.05}O$ (g,h) $Zn_{0.92}Ga_{0.08}O$ and (i,j) $Zn_{0.84}Ga_{0.16}O$.

4.3.1.4 Optical measurements

Optical measurements of the undoped ZnO and GZO films were carried out using UV/visible/infrared spectroscopy. All films showed high transmittance across the visible (400-700 nm) range, above 80%, reaching a maximum of ~85% at the lower dopant concentrations (Fig. 4.5). With the exception of 16 at.% Ga, the reflectance property of the films in the infrared increased with dopant concentrations, reaching a maximum of ~80%. Furthermore, for these films the onset of the plasma absorption edge was blue shifted with increasing amounts of gallium dopant concentration. The highest dopant amount, $Zn_{0.84}Ga_{0.16}O$, resulted in a red-shift which coincides with a drop in charge carrier concentration (Fig. 4.5e and Table. 4.3), a factor known to affect the plasma edge. The band gap of each film was calculated using the Tauc plot.[13] The band gap was 3.3 eV for the nominally undoped, $Zn_{0.99}Ga_{0.01}O$ and $Zn_{0.95}Ga_{0.05}O$ thin films and increased to 3.5 eV for the higher doped $Zn_{0.92}Ga_{0.08}O$ and $Zn_{0.84}Ga_{0.16}O$ films. This follows the general trend of increasing carrier concentration (as seen *via* the Hall effect measurements) with increasing Ga in the ZnO films. Therefore, the increase in the optical band gap can be attributed to the Moss-Burstein effect.

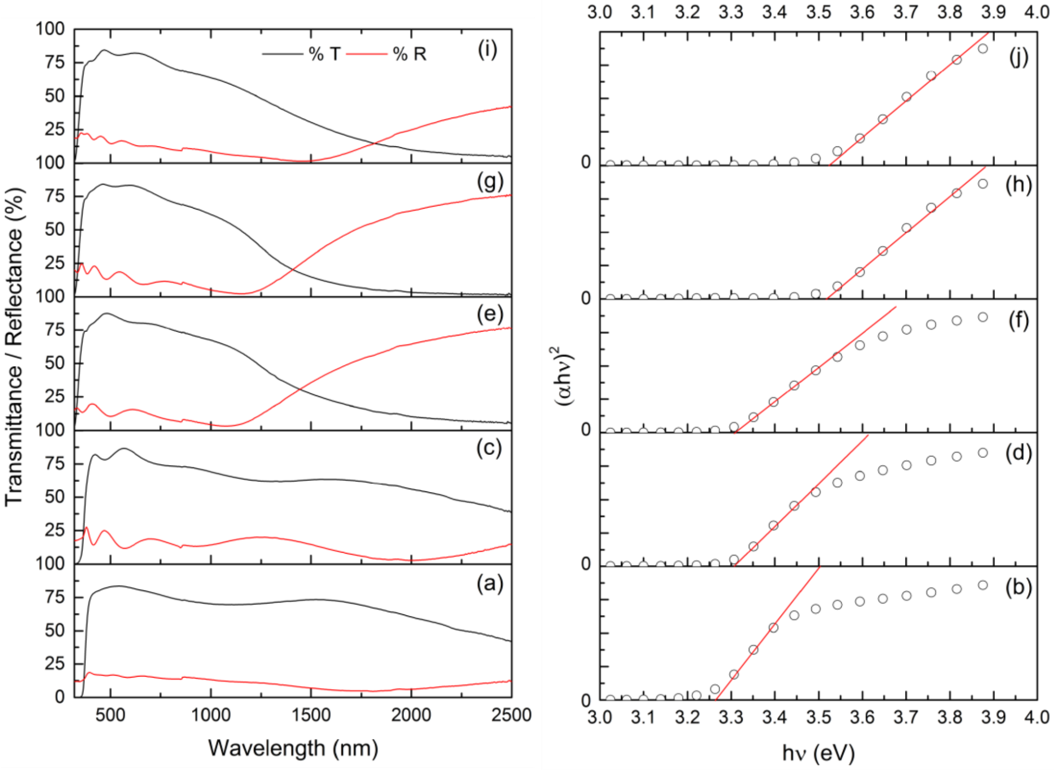

Fig. 4.5. Optical transmittance and reflectance spectra taken with an air background and the Tauc plots for ZnO and GZO thin films deposited at 450 °C. (a,b) undoped ZnO (c,d) $Zn_{0.99}Ga_{0.01}O$ (e,f) $Zn_{0.95}Ga_{0.05}O$ (g,h) $Zn_{0.92}Ga_{0.08}O$ (i,j) $Zn_{0.84}Ga_{0.16}O$.

4.3.1.5 Electrical properties

Hall effect measurements identified all the films as n-type. As expected, the doped films exhibited better electrical conductivities than the undoped ZnO (Table 4.3). It is known that an increase in charge carrier concentration can lead to a reduction in mobility as a consequence of grain boundaries trapping charge carriers and increased frequency of collisions between charge carriers. This in turn would lead to an increase in resistivity. The charge carrier concentration of the doped films increased before decreasing for the highest dopant concentration. This could be a consequence of the greater contraction of the lattice which despite containing the highest amount of dopant, somehow leads to a hindrance in the availability of the electrons to carry charge. However, this would require further investigation which is beyond the scope of the thesis. The films with 5 at.% Ga or more showed a decrease in mobility paralleled with an increase in resistivity. The film thicknesses calculated from side on SEMs (Fig. 4.4) show films get thicker with increased dopant amounts. Taking the thickness into account, the sheet resistance was calculated which showed the lowest resistivity of 17.6 $\Omega\ \square^{-1}$ for the film with 5 at.% Ga. This represents a 3-fold reduction in sheet resistance compared with the undoped ZnO film alongside a 3-fold increase in charge carrier concentration. The same film also had good optical properties. For these reasons, the deposition conditions for this film were chosen to investigate the properties of co-doped GFZO thin films.

Table 4.3. Hall effect measurements and film thicknesses of ZnO and GZO films. *d*, film thickness; *n*, charge carrier concentration; *μ*, charge carrier mobility; *ρ*, bulk resistivity; R_{sh}, sheet resistance.[*]

Film	d/nm	n/ $\times 10^{20}$ cm^{-3}	μ/cm^2 V^{-1} s^{-1}	ρ/ $\times 10^{-3}$ Ω cm	R_{sh}/$\Omega\ \square^{-1}$
ZnO	400	1.362	21.4	2.142	53.6
$Zn_{0.99}Ga_{0.01}O$	400	2.963	15.1	1.399	35.0
$Zn_{0.95}Ga_{0.05}O$	450	4.230	18.7	0.790	17.6
$Zn_{0.92}Ga_{0.08}O$	600	6.547	7.7	1.239	20.7
$Zn_{0.84}Ga_{0.16}O$	600	4.716	6.8	1.936	32.3

---

[*] The electrical properties for the undoped ZnO thin film in this chapter differs from the value given in Chapter 3, this is primarily due the slightly different synthetic procedure.

4.3.2 AACVD of GFZO films

Based on the optimum conditions found for GZO thin films (5 mol.% triethyl gallium in a diethyl zinc and toluene mixture), varying amounts of ammonium fluoride was added to the dry methanol solution to produce co-doped thin films of GFZO. Films were deposited on SiO_2 barrier coated glass at 450 °C using nitrogen as the carrier gas.

4.3.2.1 Dopant quantities in the GFZO films

The conditions for the $Zn_{0.95}Ga_{0.05}O$ film were replicated to produce films with 5 at.% Ga which was doped with varying amounts of fluorine. The quantities of the dopants were calculated using EDX for Ga and WDX for F (Table 4.4). Fluorine is a relatively light element making it difficult to detect so sometimes requires the more sensitive technique, WDX, to be analysed especially at dopant concentrations. EDX confirmed the reproducibility of the film, where 5 mol.% Ga in solution resulted in 5 at.% in the bulk of the films. The fluorine content in the bulk was quantified by WDX where 5, 10 and 20 mol.% F in solution gave 0.3, 1 and 2 at.% in the films, respectively. As described in section 3.3.2 the availability of fluorine for incorporating into the film is greatly restricted due to the decomposition of the ammonium fluoride precursor into hydrogen fluoride (see Equation 3.1).

XPS was also used to determine the gallium concentration in the films by calculating the amount from 200 second etch time (Table 4.4). Only one film showed the same at.% of Ga determined by EDX and XPS as seen from the GZO films. In the other two cases the XPS value was lower but no plausible explanation can be given for this discrepancy. The surface of the films showed much lower Ga concentrations, between 0.4-2 at.%, than in the bulk. The oxidation states were the same as before: Zn^{2+} and Ga^{3+}. The binding energy values of the Zn $2p_{3/2}$ and $2p_{1/2}$ peaks and O 1s peak were unaltered from the GZO films. However, the Ga $2p_{3/2}$ and $2p_{1/2}$ peaks shifted to slightly higher energies (from 1117.3 eV to 1118.0 eV) with increasing amounts of the more electronegative fluorine substituting for oxygen in the lattice.

Table 4.4. The relationship between mol.% in solution and at.% of gallium and fluorine in the films, deposited at 450 °C, determined by energy dispersive X-ray, wavelength dispersive X-ray and X-ray photoelectron spectroscopy from 200 second etch time.

mol.% of Ga in solution	mol.% of F in solution	at.% of Ga determined by EDX	at.% of Ga determined by XPS	at.% of F determined by WDX
5	5	5	1	0.3
5	10	5	2	1
5	20	5	5	2

4.3.2.2 Crystal structure

The X-ray diffraction patterns for the co-doped GFZO thin films are shown in Fig. 4.6. The films were polycrystalline with no significant observable deterioration in crystallinity in comparison with the singly doped GZO film, $Zn_{0.95}Ga_{0.05}O$, possibly due to the low dopant amounts of fluorine in the films. Other studies have shown that doping with fluorine alone into a ZnO lattice can result in the broadening of the XRD peaks and hence a reduction in crystallinity.[117, 149] The mean crystallite sizes showed no obvious correlation with dopant amounts, matching closely to undoped ZnO (Table. 4.5). The substitution of the Zn^{2+} ion (0.74 Å) with the smaller Ga^{3+} ion (0.62 Å) and O^{2-} ion (1.24 Å) with the closely sized F^{-} ion (1.17 Å) resulted in the expected contraction of the unit cell.

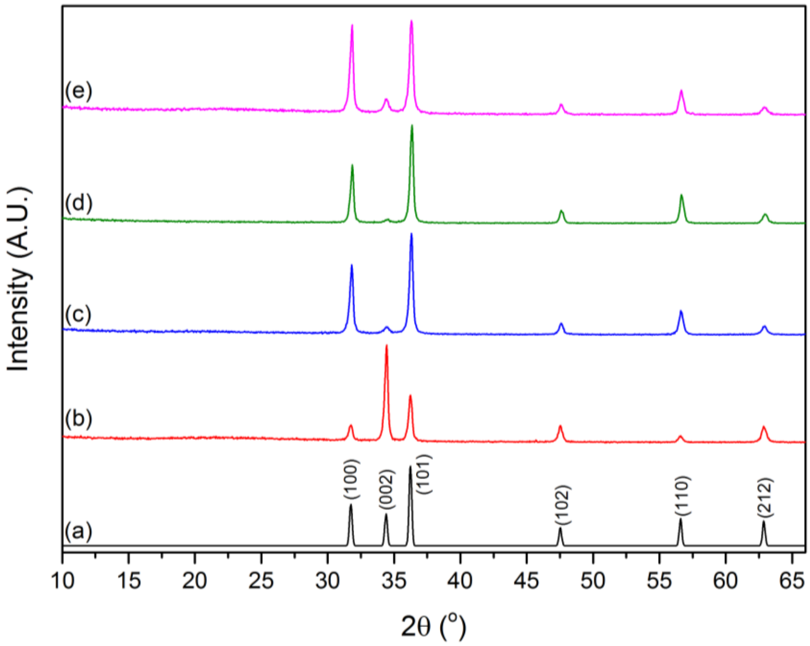

Fig. 4.6. XRD patterns of ZnO and GFZO thin films deposited *via* dual source AACVD system at 450 °C. (a) standard ZnO[126] (b) undoped ZnO (c) $Zn_{0.947}Ga_{0.05}F_{0.003}O$ (d) $Zn_{0.94}Ga_{0.05}F_{0.01}O$ (e) $Zn_{0.93}Ga_{0.05}F_{0.02}O$.

Table 4.5. Variation in the mean crystallite diameter and unit cell parameters of ZnO and GFZO thin films with the 5 at.% gallium and varying dopant concentrations of NH_4F.

Film	Mean crystallite diameter /nm	a /Å	c /Å	Unit cell volume /Å³	Volume contraction /%
ZnO	23	3.2542(2)	5.2110(2)	47.791(5)	
$Zn_{0.947}Ga_{0.05}F_{0.003}O$	23	3.2488(1)	5.2083(5)	47.608(4)	0.38
$Zn_{0.94}Ga_{0.05}F_{0.01}O$	24	3.2467(1)	5.2019(5)	47.494(5)	0.62
$Zn_{0.93}Ga_{0.05}F_{0.02}O$	22	3.2433(3)	5.1810(26)	47.197(22)	1.25

Texture coefficient calculations showed that undoped ZnO thin film had preferred growth orientation along the (002) plane whereas the co-doped films had growth preference in the (100), (101) and (110) plane as exhibited by the singly doped $Zn_{0.95}Ga_{0.05}O$ film suggesting that fluorine has little or no influence on the growth of the film (Fig. 4.7). This was also observed when ZnO was co-doped with Al and F (Section 3.3.3.1.).

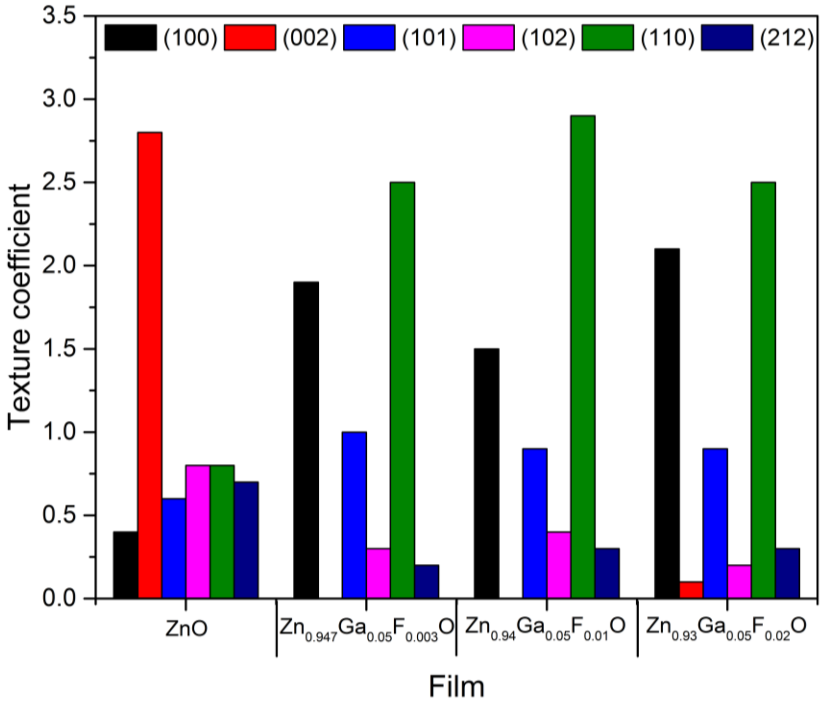

Fig. 4.7. Variation of the texture coefficient (Tc) of each plane with 5 at.% Ga and different fluorine dopant amounts.

4.3.2.3 Surface morphology

The surface morphology and side on SEM of the co-doped GFZO films were compared with the $Zn_{0.95}Ga_{0.05}O$ film that showed the best optoelectronic properties in section 4.3.1.3 (Fig. 4.8). The addition of fluorine resulted in the loss of the sharpness of the particles causing them to become smooth edged. This is supported by a study by Shi *et al*. who deposited GFZO films *via* a sputtering technique and found that the morphology consisted of closely compact particles resulting in a smooth surface. Furthermore, the particles showed greater variation in size. Fluorine incorporation above 1 at.% resulted in a greater abundance of much smaller irregular particles.

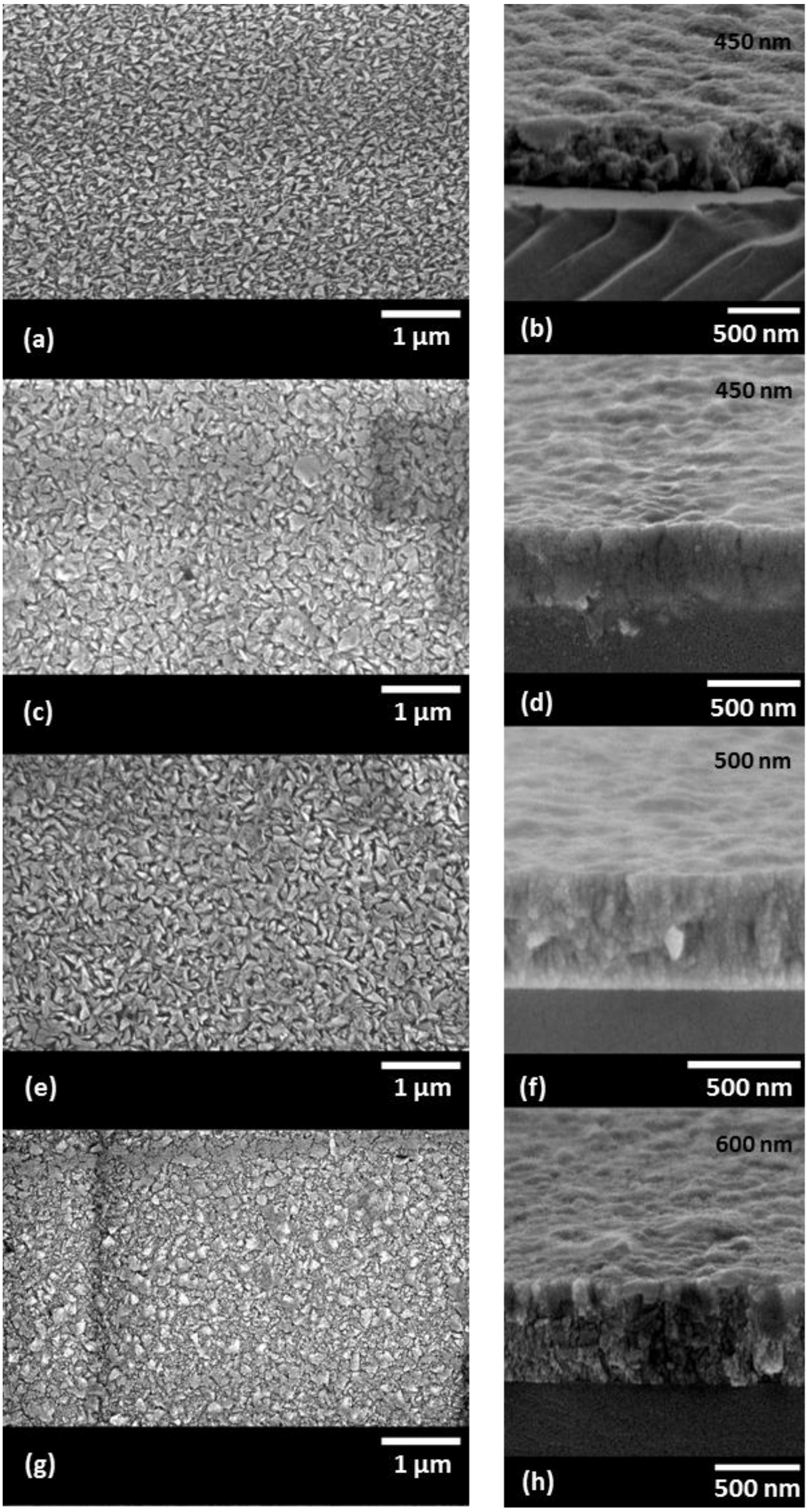

Fig. 4.8. Top down and side on SEM images of GFZO thin films (compared with 5 at.% GZO) deposited *via* dual source AACVD at 450 °C. (a,b) $Zn_{0.95}Ga_{0.05}O$ (c,d) $Zn_{0.947}Ga_{0.05}F_{0.003}O$ (e,f) $Zn_{0.94}Ga_{0.05}F_{0.01}O$ and (g,h) $Zn_{0.93}Ga_{0.05}F_{0.02}O$.

4.3.2.4 Optical measurements

The gallium and fluorine co-doped films had high transmittance, 80-85%, across the visible range (400-700 nm) and exhibited high reflectance in the infrared reaching a maximum of ~80% (Fig. 4.9). The spectra obtained for the GFZO films were similar to the single doped $Zn_{0.95}Ga_{0.05}O$ film. The plasma absorption edge was blue shifted compared with undoped ZnO but by a lesser extent when compared with the GZO film exhibiting the best optoelectronic performance. The extent of the blue shift did not always correspond to the expected trend between the wavelength and charge carrier concentration (Section 1.1). The band gap was greater compared with the singly doped GZO films (3.4 eV); the band gap was 3.6 eV for $Zn_{0.93}Ga_{0.05}F_{0.02}O$ film and 3.5 eV for the other two co-doped films.

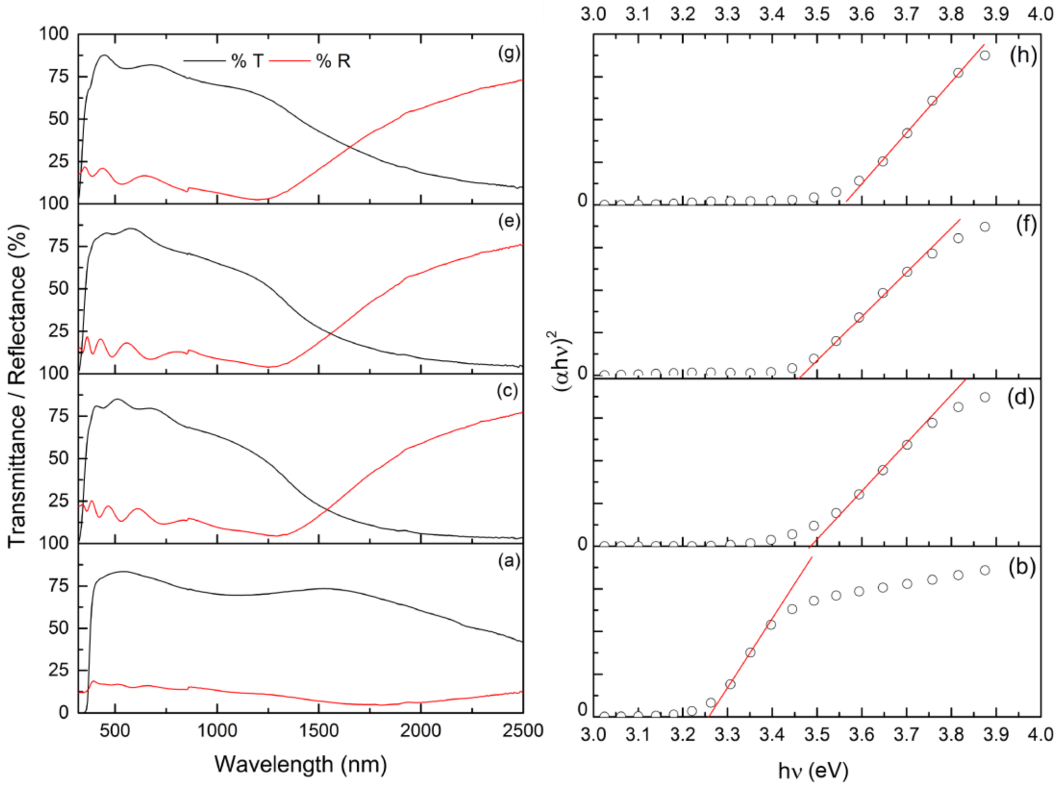

Fig. 4.9. Optical transmittance and reflectance spectra taken with an air background and the Tauc plots for ZnO and GFZO thin films deposited at 450 °C. (a,b) undoped ZnO (c,d) $Zn_{0.947}Ga_{0.05}F_{0.003}O$ (e,f) $Zn_{0.94}Ga_{0.05}F_{0.01}O$ (g,h) $Zn_{0.93}Ga_{0.05}F_{0.02}O$.

4.3.2.5 Electrical properties

The co-doped films were also identified as n-type from the negative Hall coefficients obtained from Hall effect measurements (Table 4.6). The charge carrier concentration increased before decreasing with 2 at.% F present. Furthermore, the $Zn_{0.93}Ga_{0.05}F_{0.02}O$ film had the lowest mobility and hence greatest resistivity. Again, this can be attributed to the more marked lattice contraction reducing the availability of charge carriers. Taking film thickness into consideration, which once again increased with more dopant incorporation, the optimum film was found to be $Zn_{0.94}Ga_{0.05}F_{0.01}O$ having a sheet resistance of 12.2 $\Omega\ \square^{-1}$ which is better than the corresponding singly doped $Zn_{0.93}Ga_{0.05}O$ film (Table 4.3). To my knowledge there is only one published report on the production of GFZO films. Shi *et al.* deposited a film *via* sputtering, a PVD technique, with high transmittance but with a resistivity (19.7 $\Omega\ \square^{-1}$) higher than that reported in the present study.[147]

Table 4.6. Hall effect measurements and film thicknesses of ZnO and GFZO films. *d*, film thickness; *n*, charge carrier concentration; *μ*, charge carrier mobility; *ρ*, bulk resistivity; R_{sh}, sheet resistance.[*]

Film	*d*/nm	*n*/ ×10^20 cm^-3	*μ*/cm^2 V^-1 s^-1	*ρ*/×10^-3 Ω cm	$R_{sh}/\Omega\ \square^{-1}$
ZnO	400	1.362	21.4	2.142	53.6
$Zn_{0.947}Ga_{0.05}F_{0.003}O$	450	6.016	13.17	0.788	17.5
$Zn_{0.94}Ga_{0.05}F_{0.01}O$	500	7.523	13.63	0.609	12.2
$Zn_{0.93}Ga_{0.05}F_{0.02}O$	600	3.490	10.94	1.635	27.3

---

[*] The electrical properties for the undoped ZnO thin film in this chapter differs from the value given in Chapter 3, this is primarily due the slightly different synthetic procedure.

4.4 Conclusions

Thin films of GZO and GFZO were deposited with excellent coverage and adherence on glass substrates *via* aerosol assisted chemical vapour deposition (AACVD). The composition of the films were quantified using EDX, WDX and XPS; triethyl gallium proved to be an efficient precursor resulting in high transparent and conductive films. The films were polycrystalline and as expected the unit cells underwent a contraction. All the films in this chapter showed excellent transmittance in the visible (>80%) and, apart from undoped ZnO and $Zn_{0.99}Ga_{0.01}O$, exhibited high reflectance in the infrared. The plasma absorption edge was shifted to wavelengths in the range 1100-1500 nm, with the greatest blue shift seen in the single doped $Zn_{0.95}Ga_{0.05}O$ film. This film also demonstrated the best sheet resistance of the singly doped films. Therefore, the deposition conditions for the $Zn_{0.95}Ga_{0.05}O$ film were used to deposit co-doped films. The conductivities of the GFZO films were just as impressive, with the addition of 1 at.% fluorine to the GZO lattice lowering resistivity's to 12.2 $\Omega\ \square^{-1}$. The surface morphology of the GZO films displayed a variation in particle shape and size depending on atomic amounts of gallium incorporated into the lattice. Upon co-doping with fluorine the particles became smoother and more variable in size. Like the GZO films, the GFZO films also showed high transmittance meeting the requirement of a TCO as well as having high reflectance in the infrared region. The onset of the plasma absorption edge was marginally red-shifted compared with the best performing GZO film, $Zn_{0.95}Ga_{0.05}O$, however this was offset by the lower sheet resistance for the best GFZO film, $Zn_{0.94}Ga_{0.05}F_{0.01}O$. Hence, the optoelectronic properties can be tuned by varying the dopant concentration.

Chapter 5 will move onto exploring the optoelectronic properties of doping the SnO_2 lattice with antimony. Antimony is an ideal dopant because of its similar ionic radius to that of tin and has been shown to be an effective dopant when films have been deposited *via* a variety of methods but thus far none which employed AACVD. In addition, due to already established excellent optoelectronic properties of fluorine doped tin oxide (FTO), fluorine will be co-doped alongside antimony into SnO_2.

5

Antimony doped and antimony-fluorine co-doped tin(IV) oxide thin films

This chapter explores the potential of antimony doped tin(IV) oxide (ATO) and antimony and fluorine doped tin(IV) oxide (AFTO) thin films for architectural and optoelectronic applications. The films were deposited using a standard single pot aerosol assisted CVD resulting in stable coloured films achieving full coverage of the substrate. The effects of dopant concentrations were analysed.

5.1 Introduction

Tin(IV) oxide, SnO_2, is a wide band gap n-type semiconductor with a direct value of 3.6 eV. Tin doped indium oxide (ITO) is currently the market leader offering a wide range of optoelectronic applications. However, the lower abundance and greater cost of indium as well as the increasing demand for electronic devices requires research into seeking comparable alternatives that are cost effective and sustainable.[6, 150] Thin films produced from SnO_2 offer a wide range of applications including solar cells, gas sensors, catalysis, electronics and optics.[151, 152] In addition, most architectural glass on building windows use tin-oxide based TCOs which are increasingly in demand.[65]

The enhancement of electrical properties can be achieved by intrinsic defects, including oxygen vacancies, or by introducing extrinsic defects through doping with for example higher valency cations.[153] The electrical resistivity is dependent on the density of charge carriers and their mobility[154] and for undoped SnO_2 resistivity is limited to 10^{-2} - 10^{-3} Ω cm.[151] However, over-doping is not desirable as this is known to increase electrical resistivity and reduce optical transparency.[38, 155] Dopants such as fluorine and antimony have been used to great effect in improving the n-type conductivity of SnO_2 films.[20, 156, 157, 158, 159, 160] Antimony-doped tin(IV) oxide (ATO) materials have received particular attention in the production of coloured glass.[20] The doped SnO_2 structure contains Sb in the +3 and +5 states with Sb(V) responsible for the enhancement of the electrical conductivity. The consensus is that both oxidation states are present in the antimony doped films with more Sb^{5+} replacing the Sn^{4+} site due to its smaller ionic radii (Sn^{4+} = 0.69 Å; Sb^{5+} = 0.60 Å; Sb^{3+} = 0.74 Å).

Fluorine doped tin(IV) oxide (FTO) films are commercially used for applications such as solar cells and low emissivity coatings for windows. Fluorine is incorporated into the lattice as each O^{2-} ion (1.24 Å) is substituted with an F^- ion (1.17 Å) and hence introducing more free electrons. The best commercially available FTO films have a sheet resistance in the range 7-15 $\Omega\ \square^{-1}$ (Pilkington NSG). Therefore, exploring the possibility of improving the properties of such films by co-doping would be attractive, particularly if the method employed to do so is also low cost. A number of attempts have been made to produce co-doped AFTO films using a range of precursors and deposition methods but with varying degrees of success. Gaewdang and Wongcharoen found that their co-doped film had a resistivity value of 2.3×10^{-3} Ω cm which was inferior to their single-doped films.[161] Whilst others have found greater conductivities for their co-doped films, the conductivities for the single-doped films were not reported to allow comparison nor were the amounts of Sb or F at.% present in the films.[162, 163] Clearly, there is a need for a more comprehensive study into the effects of co-doping with Sb and F into SnO_2 for optoelectronic applications.

5.2 Experimental

The depositions in this chapter were carried out using the standard single pot AACVD rig (Fig. 1.18) in a fume hood. An undoped tin(IV) oxide film was made from the glass bubbler containing 0.30 g butyltin trichloride in 10 mL methanol (Scheme 8). When ATO and AFTO thin films were deposited the required mol% of antimony(III) ethoxide for all films and ammonium fluoride for only the latter films were added to the bubbler (Schemes 9 and 10). The precursors were all purchased from Sigma Aldrich. The solvents were purchased from Fischer Scientific. All depositions were carried out in air (≥99.9%) supplied by BOC at a flow rate of 1.0 L min^{-1} and a temperature of 450 °C. The mist was produced using a humidifier and transported to the reactor. The depositions usually lasted between 10-20 minutes. The films were adherent with full coverage of the substrate and they were transparent with a blue or black colouration for ATO and AFTO, respectively, which darkened with increasing amounts of antimony incorporation into the SnO_2 lattice.

$$\mathrm{BuSnCl_3} \xrightarrow[450\ ^\circ\mathrm{C;\ Air}]{\mathrm{MeOH}} \mathrm{SnO_2 + waste} \qquad \text{(Scheme 8)}$$

$$\mathrm{BuSnCl_3 + Sb(OEt)_3} \xrightarrow[450\ ^\circ\mathrm{C;\ Air}]{\mathrm{MeOH}} \mathrm{ATO + waste} \qquad \text{(Scheme 9)}$$

$$\mathrm{BuSnCl_3 + Sb(OEt)_3 + NH_4F} \xrightarrow[450\ ^\circ\mathrm{C;\ Air}]{\mathrm{MeOH}} \mathrm{AFTO + waste} \qquad \text{(Scheme 10)}$$

Preliminary experiments were carried out using antimony(III) acetate and antimony(V) chloride as dopant precursors but proved to be unsuccessful. Furthermore, antimony(III) fluoride and antimony(V) fluoride were used in order to co-dope using a single precursor. Unfortunately, the resultant films had no detectable antimony.

The films discussed in the following chapter will be referred to as the amount of dopant(s) found in the bulk of the film rather than the amount present in the precursor solution.

5.2.1 Instrumental conditions

WDX calculations were carried out using the Phillips ESEM. The Sn, Sb and F at.% was obtained from the Sn-L_α line (3444 eV), Sb-L_α (3605 eV) and F-K_α (676.8 eV) X-ray emission lines, respectively.

5.3 Results and discussion

5.3.1 AACVD of ATO films

Antimony doped tin(IV) oxide thin films were deposited on SiO_2 barrier coated glass using butyltin trichloride and various mol.% amounts (5, 10, 15 and 20 mol.%) of the antimony dopant, antimony(III) ethoxide, in a methanol solution at 450 °C using air as the carrier gas.

Unlike diethylzinc which forms complex clusters when it reacts (Chapters 3 and 4), butlytin trichloride reacts with antimony (III) ethoxide *via* a ligand exchange mechanism.

5.3.1.1 Dopant quantities in the ATO films

Wavelength dispersive X-ray spectroscopy was used to determine the % antimony content in the bulk of the films. In previous film analysis EDX has been used to quantify at.% amounts of elements present in the film but this method was not suitable for this system as the antimony peaks overlapped with the tin peaks thus making the two elements indistinguishable. The results showed a positive correlation between the concentration of $Sb(OEt)_3$ in the precursor solution and the concentration found in the films (Table 5.1). X-ray photoelectron spectroscopy showed the presence of 1-2 at.% Sb on the surface of the film, suggesting that $Sb(OEt)_3$ does not surface segregate. The antimony amounts in the films were of the same order when etched for 200 seconds.

Table 5.1. The relationship between mol.% in solution and at.% of antimony in the films, deposited at 450 °C, determined by wavelength dispersive X-ray and X-ray photoelectron spectroscopy at the surface.

mol.% in solution	at.% determined by WDX	at.% determined by XPS
5	1	1
10	4	2
15	7	1
20	10	2

The oxidation state of the tin was confirmed to be Sn^{4+} with the Sn $3d_{5/2}$ peak centred at 486.5–486.6 eV for all films therefore the presence of Sn^{2+} can be discounted. Due to the heavy overlap between the Sb $3d_{5/2}$ and the O 1s transitions, the less intense

Sb $3d_{3/2}$ peak was used to determine the position and intensity of the more intense Sb $3d_{5/2}$. The overlapping Sb $3d_{5/2}$ and O 1s peak was modelled with a spin orbit split of 9.39 eV and the Sb $3d_{5/2}$ peak intensity is 1.5 times greater than the Sb $3d_{3/2}$. Due to the similar peak positions of the Sb(V) and Sb(III) it is not possible to determine the oxidation state of Sb form XPS alone, especially at dopant concentrations where signal to noise in the spectra can be low. For the Sb doped samples in this study the $Sb_{3/2}$ peaks appears between 539.3–539.6 eV.

Valence band (VB) photoelectron spectra for the undoped and ATO films are shown in figure 5.1c. All spectra show the three peaks that are composed of O 2p states as expected for SnO_2. The overall O 2p band width is roughly 9 eV. Apart from some peak broadening there was little change in the VB due to Sb doping. No electronic states were detected within the band gap due to doping which is unusual as normally a peak is expected 0.5 eV below the Fermi level indicating conduction band filling upon semiconductor to metal transition. The absence of this peak maybe due to Sb being primarily a bulk dopant in the AACVD grown films. This also follows from core level XPS and WDX results that showed Sb levels at the surface being much lower than in the bulk therefore suggesting bulk segregation.

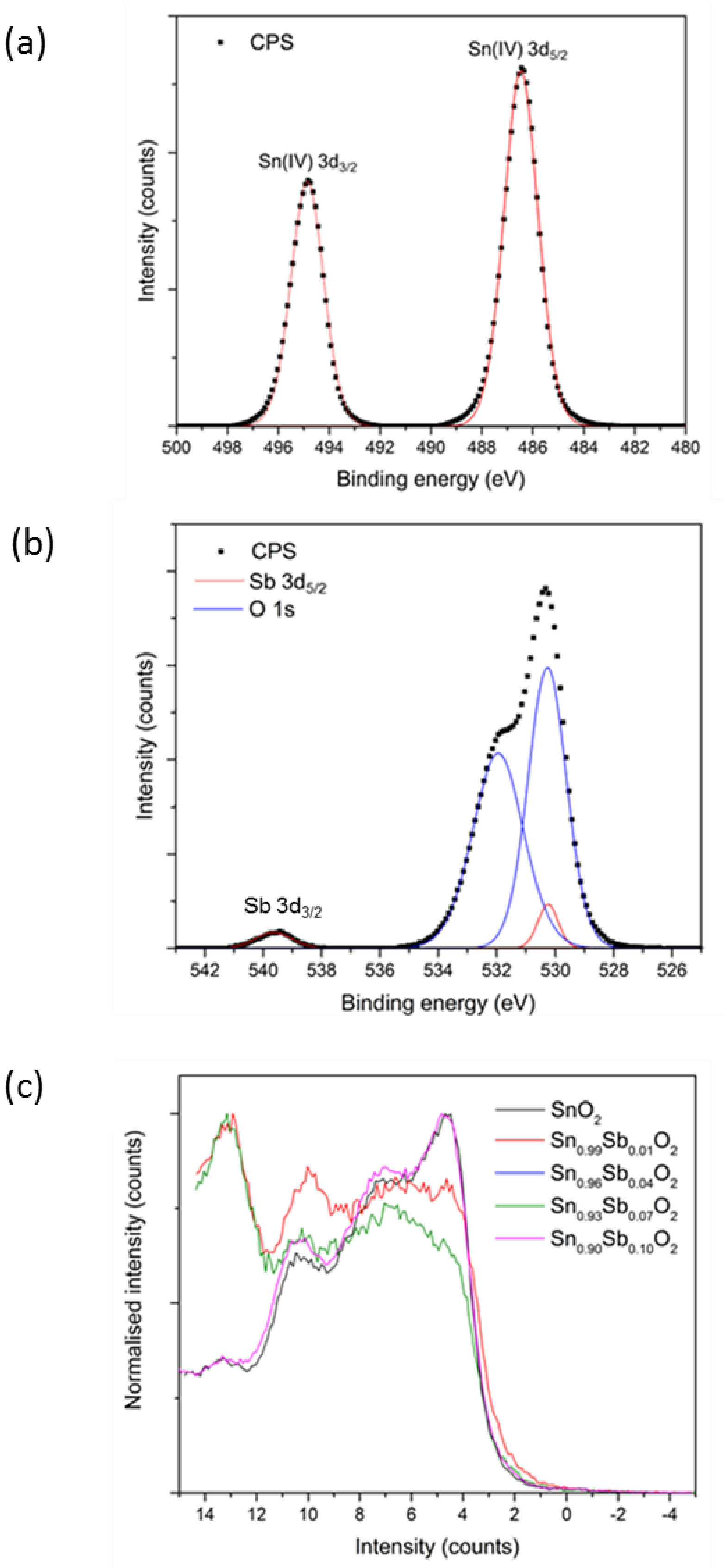

Fig. 5.1. Representative XPS spectra of (a) Sn $3d_{5/2}$ and $3d_{3/2}$ peaks, (b) Sb $3d_{3/2}$ and the overlap of O 1s with Sb $3d_{5/2}$ and (c) valence band spectra.

5.3.1.2 Crystal structure

The X-ray diffraction patterns of the films showed all films were polycrystalline, confirming the presence of the tetragonal rutile phase with no observable peaks for a secondary SbO_x phase (or a significant amorphous component) even at high dopant concentrations (Fig, 5.2). The crystallinity of the films did not notably decrease with increasing dopant amounts. The mean crystallite diameters were calculated and are shown in Table 5.2. The mean crystallite size in the doped films was slightly greater than the undoped SnO_2 film, however no trend was seen with regards to the varying dopant amounts. The greater crystallite size maybe a consequence of the dynamics of film growth in forming a thicker film. The substrate being amorphous would initially produce film layers with low crystallinity and in turn smaller crystallite sizes. However, each subsequent layer would act as a template for the next layer growth resulting in an increase in the crystallite size. Hence, thicker films would have larger crystallite sizes, an effect previously observed by Sathasivam *et al.*[164] investigating the deposition of GaAs films *via* AACVD. Le Bail modelling of the XRD patterns showed that doping of SnO_2 with Sb generally results in a contraction of the cassiterite unit cell (Table 5.2). This follows what is expected for the substitutional doping of Sb^{5+} as its ionic radii is only 0.60 Å whereas Sn^{4+} is 0.69 Å. The apparent expansion observed in the unit cell of the $Sn_{0.99}Sb_{0.01}O_2$ film is probably a consequence of the tendency of Sb to remain in the +3 oxidation state at lower dopant concentrations. At high Sb doping concentration (10 at.%) there was an increase in unit cell size compared to 4 and 7 at.%, which is most likely due to the incorporation of Sb^{3+} (radii of 0.74 Å) ions as well as the desired Sb^{5+} into the lattice. The substitution of a smaller cation should also shift the XRD peaks to higher angles. However, Li *et al.* explained why the shift is not always seen by suggesting that interstitial Sb^{3+}/Sb^{5+} might increase the cell volume, despite this process not being energetically favourable, hence negating the apparent effect of the substitution of Sn^{4+} with Sb^{5+}.[165]

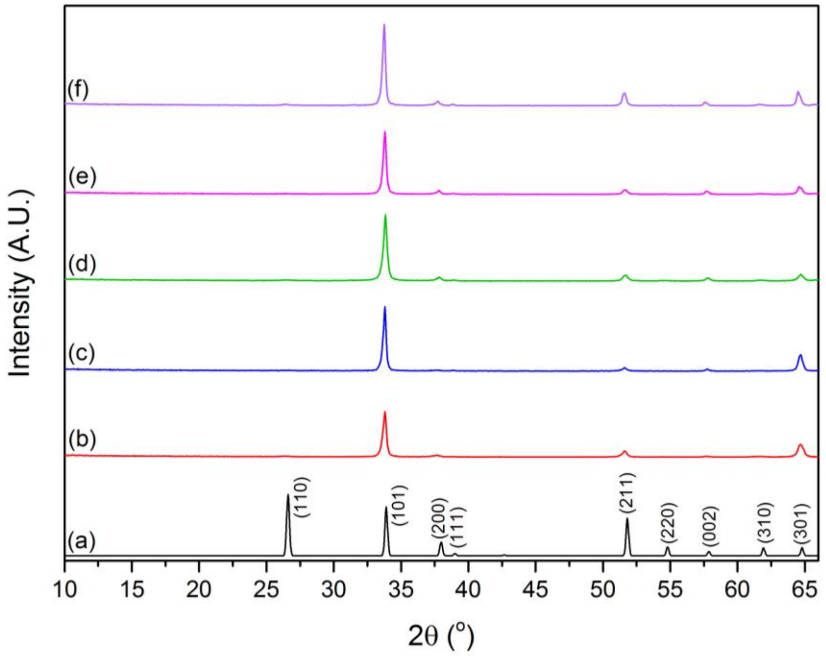

Fig. 5.2. XRD patterns of SnO_2 and ATO thin films deposited *via* single pot AACVD system at 450 °C. (a) standard SnO_2[166] (b) undoped SnO_2 (c) $Sn_{0.99}Sb_{0.01}O_2$ (d) $Sn_{0.96}Sb_{0.04}O_2$ (e) $Sn_{0.93}Sb_{0.07}O_2$ (f) $Sn_{0.90}Sb_{0.10}O_2$.

Table 5.2. Variation in the mean crystallite diameter and unit cell parameters of SnO_2 and ATO thin films with different dopant concentrations of $Sb(OEt)_3$.

Film	**Mean crystallite diameter /nm**	**a /Å**	**c /Å**	**Unit cell volume /Å^3**	**Volume contraction /%**
SnO_2	16	4.7670(5)	3.1902(2)	72.493(14)	
$Sn_{0.99}Sb_{0.01}O_2$	23	4.7687(8)	3.1945(2)	72.643(23)	0.20 (expansion)
$Sn_{0.96}Sb_{0.04}O_2$	19	4.7510(4)	3.1935(2)	72.081(11)	0.57
$Sn_{0.93}Sb_{0.07}O_2$	25	4.7510(4)	3.1915(2)	72.041(11)	0.62
$Sn_{0.90}Sb_{0.10}O_2$	23	4.7614(3)	3.1944(1)	72.421(8)	0.10

Texture coefficient calculations based on undoped SnO_2 were calculated for the doped ATO films (Fig. 5.3). All films, compared with a standard SnO_2,[166] showed no or minimal growth along the (110) and (220) planes, respectively. Undoped SnO_2 showed preference in growth along the (101) and (301) planes when compared to the SnO_2 standard pattern. The (101) plane was still preferred after doping but the (301) plane became less preferred. An increase in growth preference was seen along the (002) plane for the doped films. Despite there being a fair number of studies on ATO films, there is no consistency in the reported preferred orientation of growth of the films.[167, 168, 169, 170] Presumably, many factors such as the deposition technique, deposition conditions, precursors and the substrate used have an influence on the preferred orientation.[129]

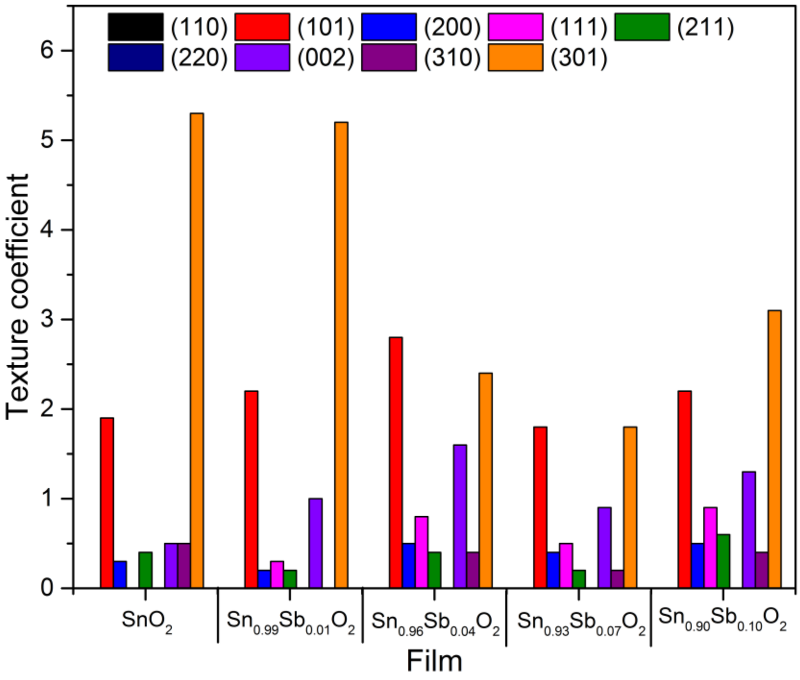

Fig. 5.3. Variation of the texture coefficient (Tc) of each plane with varying amounts of Sb dopant in SnO_2.

5.3.1.3 Surface morphology

The top-down surface morphology and side-on film thicknesses were analysed through a scanning electron microscope (Fig. 5.4). Regardless of film composition, the surface morphology of all the films was similar, which is in agreement with all films having a preference in growth along the (301) plane (Section 5.3.1.2). The morphology consisted of a heterogeneous distribution of clusters of irregular shaped particles delineated by defined boundaries. The clusters varied in size, ranging from 60-380 nm with no evidence of any amorphous features. Side-on images of the films revealed tooth-like features which were top heavy and increased in width with film thickness. Therefore, the only notable influence of Sb doping was a large increase in film thickness with dopant concentration (Table 5.4).

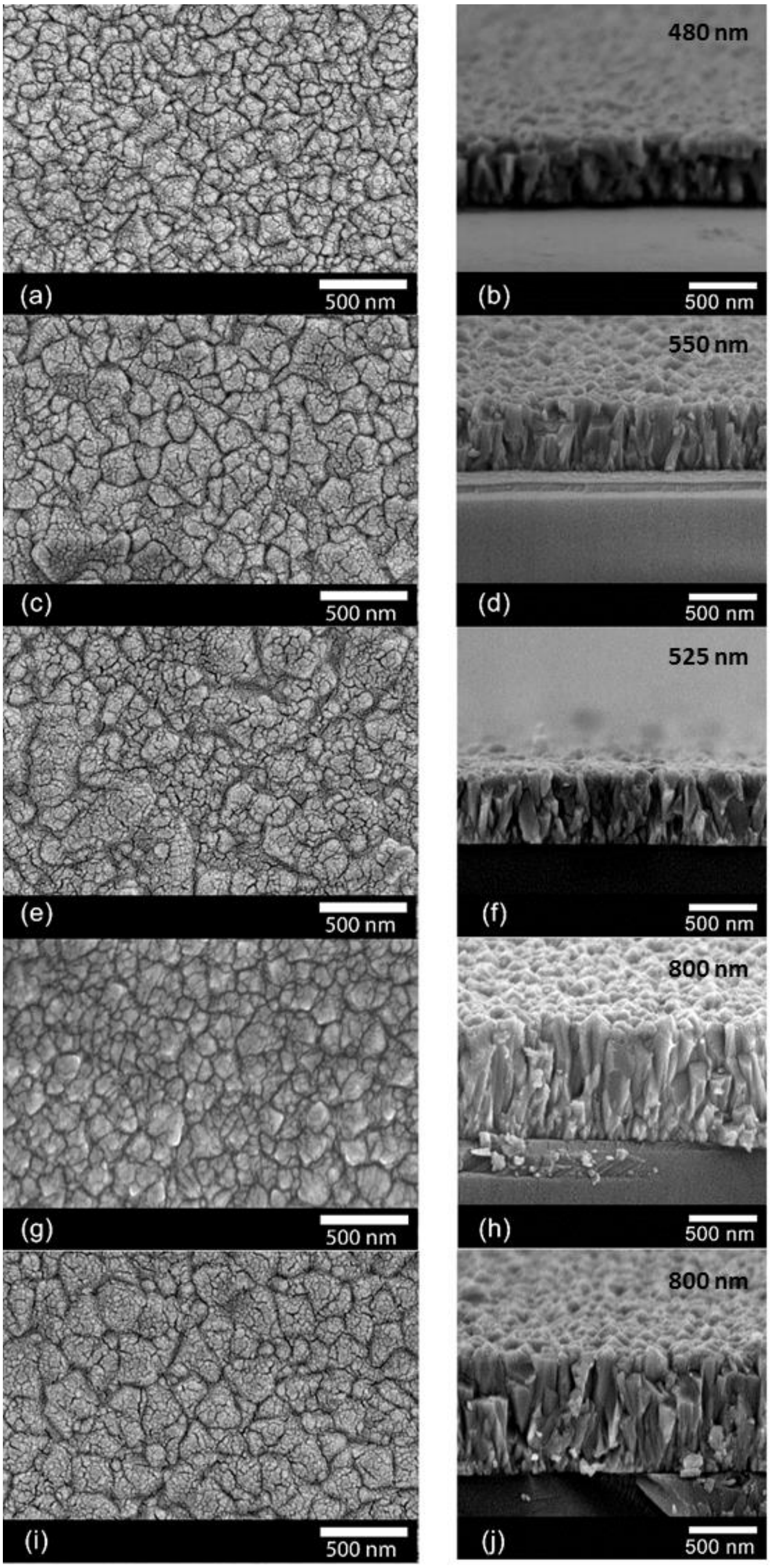

Fig. 5.4. Top down and side on SEM images of ATO thin films deposited *via* single pot AACVD at 450 °C. (a,b) undoped SnO_2 (c,d) $Sn_{0.99}Sb_{0.01}O_2$ (e,f) $Sn_{0.96}Sb_{0.04}O_2$ (g,h) $Sn_{0.93}Sb_{0.07}O_2$ (i,j) $Sn_{0.90}Sb_{0.10}O_2$.

5.3.1.4 Optical measurements

The optical characteristics were determined using UV/vis/IR spectroscopy (Fig. 5.6). The greatest transmittance observed in the visible was seen in the undoped SnO_2 film, a colourless transparent film, reaching a maximum of 85%. Upon doping with antimony, the films had a blue colouration but remained transparent. However, transparency in the visible reduced with increasing dopant concentration (Fig. 5.5 and Table 5.3). In contrast, the reflectance in the infrared more than doubled for the doped films compared with the undoped SnO_2, with $Sn_{0.99}Sb_{0.01}O_2$ reaching an approximate value of 70%. The intensity of the blue colouration increased with Sb dopant amounts which correlated with the expected reduction observed in the band gap (Table 5.3) which is also a feature commonly reported in literature regardless of deposition method.[156, 171, 172] There are many explanations that have been put forward for this observation, the main reason being that Sb^{5+} is responsible for the bluish colour due to absorbance of electrons in the conduction band of the semiconductor.[156, 157] In contrast, others suggest, based on the observed reduction in conductivity that the darkening must be due to the presence of an increase in Sb^{3+} ions concentration.[173] Naghavi *et al.* proposed that both ions, Sb^{5+} and Sb^{3+}, have a role in the darkening of the doped films by reducing the band gap – a consequence of impurity levels created above and below the conduction band.[174]

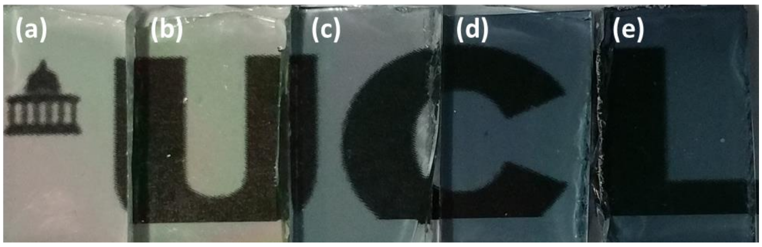

Fig. 5.5. Photograph showing the colour and transparency of the ATO films with increasing amount of dopant incorporation. (a) undoped SnO_2 (b) $Sn_{0.99}Sb_{0.01}O_2$ (c) $Sn_{0.96}Sb_{0.04}O_2$ (d) $Sn_{0.93}Sb_{0.07}O_2$ (e) $Sn_{0.90}Sb_{0.10}O_2$.

Table 5.3. Maximum transparency (%) across the visible (400-700 nm) and band gaps for ATO thin films. The band gaps were obtained from a Tauc plot[13] using optical measurement data (Fig 5.6).

Film	Transparency / %	Band gap / eV
SnO_2	85	3.6
$Sn_{0.99}Sb_{0.01}O_2$	80	3.5
$Sn_{0.96}Sb_{0.04}O_2$	65	3.5
$Sn_{0.93}Sb_{0.07}O_2$	50	3.5
$Sn_{0.90}Sb_{0.10}O_2$	45	3.4

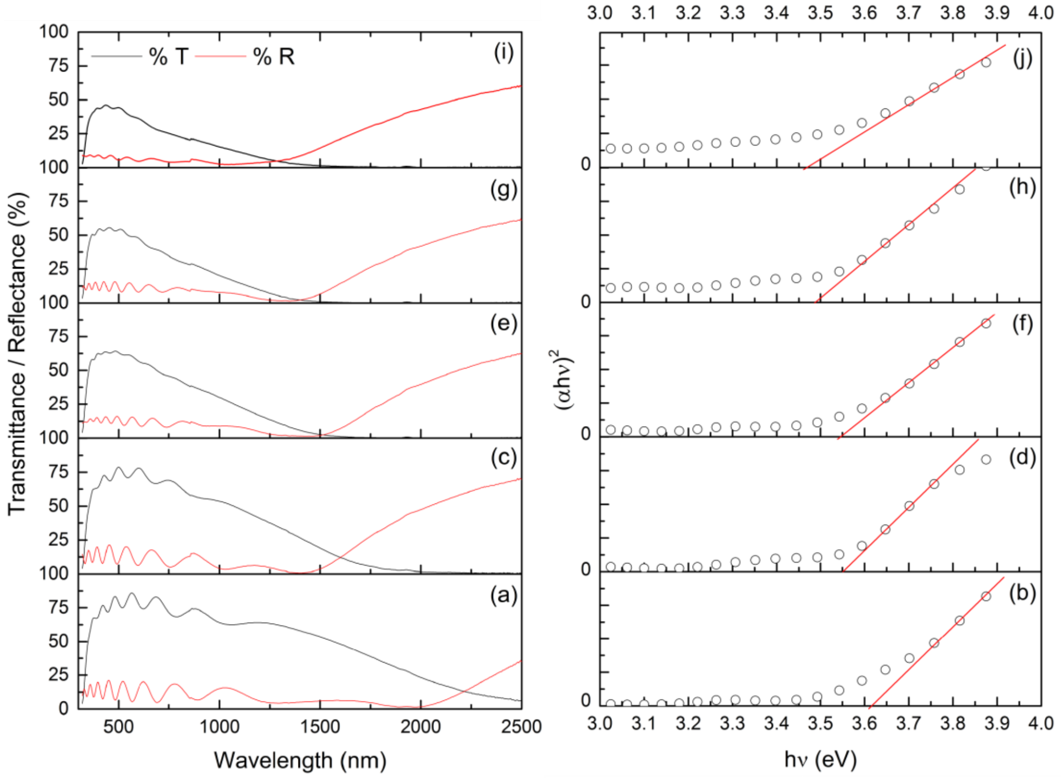

Fig. 5.6. Optical transmittance and reflectance spectra taken with an air background and Tauc plots for SnO_2 and ATO thin films deposited at 450 °C. (a,b) undoped SnO_2 (c,d) $Sn_{0.99}Sb_{0.01}O_2$ (e,f) $Sn_{0.96}Sb_{0.04}O_2$ (g,h) $Sn_{0.93}Sb_{0.07}O_2$ (i,j) $Sn_{0.90}Sb_{0.10}O_2$.

5.3.1.5 Electrical properties

All ATO films were identified by Hall effect measurements as n-type. Doping with antimony can dramatically reduce resistivity of the film compared with undoped SnO_2 (Table 5.4). In this instance, the trends in carrier concentration, mobility and resistivities do not conform to the norm. The greatest charge carrier concentration, 11.670×10^{20} cm^{-3}, was observed in the $Sn_{0.96}Sb_{0.04}O_2$ film but greater than 4 at.% Sb resulted in a reduction down to 5.764×10^{20} cm^{-3}. An explanation for this may be due to the Sn^{4+} vacancies that can occur at higher Sb dopant concentrations and act as charge neutralisation sites, reducing the carrier concentrations. This has been observed in Sb doped ZnO films previously.[175] The trend in mobility and conductivity (inverse of resistivity) mirrored that of charge carrier concentration an observation also seen in other systems including Mo doped In_2O_3.[150] However, this goes against the expected relationships between the three variables, where an increase in charge carrier concentration would lead to a reduction in mobility and in turn an increase in resistivity. It is important to state that there are two variables that need to be considered in this system: the at.% of Sb and the ratio of Sb^{5+}/Sb^{3+} present. It cannot be assumed that this ratio remains constant in each of these films since it is known that the ratio is dependent on the dopant level. Geraldo *et al.* reported that 85% of Sb at dopant levels of 4 at.% or less is in the +5 oxidation state but the composition changes at higher dopant levels.[176] The thickness of these films varied drastically but this was taken into consideration when calculating the sheet resistance. The best electrical conductivity was seen in the film with 4 at.% Sb, $Sn_{0.96}Sb_{0.04}O_2$, having a sheet resistance value of 9.0 Ω □$^{-1}$. On this basis, the deposition conditions used to deposit this film formed the starting point for the production of AFTO films.

Table 5.4. Hall effect measurements and film thicknesses of SnO_2 and ATO films. *d*, film thickness; *n*, charge carrier concentration; *μ*, charge carrier mobility; *ρ*, bulk resistivity; R_{sh}, sheet resistance.

Film	*d*/nm	*n*/ ×10^{20} cm^{-3}	*μ*/cm^2 V^{-1} s^{-1}	*ρ*/×10^{-3} Ω cm	R_{sh}/Ω □$^{-1}$
SnO_2	480	3.389	10.4	1.779	37.1
$Sn_{0.99}Sb_{0.01}O_2$	550	3.589	6.9	2.533	46.1
$Sn_{0.96}Sb_{0.04}O_2$	525	11.670	11.4	0.471	9.0
$Sn_{0.93}Sb_{0.07}O_2$	800	6.210	6.2	1.615	20.2
$Sn_{0.90}Sb_{0.10}O_2$	800	5.764	3.1	3.444	39.1

5.3.2 AACVD of AFTO films

Antimony and fluorine co-doped tin(IV) oxide thin films were deposited on SiO_2 barrier coated glass based on the optimum conditions found for the ATO system (10 mol.% antimony(III) ethoxide in a butyltin trichloride and methanol solution). Ammonium fluoride was added to the bubbler in 5, 10 and 20 mol.% amounts. Film deposition were carried out at 450 °C using air as the carrier gas.

5.3.2.1 Dopant quantities in the AFTO films

Co-doped films of AFTO were deposited using a single solution containing a mixture of 10 mol.% $Sb(OEt)_3$ in methanol with varying amounts of NH_4F. For reasons mentioned above (Sections 5.3.1.1 and 4.3.2.1) WDX was used to quantify Sb and F amounts in the films. (Table 5.5). In the single doped ATO film made using 10 mol.% antimony solution, WDX identified 4 at.% Sb in the bulk of the film. However, when co-doped with fluorine this was not reproducible and instead the three films made contained variable amounts of Sb. The present study, to my knowledge, is the only one that has varied the dopant amounts of fluorine whilst co-doping and hence it is not possible to compare the divergence of the mol.% of Sb in solution and the at.% found in the films. Therefore, it would be tenuous to suggest that the presence of fluorine is in some way affecting the Sb incorporation. WDX was also used to quantify the amounts of fluorine in the films and section 3.3.2 explains the low F dopant incorporation into the lattice compared with the mol.% amounts in the precursor solution. XPS was also used to determine the antimony concentration in the films by calculating the amount from 200 second etch time (Table 5.5). An analysis of XPS data from the surface of the films showed no detectable antimony.

Table 5.5. The relationship between mol.% in solution and at.% of antimony and fluorine in the films, deposited at 450 °C, determined by wavelength dispersive X-ray and X-ray photoelectron spectroscopy from 200 second etch time.

mol.% of Sb in solution	mol.% of F in solution	at.% of Sb determined by WDX	at.% of Sb determined by XPS	at.% of F determined by WDX
10	5	1	1	1
10	10	3	1	1
10	20	5	2	2

5.3.2.2 Crystal structure

Co-doping the films resulted in a greater disruption in the lattice structure compared with singly doped ATO, resulting in less crystalline XRD patterns (Fig. 5.7). Overall, the patterns matched that of cassiterite SnO_2. Furthermore, despite the number of atoms substituted into the lattice remaining the same for the $Sn_{0.96}Sb_{0.04}O_2$ and $Sn_{0.96}Sb_{0.03}F_{0.01}O_2$, the XRD pattern was more disrupted for the latter film. This discrepancy could be due to the influence of the +5 oxidation state of antimony on the fluoride ion which would not have been the case when fluorine had been co-doped with Al or Ga, which only exist in the +3 state. The mean crystallite diameters (Table 5.6) markedly decreased with increasing number of dopant atoms incorporating into the film lattice which correlated with a decrease in crystallinity as shown by XRD. The unit cells of the films, calculated as before, showed a contraction (Table 5.6). This suggests that more of the smaller Sb^{5+} is substituting the Sn^{4+} ion. However, it is still possible that a mixture of Sb^{5+}/Sb^{3+} is being incorporated when more than 1 at.% Sb is present because the relative difference in ionic sizes of Sn^{4+} to Sb^{5+} and Sn^{4+} to Sb^{3+} will overall still give a contraction unless the majority of the replaced ions are Sb^{3+}. Furthermore, any amount of fluorine introduced into the lattice will result in a contraction because of its smaller radius compared with the substituted oxide ion.

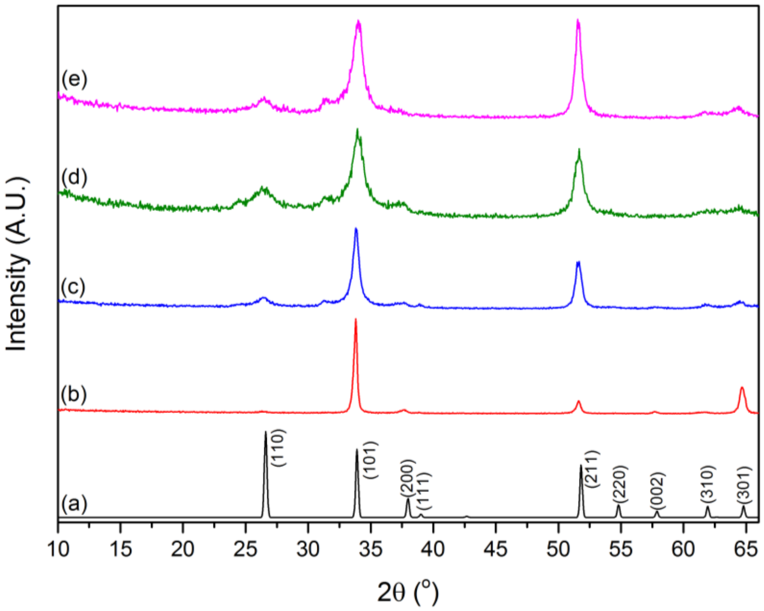

Fig. 5.7. XRD patterns of SnO_2 and AFTO thin films deposited *via* single pot AACVD system at 450 °C. (a) standard SnO_2[166] (b) undoped SnO_2 (c) $Sn_{0.98}Sb_{0.01}F_{0.01}O_2$ (d) $Sn_{0.96}Sb_{0.03}F_{0.01}O_2$ (e) $Sn_{0.93}Sb_{0.05}F_{0.02}O_2$.

Table 5.6. Variation in the mean crystallite diameter and unit cell parameters of SnO_2 and AFTO thin films with different dopant concentrations of $Sb(OEt)_3$ and NH_4F.

Film	Mean crystallite diameter /nm	a /Å	c /Å	Unit cell volume /Å³	Volume contraction /%
SnO_2	16	4.7670(5)	3.1902(2)	72.493(14)	
$Sn_{0.98}Sb_{0.01}F_{0.01}O_2$	11	4.7605(10)	3.1900(7)	72.292(24)	0.27
$Sn_{0.96}Sb_{0.03}F_{0.01}O_2$	6	4.7648(22)	3.1709(18)	71.990(51)	0.68
$Sn_{0.93}Sb_{0.05}F_{0.02}O_2$	8	4.7755(19)	3.1660(15)	72.201(41)	0.61

Fig. 5.8 shows the preference in plane growth of the co-doped films. In the undoped SnO_2 and AFTO films there was no growth in the (111) and (220) planes, whereas whilst present in SnO_2 no growth was also seen along the (200) and (002) planes in the co-doped films. Furthermore, growth along the (110) plane was only present in the AFTO films. Lastly, apart from $Sn_{0.98}Sb_{0.01}F_{0.01}O_2$, the other co-doped films, containing greater amounts of antimony, growth along the (310) plane was absent. Compared with ATO films, co-doping has a more profound effect on the preferential growth of the films, namely more of the planes are absent.

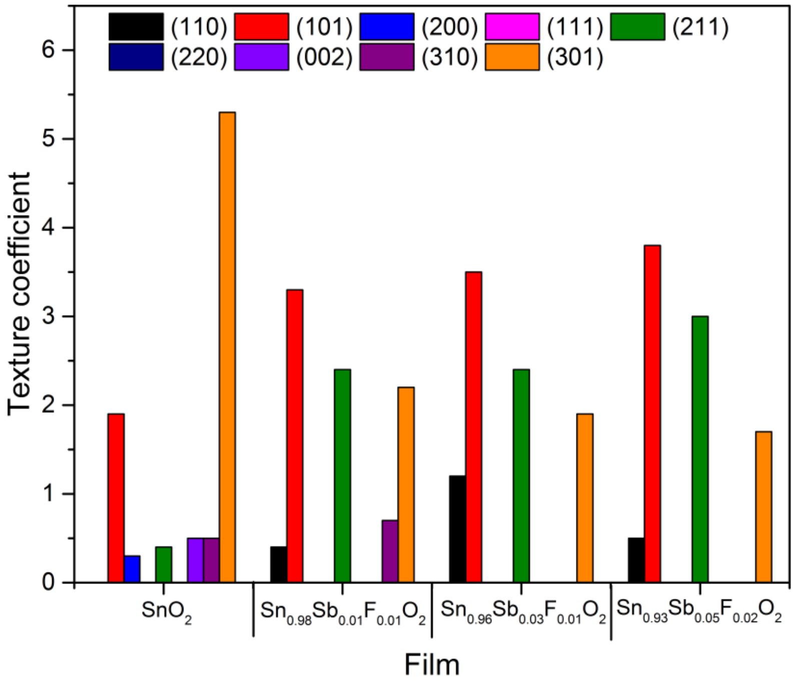

Fig. 5.8. Variation of the texture coefficient (Tc) of each plane with varying amounts of Sb and F dopants in SnO_2.

5.3.2.3 Surface morphology

When compared with undoped SnO_2 and ATO films, the morphologies of the co-doped films markedly changed (Fig. 5.9). The AFTO films appeared more uniform, with regards to particle shape and size, with increasing amounts of antimony incorporation into the SnO_2 lattice. The $Sn_{0.98}Sb_{0.01}F_{0.01}O_2$ film surface morphology showed a diverse range of particles that appear more protruding like hence giving film an uneven surface. This is further supported by the mountainous appearance seen in the side-on SEM image (Fig. 5.9c and d). As the antimony dopant increased (and fluorine dopant remaining the same) there was a noticeable absence of the larger particles and hence fewer protrusions which is supported by the image seen in Fig. 5.9f. AFTO films made by ultrasonic spray pyrolysis also showed a reduction in particle size with increasing Sb dopant concentration.[161] The morphology of the $Sn_{0.93}Sb_{0.05}F_{0.02}O_2$ film showed a greater consistency in particle shape and size, with most of the particles having a rice grain appearance and measuring at an average of 360 nm in length (Fig. 5.9g). Co-doping with Sb and F resulted in thick films even at lower concentrations (Table 5.8).

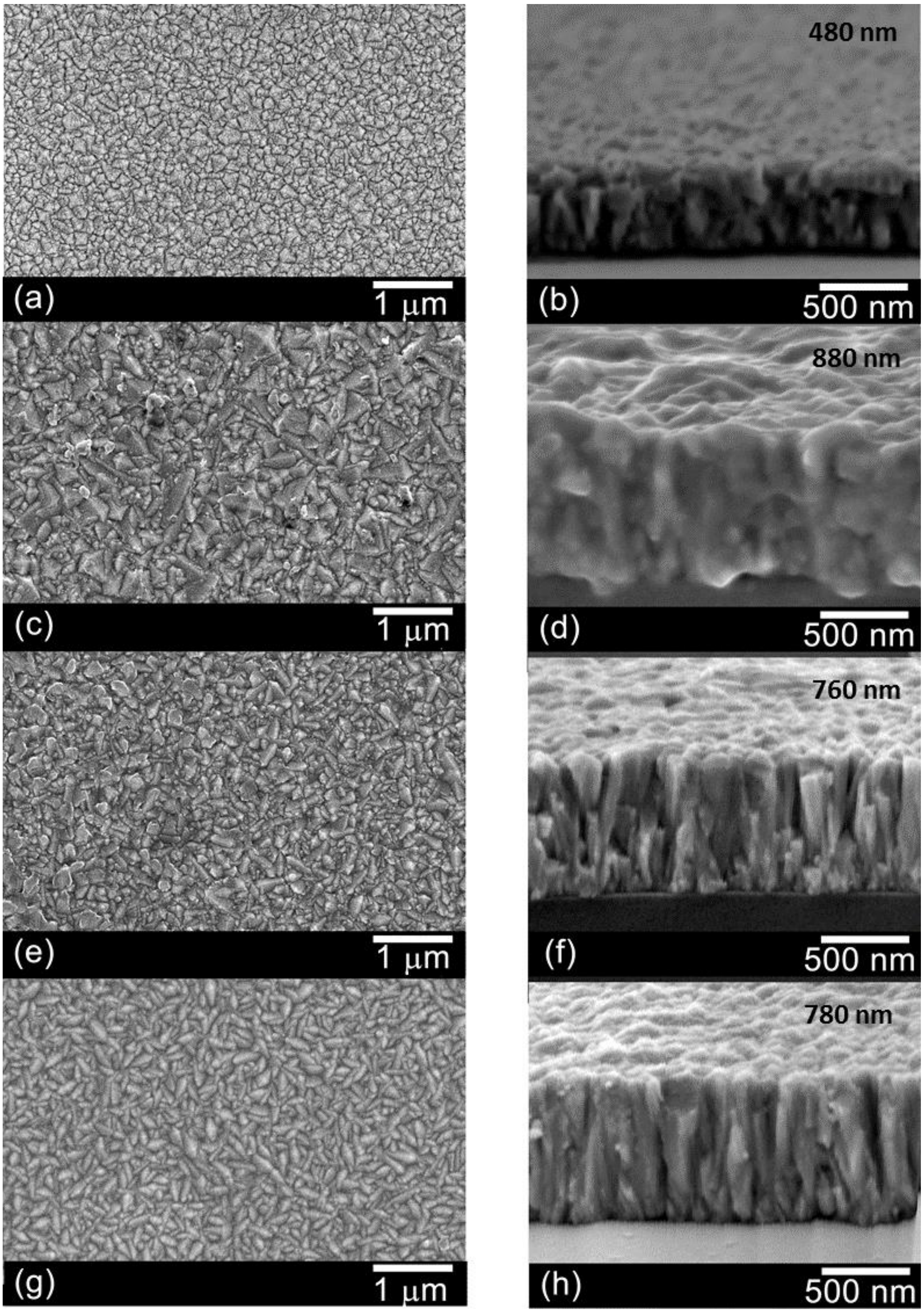

Fig. 5.9. Top down and side on SEM images of AFTO thin films deposited *via* single pot AACVD at 450 ^{0}C. (a,b) undoped SnO$_2$ (c,d) Sn$_{0.98}$Sb$_{0.01}$F$_{0.01}$O$_2$ (e,f) Sn$_{0.96}$Sb$_{0.03}$F$_{0.01}$O$_2$ (g,h) Sn$_{0.93}$Sb$_{0.05}$F$_{0.02}$O$_2$.

5.3.2.4 Optical measurements

Optical measurements, taken using UV/vis/IR spectroscopy, showed the percentage transparency in the visible to reduce by more than half compared with undoped SnO_2 (Fig. 5.10) and lower than that of the highest Sb at.% single doped film. The AFTO films were transparent and near-black in colour with transmittance remaining very similar regardless of atomic composition of the films, reaching a maximum of 40%. The reduction in transparency and the blackening of AFTO films has been reported by others.[161] Kojima *et al.* states that the blackening of the films is attributed to the coexistence of the two different oxidation states of the Sb ion, 5+ and 3+.[173] The reflectance properties of the films was greater but variable than undoped SnO_2, however there was no obvious trend to report. Furthermore, as expected, the band gaps of these films decreased compared with SnO_2 (Table 5.7).

Table 5.7. Maximum transparency (%) across the visible (400-700 nm) and band gaps for AFTO thin films. The band gaps were obtained from a Tauc plot[13] using optical measurement data (Fig. 5.10).

Film	Transparency / %	Band gap / eV
SnO_2	85	3.6
$Sn_{0.98}Sb_{0.01}F_{0.01}O_2$	36	3.3
$Sn_{0.96}Sb_{0.03}F_{0.01}O_2$	35	3.2
$Sn_{0.93}Sb_{0.05}F_{0.02}O_2$	40	3.4

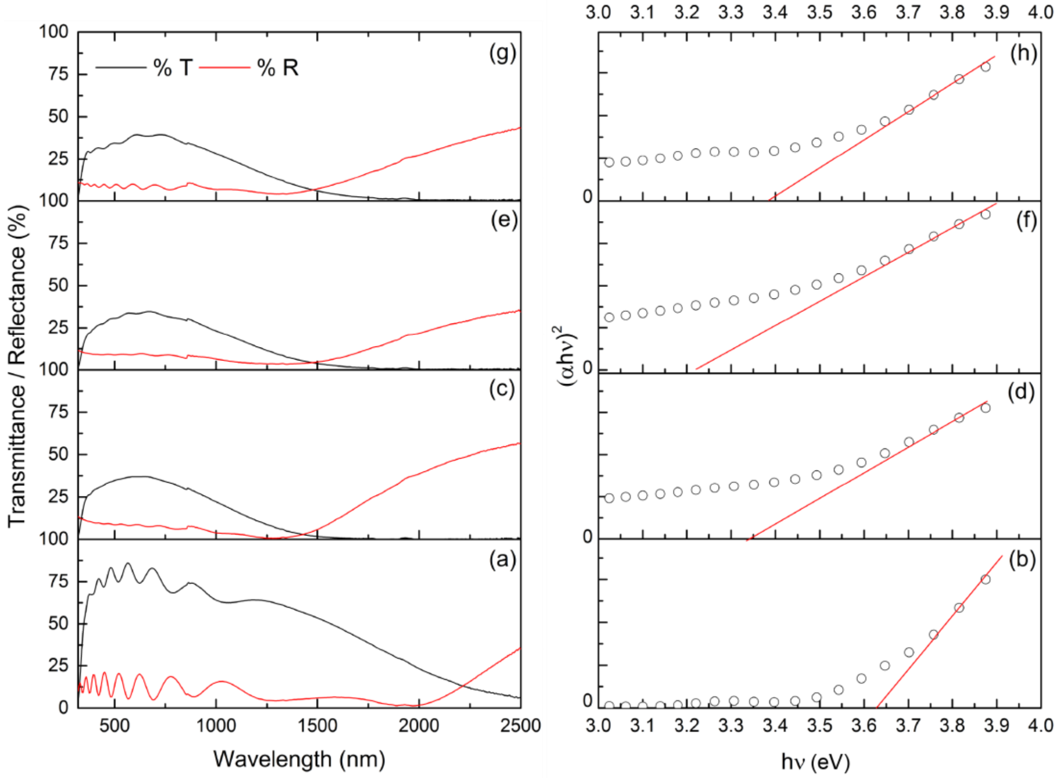

Fig. 5.10. Optical transmittance and reflectance spectra taken with an air background and the Tauc plots for SnO_2 and AFTO thin films deposited at 450 °C. (a,b) undoped SnO_2 (c,d) $Sn_{0.98}Sb_{0.01}F_{0.01}O_2$ (e,f) $Sn_{0.96}Sb_{0.03}F_{0.01}O_2$ (g,h) $Sn_{0.93}Sb_{0.05}F_{0.02}O_2$.

5.3.2.5 Electrical properties

n-type AFTO films showed lower sheet resistances compared with undoped SnO_2 (Table 5.8). Unexpectedly, co-doping the ATO films with fluorine did not further enhance electrical properties particularly since FTO is a widely used commercial TCO with excellent optoelectronic properties where electrical resistivities as low as 7 Ω □$^{-1}$ (TEC 7). The sheet resistance was found to be lowest for $Sn_{0.98}Sb_{0.01}F_{0.01}O_2$ with a value of 19.4 Ω □$^{-1}$. However, this was no better than the lowest value obtained from single doped ATO films, an observation reported by others who found that single doped ATO and FTO are superior than the combination of both dopants in one film.[161] The mobility of the films continues to remain low with values similar to those of $Sn_{0.90}Sb_{0.10}O_2$ film, however this is not entirely unexpected since the charge carrier concentration was greater for the AFTO films than the undoped SnO_2 film. Except for $Sn_{0.96}Sb_{0.03}F_{0.01}O_2$, which had a greater resistivity, the values for the other films were similar to SnO_2.

Table 5.8. Hall effect measurements and film thicknesses of SnO_2 and AFTO films. *d*, film thickness; *n*, charge carrier concentration; *μ*, charge carrier mobility; *ρ*, bulk resistivity; R_{sh}, sheet resistance.

Film	*d*/nm	*n*/ ×10^{20} cm^{-3}	*μ*/cm^2 V^{-1} s^{-1}	*ρ*/×10^{-3} Ω cm	R_{sh}/Ω □$^{-1}$
SnO_2	480	3.389	10.4	1.779	37.1
$Sn_{0.98}Sb_{0.01}F_{0.01}O_2$	880	8.483	4.3	1.708	19.4
$Sn_{0.96}Sb_{0.03}F_{0.01}O_2$	760	7.458	3.4	2.473	32.5
$Sn_{0.93}Sb_{0.05}F_{0.02}O_2$	780	7.095	5.1	1.724	34.8

5.4 Conclusions

Single doped ATO and co-doped AFTO films were successfully deposited using a simple single pot aerosol assisted chemical vapour deposition (AACVD) technique. The chemicals used (butyltin trichloride, antimony(III) ethoxide and ammonium fluoride) were cost effective and safe to handle. Antimony(III) ethoxide as well as the delivery method facilitated by AACVD, proved to be an effective doping system. This system produced coloured glass with good transparency, namely blue and black where the intensity of the colour can be altered by changing the dopant concentrations that are incorporated into the SnO_2 lattice. Coloured glass has an obvious application in architectural features, which combined with its electrical properties can lead them to use in a wider range of applications. The ATO films were all polycrystalline but unlike SnO_2, showed no growth in the (110) and (220) planes. The morphologies of these films were similar regardless of film composition and the films got thicker with increasing dopant amounts. The single doped films were blue and got darker (reduced transmittance in the visible) with increasing dopant incorporation and hence a reduction in the band gap was seen. The lowest sheet resistance of 9.0 $\Omega\ \square^{-1}$ was achieved with the $Sn_{0.96}Sb_{0.04}O_2$ film. Adding a second dopant into the precursor solution did not produce the consistency expected between the concentration of dopant in the solution and the amount incorporated in the film. The SnO_2 lattice of the AFTO films was disrupted resulting in a less crystalline lattice as well as the absence of growth along the (111) and (220) planes. A change in morphology was seen compared with the single doped films where the distribution of particles appeared more uniform. The AFTO films were black, with a maximum transmittance of 40% and a further reduction in the band gap was measured. The lowest sheet resistance measured for these films was 19.4 $\Omega\ \square^{-1}$ for the $Sn_{0.98}Sb_{0.01}F_{0.01}O_2$ film. Surprisingly, the film with the best optoelectronic properties in the realm of TCO's was the single doped film, $Sn_{0.96}Sb_{0.04}O_2$ rather than a film containing fluorine as the second dopant particularly as FTO is a widely known commercial TCO. The lack of similar studies makes it difficult to explain our unexpected results. However, it is worth noting that it is possible that the best AFTO film is yet to be made and these co-doped films may not be comparable to each other as the composition of the two oxidation states of the antimony ions present is unknown in the films reported in this chapter.

Chapter 6 will extend the present study by investigating doping the SnO_2 lattice with tungsten alone and as a co-dopant with fluorine. Tungsten is a promising dopant because in its favourable +6 oxidation state each ion can donate two electrons into the conduction band when substituted for tin. Hence, the carrier concentration can be significantly enhanced without the need for high dopant incorporation.

6

Tungsten doped and tungsten-fluorine co-doped tin(IV) oxide thin films

Chapter 6 explores the optoelectronic characteristics of tungsten doped tin(IV) oxide (WTO) and tungsten-fluorine co-doped tin(IV) oxide (WFTO) deposited *via* aerosol assisted CVD (AACVD). The co-doped films were based on the conditions employed to produce the optimum WTO film. These films were compared with the properties of commercially available FTO.

6.1 Introduction

In Chapter 5, antimony was successfully doped into SnO_2 improving its conductivity and producing a coloured film with applications in architectural glass coatings. The maximum oxidation state exhibited by antimony is +5 and its smaller ionic radius makes it an ideal dopant for n-type conductivity. It would be desirable to produce a thin film based on SnO_2 with comparable electrical properties with that of the best ATO film but with higher optical transparency, meeting the requirement of >80%.

Like antimony, tungsten can also exist in various oxidation states with W^{6+} being the most common and having an ionic radius of 0.60 Å which makes tungsten a promising dopant for replacing the slightly larger Sn^{4+} ion (0.69 Å) in the SnO_2 lattice. Tungsten has been shown to be a good dopant for producing TCOs based on In_2O_3 and TiO_2.[177, 178] The relative expense and scarcity of indium inhibits its long-term use which means alternatives such as SnO_2 need to be investigated (see Section 1.5). There have been a handful of studies producing and characterising tungsten doped tin(IV) oxide (WTO) thin films employing a variety of deposition methods including sputtering, sol-gel, chemical bath, pulsed plasma, chemical vapour deposition and spray pyrolysis.[64, 178, 179, 180, 181] Most of these studies produced their best films using low dopant amounts of tungsten, with the lowest reported resistivity of 6.67×10^{-4} Ω cm, better than undoped SnO_2 thin films.[182] The low dopant amount in the films still gave rise to relatively high conductivities since there is a valence difference of two between the Sn^{4+} and W^{6+} ions. This difference is larger than common doped films like AZO and ATO where the charge carrier concentration is lower for dopant amounts equal to that of tungsten.[182, 183]

The following chapter investigates the use of aerosol assisted chemical vapour deposition (AACVD) of tungsten doped and, tungsten and fluorine co-doped tin(IV) oxide thin films. Comparing existing studies on WTO films it is apparent that deposition methods greatly influences the optoelectronic properties of the films. For example, studies by Huang *et al.* using the two different techniques, pulsed plasma and sol-gel dip coating, reported values for resistivity, mobility and charge carrier concentration for their best WTO films. The latter deposition method produced an inferior film with a resistivity and charge carrier concentration 10-fold lower as well as a 75% reduction in mobility.[182, 183] The present study, to my knowledge, is the first to deposit WTO films using AACVD, a simple cost-effective technique in which film properties can be controlled and optimised. Based on the conditions required for the optimum WTO film, co-doping with W and F into a SnO_2 unit cell will be investigated. Fluorine doped SnO_2 is an established commercial coating since the incorporation of fluorine into the lattice increases the number of free electrons by substituting O^{2-} for F^{-}. Thus far only one study, published in 2014, that I am aware of, has co-doped tungsten and fluorine into tin(IV) oxide (WFTO) *via* a spray pyrolysis method and found resistivity was lower than that of commercial fluorine doped tin(IV) oxide (FTO).[184] As reported in Chapter 5, co-doping fluorine alongside antimony into SnO_2 did not improve the optoelectronic properties of the resultant films compared with the singly doped ATO films. Therefore, it would be worthwhile to investigate if this is still the case with WFTO films deposited *via* AACVD.

6.2 Experimental

The films discussed in this chapter were deposited using a simple single pot AACVD set-up (Fig. 1.18) in a fume hood. An undoped tin(IV) oxide film was made from the glass bubbler containing 0.30 g butyltin trichloride in 20 mL methanol (Scheme 11). WTO films were produced by adding the desired dopant amounts of tungsten(VI) hexacarbonyl to the bubbler (Scheme 12). WFTO films required the addition of tungsten(VI) hexacarbonyl as well as ammonium fluoride precursor, in varying mol.% amounts, into the bubbler (Scheme 13). Before each deposition, the solution in the bubbler was sonicated for 10 minutes. The precursors were all purchased from Sigma Aldrich. The solvents were purchased from Fischer Scientific. All the films were produced at 450 °C in air at a flow rate of 1.5 L min^{-1} (≥99.9% supplied by BOC). A humidifier was used to turn the solution into an aerosol which was transported in the carrier gas into the deposition chamber, lasting approximately 20-30 minutes by which time all the solution had been depleted. All the films, WTO and WFTO, were adherent with full coverage of the substrate and were colourless.

$$\mathrm{BuSnCl_3} \xrightarrow[\text{450 °C; Air}]{\text{MeOH}} \mathrm{SnO_2} + \text{waste} \qquad \text{(Scheme 11)}$$

$$\mathrm{BuSnCl_3} + \mathrm{W(CO)_6} \xrightarrow[\text{450 °C; Air}]{\text{MeOH}} \text{WTO} + \text{waste} \qquad \text{(Scheme 12)}$$

$$\mathrm{BuSnCl_3} + \mathrm{W(CO)_6} + \mathrm{NH_4F} \xrightarrow[\text{450 °C; Air}]{\text{MeOH}} \text{WFTO} + \text{waste} \qquad \text{(Scheme 13)}$$

Other precursors for the dopant that were explored include tungsten(VI) ethoxide and ammonium tungstate. However, these either did not produce films with identifiable quantities of the dopant or had conductivities too low for consideration.

The films discussed in the following chapter will be referred to as the amount of dopant(s) found in the bulk of the film rather than the amount present in the precursor solution.

6.2.1 Instrumental conditions

EDX and WDX calculations were carried out using the JEOL JSM-6301F field emission and Phillips ESEM, respectively. The Sn, W and F at.% was obtained from the Sn-L_α line (3444 eV), W-L_α (8398 eV) and F-K_α (676.8 eV) X-ray emission lines, respectively.

6.3 Results and discussion

6.3.1 AACVD of WTO films

Tungsten doped tin(IV) oxide thin films were deposited on SiO_2 barrier coated glass by adding varying mol.% amounts (0.1, 0.2, 0.5, 0.7 and 1%) of tungsten(VI) hexacarbonyl, $W(CO)_6$, into a butyltin trichloride and methanol solution. Depositions were carried out in air and at 450 °C. The film deposited using 0.1 mol.% $W(CO)_6$ in solution was found not to have detectable levels of tungsten and hence the outcome of further analysis will not be discussed. However, it is worth noting that the electrical conductivity of this film (25.4 $\Omega\ \square^{-1}$) was better than undoped SnO_2.

Another noteworthy observation, made in a preliminary investigation, was that when using a reduced flow rate of 1.0 L min^{-1} of air resulted in films consisting of two regions. The inlet side of the film was yellow and transparent and the outlet end of the film was colourless. XPS showed that the yellow films contained a greater amount of tungsten corresponding to W^{6+}. In addition, the conductivity of the yellow regions was substantially inferior, reaching kΩ values using the 2-point probe. This is a characteristic of over doping films which commonly results in a deterioration in the film structure.[108] To achieve a consistent film to allow a reliable analysis, the effect of varying the carrier gas flow rate was investigated. Visibly uniform films were achieved with a flow rate of 1.5 L min^{-1}.

6.3.1.1 Dopant quantities of the WTO films

Energy dispersive X-ray spectroscopy was used to determine the at.% of tungsten incorporated into the films. Dopant amounts in solution used in this system has been considerably lower than mol.% previously used in the other systems investigated (Chapters 3-5) to give similar at.% amounts in the films. For example, a 5 mol.% solution of antimony(III) ethoxide resulted in 1 at.% Sb in the ATO film. In contrast, to achieve the same at.% of W in WTO film, a much lower mol.% solution of tungsten(VI) hexacarbonyl was required (Table 6.1). X-ray photoelectron spectroscopy analysed the oxidation state at the surface and elemental composition of the films at 400 seconds etch time. There was a positive correlation, confirmed by EDX and XPS, between the mol.% of the tungsten dopant in solution and the at.% of tungsten found in the films. The discrepancy in the at.% values given by the two methods is attributed to the nature by which each film is analysed (Section 4.3.1.1). The oxidation state can only be calculated from data at the surface as etching the films leads to a reduction in the elements state due to preferential etching of oxygen over metals. The oxidation state of tin was confirmed to be Sn^{4+} with the Sn $3d_{5/2}$ and Sn $3d_{3/2}$ peak centred at 486.1 eV and 494.4 eV, respectively, for all films (Fig. 6.1a). The O 1s peak had a binding energy value between 529.8-530.4 eV. The film with the lowest amount of tungsten in solution showed no tungsten at the surface. A small amount of tungsten was detected at the surface for the films deposited using 0.5 mol.% and 0.7 mol.% $W(CO)_6$, which was too low to allow accurate modelling of the proportion of each oxidation state. A study by Yang *et al.* found no W 4f peaks below 2 at.% in the film.[185] The film with the highest dopant amount, 1 mol.% in solution, showed tungsten in the +4 and +6 oxidation states with the $4f_{7/2}$ peak having binding energies of 34.3 and 35.8 eV, respectively (Table 6.1 and Fig. 6.1b). It has been reported that doping beyond 2 at.% W leads to some of the W^{6+} being reduced to lower valence states.[184]

Table 6.1. The relationship between mol.% in solution and at.% of tungsten in the films, deposited at 450 °C, determined by energy dispersive X-ray and X-ray photoelectron spectroscopy at 400 seconds etch time and at the surface for the varying oxidation states.

mol.% in solution	at.% determined by EDX	at.% determined by XPS	at.% determined by XPS at the surface	
0.2	1	0.2		
0.5	1.5	0.6	+4	+6
0.7	2	0.8		
1.0	3	3.1	0.5	3.7

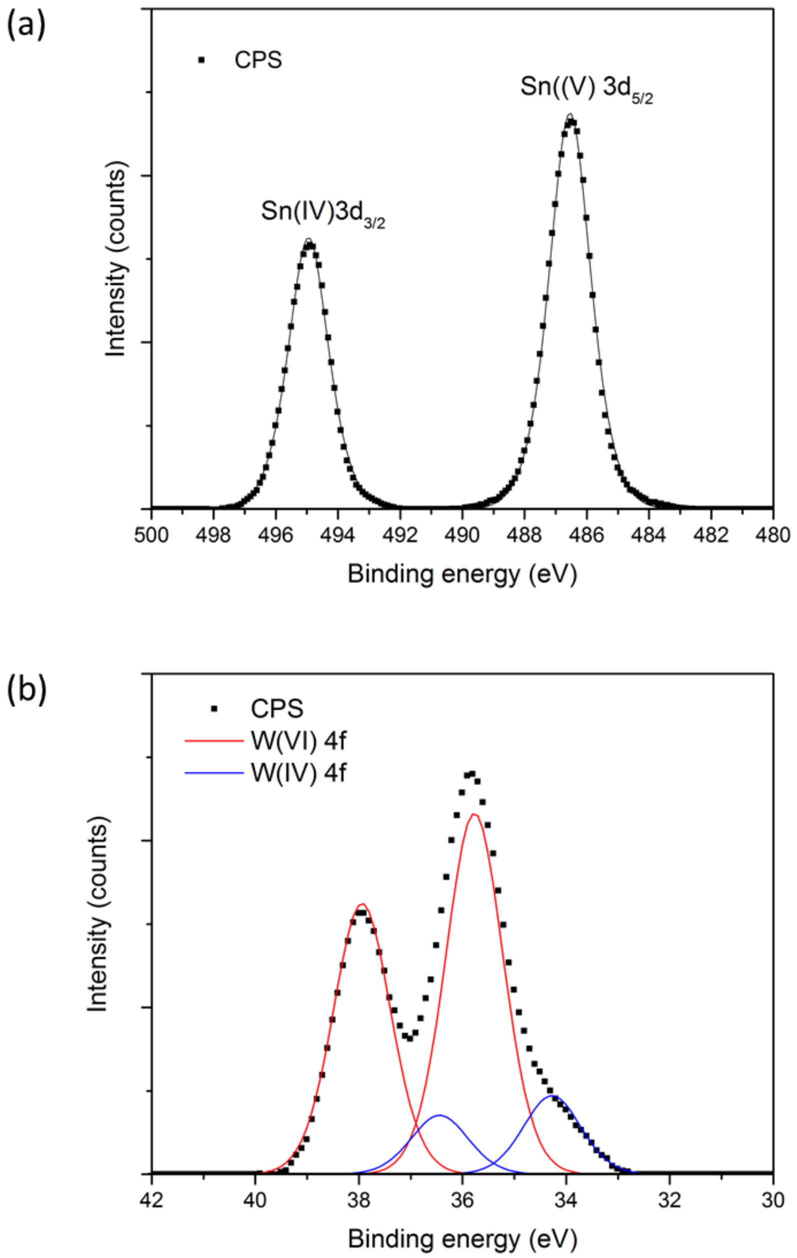

Fig. 6.1. Representative XPS spectra of (a) Sn $3d_{5/2}$ and $3d_{3/2}$ peaks and (b) W $4f_{7/2}$ and $4f_{5/2}$ peaks showing the two different oxidation state peaks.

6.3.1.2 Crystal structure

The crystal structure of the films was determined *via* data collected using X-ray diffraction (Fig. 6.2). As previously found in Chapter 5, the XRD patterns of all films were polycrystalline and matched that of tetragonal rutile SnO_2. The crystallinity of the films remained unaltered regardless of film composition, a finding reported by others.[182] This could be attributed to the relatively small amount of tungsten incorporated into the SnO_2 lattice. The mean crystallite size from the WTO films was equal to or greater than that of undoped SnO_2 however the relatively large variation observed in calculating each mean crystallite diameter negates the apparent differences recorded in Table 6.2. The percentage unit cell contraction was calculated from the XRD data fitted using the Le Bail method. As expected, the percentage contraction increased with dopant concentrations incorporated into the film since the ionic radius of W^{6+}(0.60 Å) is smaller than the substituted ion, Sn^{4+} (0.69 Å). The small differences in percentage contraction maybe due to the presence of both oxidation states, +4 and +6, as found with the 3 at.% WTO film. Furthermore, it should be noted that the error calculated for the contraction observed in the SnO_2 unit cell is relatively large hence having an effect on the values obtained for the unit cell size of the crystal structure of the doped films.

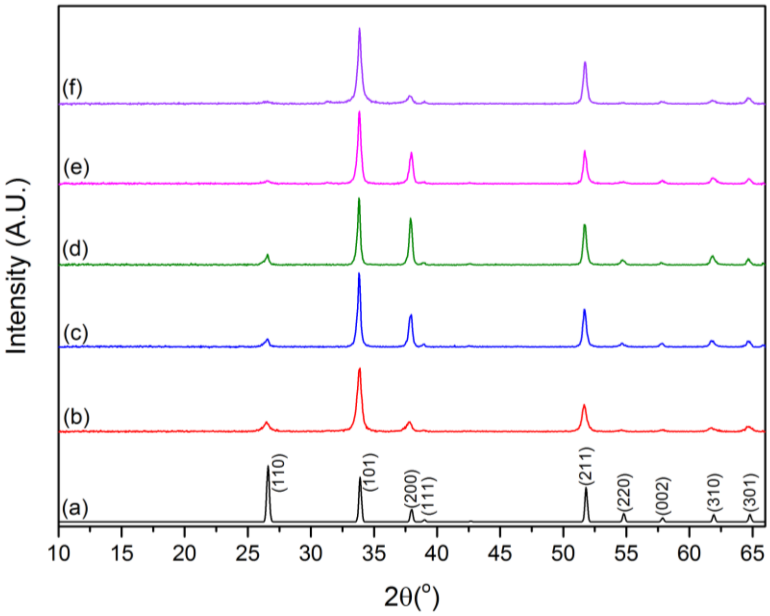

Fig. 6.2. XRD patterns of SnO_2 and WTO thin films deposited *via* single pot AACVD system at 450 °C. (a) standard SnO_2[166] (b) undoped SnO_2 (c) $Sn_{0.99}W_{0.01}O_2$ (d) $Sn_{0.985}W_{0.015}O_2$ (e) $Sn_{0.98}W_{0.02}O_2$ (f) $Sn_{0.97}W_{0.03}O_2$.

Table 6.2. Variation in the mean crystallite diameter and unit cell parameters of SnO_2 and WTO thin films with different dopant concentrations of $W(CO)_6$.

Film	Mean crystallite diameter /nm	a /Å	c /Å	Unit cell volume /Å^3	Volume contraction /%
SnO_2	18	4.7594(12)	3.1891(7)	72.239(31)	
$Sn_{0.99}W_{0.01}O_2$	25	4.7493(3)	3.1928(3)	72.018(9)	0.31
$Sn_{0.985}W_{0.015}O_2$	26	4.7464(2)	3.1960(3)	72.001(7)	0.33
$Sn_{0.98}W_{0.02}O_2$	21	4.7446(5)	3.1960(5)	71.947(11)	0.40
$Sn_{0.97}W_{0.03}O_2$	18	4.7494(4)	3.1892(3)	71.937(11)	0.42

The preferred plane growth of the WTO films was compared with undoped SnO_2 which has growth preference in the (101), (200), (211), (310) and (301) planes. The intensity of the (101) plane was almost double that of the other preferred planes. Interestingly, when the films were doped the (101) plane as well as the (301) plane weakened. The intensity of the (211) and (310) planes were similar to undoped SnO_2. However, the intensity of the (200) plane increases when doped, doubling with 1.5 at.% tungsten before steadily declining to a value half that of undoped SnO_2 at the highest dopant amount, 3 at.%. The preferred orientations of the tetragonal rutile tin(IV) oxide varies from study to study, highlighting the significance of the deposition method employed effecting the growth of the films.[64, 182, 186] Of these studies, Kumar *et al.* also reported that the (200) plane increases "remarkably" with tungsten doping.[186] Preferential growth has an impact on the physical properties of the films, for example the (200) plane in SnO_2 has been reported to influence the electrical mobility.[187]

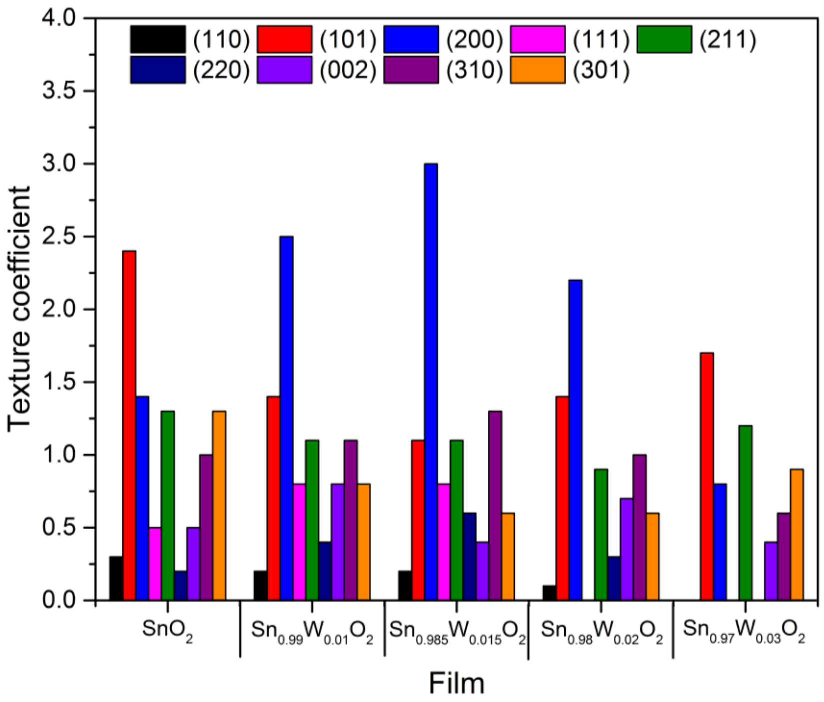

Fig. 6.3. Variation of the texture coefficient (Tc) of each plane with varying amounts of W dopant in SnO_2.

6.3.1.3 Surface morphology

The morphology of these films was observed top-down and side-on through a scanning electron microscope (Fig. 6.4). Undoped SnO_2 was deposited at a flow rate of 1.5 L min^{-1} instead of 1.0 L min^{-1} as used in Chapter 5. This variable alone seems to have influenced film morphology. At the greater flow rate, the range of particle sizes was narrower (from 50-260 nm) and the shape, while irregular, was more defined. In general, doping caused the particle size range to increase. The film with 1 at.% W incorporated into the SnO_2 lattice, there was a noticeable increase in the amount of larger particles in the size range of 300-360 nm (Fig 6.4c). As the atomic percentage of W increased to 1.5, the absence of smaller particles was more notable as well as the upper particle size limit reaching approximately 420 nm (Fig 6.4e). At 2 at.%, the modal particle size reduced to values between 200-300 nm (Fig 6.4g). In the film with the highest W dopant amounts the particles coalesced more making particle separation less obvious (Fig 6.4i). The observed decrease in particle size beyond 1.5 at.% tungsten could be a result of a limitation in grain growth attributed to a disruption in the lattice with increasing amounts of W atoms.[181] Side-on images show consistency in thickness of the SnO_2 and WTO films (Table 6.3).

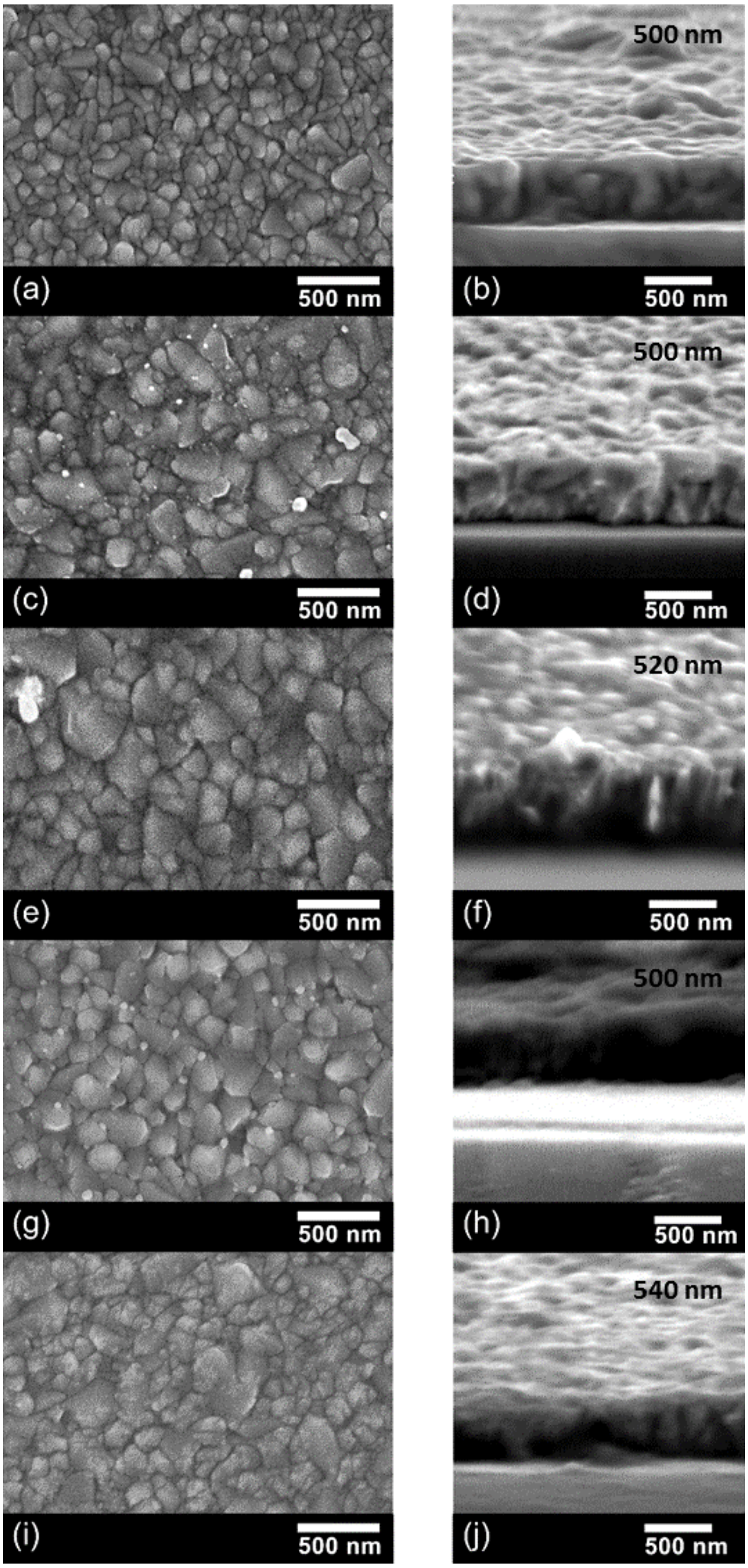

Fig. 6.4. Top down and side on SEM images of WTO thin films deposited *via* single pot AACVD at 450 °C. (a,b) undoped SnO_2 (c,d) $Sn_{0.99}W_{0.01}O_2$ (e,f) $Sn_{0.985}W_{0.015}O_2$ (g,h) $Sn_{0.98}W_{0.02}O_2$ and (i,j) $Sn_{0.97}W_{0.03}O_2$.

6.3.1.4 Optical measurements

The optical measurements of the undoped SnO_2 and WTO films were obtained using a UV/visible/IR spectrometer (Fig. 6.5). All the films were highly transparent and colourless. There was a marginal linear decline in the transparency of the films with increasing amount of dopant incorporation (from 85% to 77%). Maximum reflectance in the infrared region of 45% was achieved when the films were doped regardless of dopant amounts. In contrast to the undoped SnO_2 film produced in Chapter 5, the present film did not show a crossing over of the transmittance and reflectance curves within the IR range analysed. This is a likely consequence of the higher flow rate (1.5 L min^{-1}) used during deposition as a plasma band onset of increased reflectance towards the infrared was seen when the lower flow rate (1.0 L min^{-1}) was used to deposit a SnO_2 in a preliminary experiment for this chapter hence showing the impact flow rate has on growth. As mentioned previously (Section 6.3.1.2), the planes in which the film grows effects its physical properties. From the two undoped SnO_2 films (Chapter 5 and present chapter), preferential growth was found to be different for the two flow rates. The cross over between transmittance and reflectance was seen in the WTO films around 2300 nm, with no apparent shift as a function of dopant quantities. Despite the small decrease seen in transparency with dopant amounts, the band gap remained unchanged, matching that of undoped SnO_2 (3.6 eV).

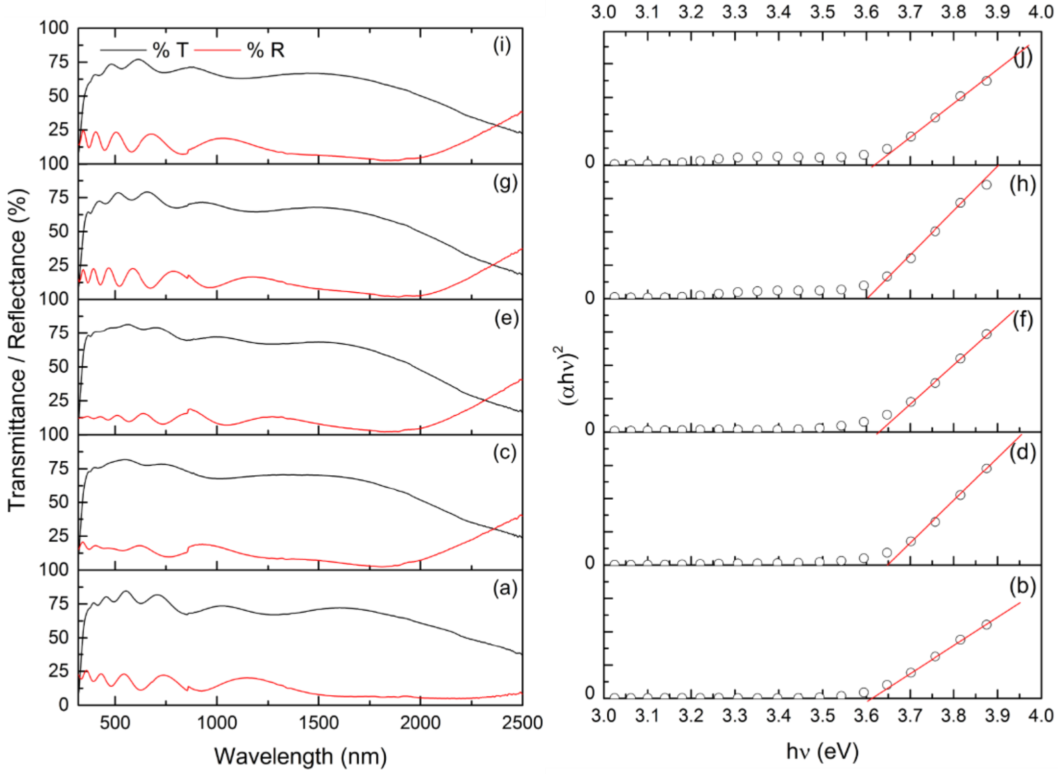

Fig. 6.5. Optical transmittance and reflectance spectra taken with an air background and the Tauc plots for SnO_2 and WTO thin films deposited at 450 °C. (a,b) undoped SnO_2 (c,d) $Sn_{0.99}W_{0.01}O_2$ (e,f) $Sn_{0.985}W_{0.015}O_2$ (g,h) $Sn_{0.98}W_{0.02}O_2$ (i,j) $Sn_{0.97}W_{0.03}O_2$.

6.3.1.5 Electrical properties

The WTO films were all identified as n-type. The films were all roughly the same thickness ranging from 500–540 nm (Table 6.3). Doping with tungsten can lead to reduced resistivities if the number of free charge carriers increases, which is the case if the tungsten is present in an oxidation state above +4. However, high dopant amounts are known to have a detrimental effect on optoelectronic properties. Doping the films resulted in an increase in charge carrier concentration until 1.5 at.% tungsten before reducing again. The trend in conductivity tracked that of carrier concentration but in this study mobility remained similar to undoped SnO_2 for WTO films with up to 3 at.% tungsten. This is unusual as one would expect the mobility to decrease with an increase in carrier concentration due to collisions between charge carriers or the presence of grain boundaries trapping charge carriers. The trend found in the preferred growth planes could explain this observation. The (200) plane has been reported to increase mobility which would explain why mobility had not decreased in the WTO films.[187] In figure 6.3, the (200) plane is favoured over all others for the doped films until dopant amounts reached 3 at.% ($Sn_{0.97}W_{0.03}O_2$), where the (200) plane had significantly reduced preference; this corresponds to an accompanying reduction in mobility. It has been also been reported that doping beyond 2 at.% W leads to some of the W^{6+} being reduced to lower valence states which results in the formation of acceptor states and loss of carriers and hence increase in sheet resistance.[184] This is what was seen in the present study, where a mixture of W^{6+} and W^{4+} was detected by XPS (Table 6.1) and a reduction was seen in carrier concentration as well as an increase in sheet resistance. Doping tin(IV) oxide with tungsten decreased resistivity by approximately 3-fold with the 1.5 at.% tungsten film, $Sn_{0.985}W_{0.015}O_2$, having the optimal sheet resistance of 11.4 $\Omega\ \square^{-1}$. The deposition conditions used for making this film were carried forward to investigate the co-doping of tungsten and fluorine into the SnO_2 lattice.

Table 6.3. Hall effect measurements and film thicknesses of SnO_2 and WTO films. *d*, film thickness; *n*, charge carrier concentration; *μ*, charge carrier mobility; *ρ*, bulk resistivity; R_{sh}, sheet resistance.[*]

Film	*d*/nm	*n*/ × 10^{20} cm^{-3}	*μ*/cm^2 V^{-1} s^{-1}	*ρ*/×10^{-3} Ω cm	R_{sh}/Ω $\square^{-1}$
SnO_2	500	1.100	29.6	1.917	38.3
$Sn_{0.99}W_{0.01}O_2$	500	2.328	33.9	0.791	15.8
$Sn_{0.985}W_{0.015}O_2$	520	3.664	28.9	0.590	11.4
$Sn_{0.98}W_{0.02}O_2$	500	2.483	29.7	0.848	17.0
$Sn_{0.97}W_{0.03}O_2$	540	2.566	10.3	2.368	43.9

---

[*] The electrical properties for the undoped SnO_2 thin film in this chapter differs from the value given in Chapter 5, this is primarily due the slightly different synthetic procedure.

6.3.2 AACVD of WFTO films

Co-doped tungsten and fluorine tin(IV) oxide thin films were deposited based on the conditions used to produce the optimum WTO film, $Sn_{0.985}W_{0.015}O_2$. The conditions for this film was 0.5 mol.% tungsten hexacarbonyl in a butyltin trichloride and methanol solution deposited at 450 °C on barrier coated glass using 1.5 L min^{-1} air. To deposit WFTO films varying amounts of ammonium fluoride (10, 20 and 30 mol.%) was added to the solution.

6.3.2.1 Dopant quantities of the WFTO films

The WFTO films were analysed by EDX, XPS and WDX for the percentage composition of W in bulk, W at the surface and 400 seconds etch time and F in bulk, respectively. Like the GFZO films but unlike the AFTO films discussed in Chapters 4 and 5, respectively, the WFTO films, as confirmed by EDX, had good reproducibility for incorporating the amount of tungsten to match the optimum single doped film (Table 6.4). The oxidation state of tin was confirmed as +4 for all films from XPS where the Sn $3d_{5/2}$ and $3d_{3/2}$ peaks adopted binding energy values in the ranges 483.1-486.3 eV and 494.5-494.7 eV, respectively. The O 1s peak appeared between 529.7-529.9 eV. XPS did not detect W at the surface for the films with 10 and 30 mol.% F, and hence the oxidation state cannot be determined. However, the film with 20 mol.% F found an appreciable amount of W at the surface that allowed the peaks to be modelled; 4.2 at.% W was found with 0.8 at.% as W^{4+} and 3.4 at.% as W^{6+}. The W $4f_{7/2}$ and W $4f_{5/2}$ XPS peaks had binding energy values of 35.4 and 37.5 eV, respectively. The films were also analysed at 400 seconds etch time and there was an apparent reduction in at.% W detected with increasing mol.% of F. Unlike EDX which gives a more representative elemental composition value because it analyses the bulk material, XPS looks at a surface as specified by the etch time. A surprising finding is the reduction in fluorine incorporation with increasing fluorine mol.% in solution. Whilst there is no logical reason for this, the optoelectronic properties were still investigated.

Table 6.4. The relationship between mol.% in solution and at.% of tungsten and fluorine in the films, deposited at 450 °C, determined by energy dispersive X-ray, wavelength dispersive X-ray and X-ray photoelectron spectroscopy at 400 seconds etch time.

mol.% of W in solution	mol.% of F in solution	at.% of W determined by EDX	at.% of W determined by XPS	at.% of F determined by WDX
0.5	10	1.5	0.5	1.1
0.5	20	1.5	0.8	0.8
0.5	30	1.5	0.4	0.5

6.3.2.2 Crystal structure

Adding a second dopant the films remained polycrystalline, matching the lattice structure of tetragonal rutile SnO_2 (Fig. 6.6). The crystallite size calculated for the WFTO films were in the same range as those found in the singe doped WTO films (Table 6.5). The unexpected discrepancy observed for the change in unit cell is unlikely to be a real phenomenon for two reasons: As the error value in the calculated unit cell volume for undoped SnO_2 is large, the percentage change in volume for the co-doped films relative to the undoped SnO_2 would also have large associated errors. Secondly, the software (GSAS and EXPGUI), used to fit the XRD data in order to calculate the unit cell volume, requires a certain level of human judgement which together with the numerous variables involved in the calculation can result in estimations that give marginal results (Table 6.5). Therefore, in this instance the values for percentage volume change should be interpreted tentatively.

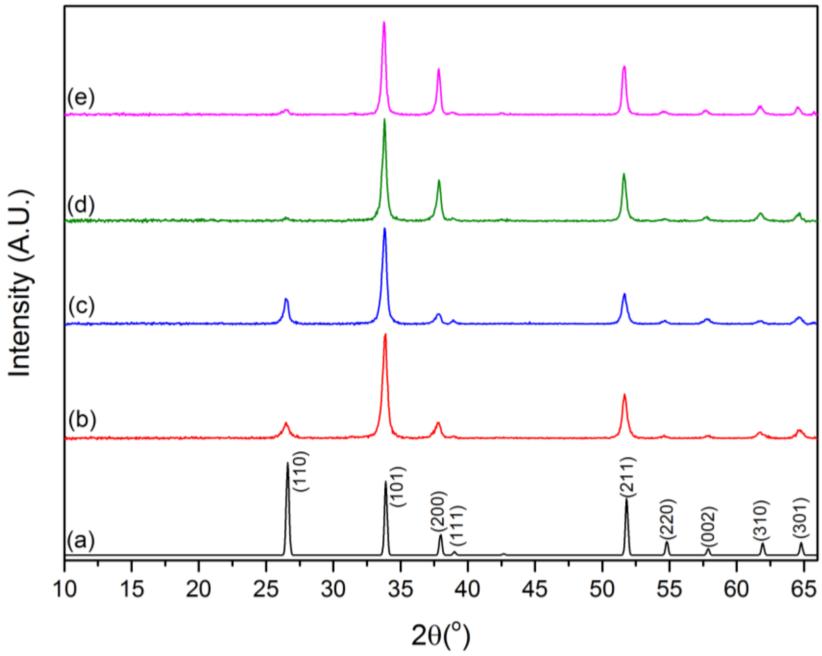

Fig. 6.6. XRD patterns of SnO_2 and WFTO thin films deposited *via* single pot AACVD system at 450 °C. (a) standard SnO_2[166] (b) undoped SnO_2 (c) $Sn_{0.98}W_{0.015}F_{0.005}O_2$ (d) $Sn_{0.977}W_{0.015}F_{0.008}O_2$ (e) $Sn_{0.974}W_{0.015}F_{0.011}O_2$.

Table 6.5. Variation in the mean crystallite diameter and unit cell parameters of SnO_2 and WFTO thin films with different dopant concentrations of NH_4F.

Film	Mean crystallite diameter /nm	a /Å	c /Å	Unit cell volume /Å³	Volume contraction /%
SnO_2	18	4.7594(12)	3.1891(7)	72.239(31)	
$Sn_{0.98}W_{0.015}F_{0.005}O_2$	19	4.7581(5)	3.1928(3)	72.283(13)	0.06 (expansion)
$Sn_{0.977}W_{0.015}F_{0.008}O_2$	21	4.7534(4)	3.1960(3)	72.212(11)	0.04
$Sn_{0.974}W_{0.015}F_{0.011}O_2$	21	4.7559(3)	3.1991(3)	72.361(9)	0.17 (expansion)

In undoped SnO_2 the (101), (200), (211), (310) and (301) planes showed preferential growth. The (200) plane for the single doped 1.5 at.% WTO film, on which the WFTO films are based on, showed double the preference in growth along this plane. In general, this was also observed in the WFTO films. Furthermore, co-doping with fluorine resulted in a small increase in preferred orientation along the (111) and (002) planes, and a small decline in growth preference along the (110) plane (Fig. 6.7). Contrasting results have been found by Turgut *et al.*,[184] the only other known study on WFTO films, who found that initially when co-doped the preferred growth was along the (211) plane and with increasing amounts of tungsten dopant (their fluorine content remained constant), the (200) followed by the (110) plane became preferred.

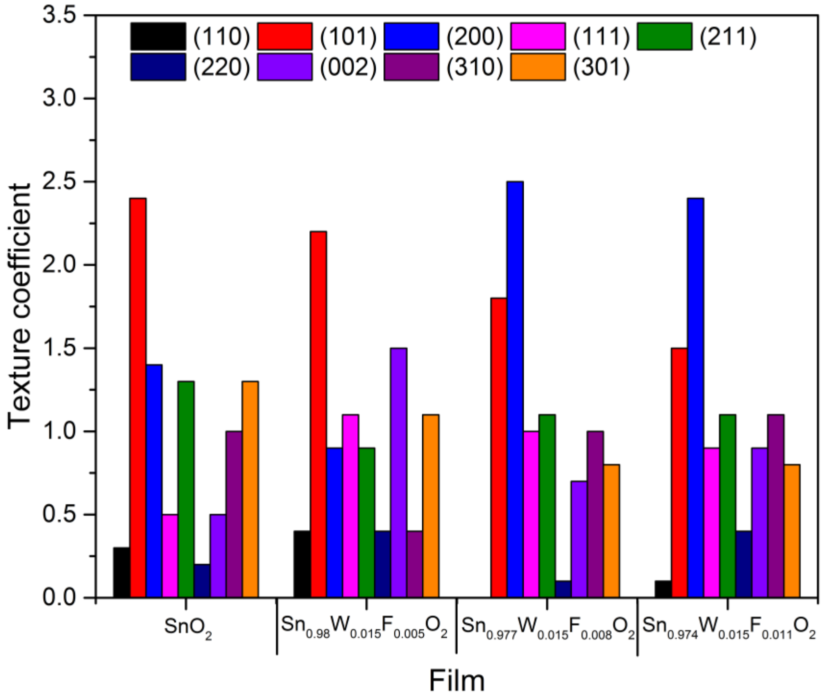

Fig. 6.7. Variation of the texture coefficient (Tc) of each plane with 1.5 at.% W and varying amounts of F dopant in SnO_2.

6.3.2.3 Surface morphology

The morphology of the WFTO films consisting of the least amount of fluorine (0.5 at.%) bears a striking resemblance to the single doped 1.5 at.% WTO film (Fig. 6.8a and c). However, the average particle size was about half that, approximately 200 nm. At 0.8 at.% F, the particle size further decreased with the edges becoming smoother resulting in a flatter and more compact film appearance (Fig. 6.8e). At the highest F content, the morphology appeared flat but with obvious clusters separated by defined boundaries (Fig. 6.8g). The film thicknesses matched that of the single doped films apart from the $Sn_{0.98}W_{0.015}F_{0.005}O_2$ film which was slightly thinner having a thickness of 300 nm (Fig. 6.8d). There is no plausible explanation as to why the film deposited was thinner as apart from changing the fluorine content the other variables remained the same, and it is clear to see that the fluorine amounts do not affect film thickness as the films with higher F content were within the 500–550 nm range (Fig. 6.8f and h).

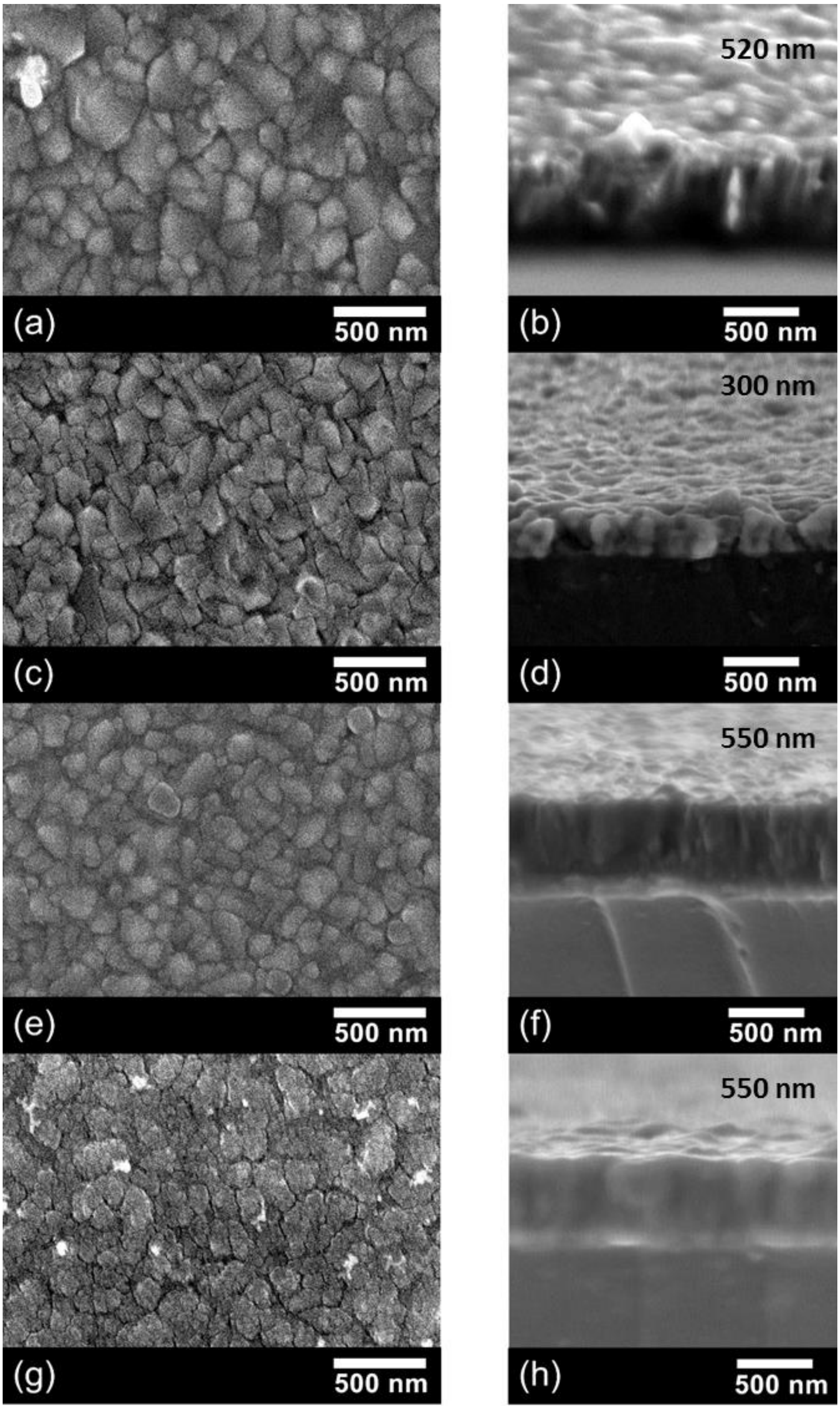

Fig. 6.8. Top down and side on SEM images of WFTO thin films (compared with 1.5 at.% WTO) deposited *via* single pot AACVD at 450 °C. (a,b) $Sn_{0.985}W_{0.015}O_2$ (c,d) $Sn_{0.98}W_{0.015}F_{0.005}O_2$ (e,f) $Sn_{0.977}W_{0.015}F_{0.008}O_2$ (g,h) $Sn_{0.974}W_{0.015}F_{0.011}O_2$.

6.3.2.4 Optical measurements

The optical measurements were taken as mentioned in Section 6.3.1.4 (Fig. 6.9). The WFTO thin films were transparent and colourless. A striking observation found with the co-doped films was the marked blue shifting of the plasma edge (the onset of the increase in reflectance), with the greatest shift reaching a wavelength of approximately 1500 nm. Furthermore, this film also had a maximum reflectance of 90%. The blue shift of the plasma edge is in line with the higher charge carrier concentrations compared with undoped SnO_2 and single doped WTO films (Table 6.3 and 6.6). Moreover, the transmittance and reflectance profile observed for the WFTO films are also a feature of FTO films.[20] The interference fringes seen in the transmission curve is a function of film thickness (Table 6.6). As expected, the band gaps remained at 3.6 eV regardless of film composition because transmittance were similar.

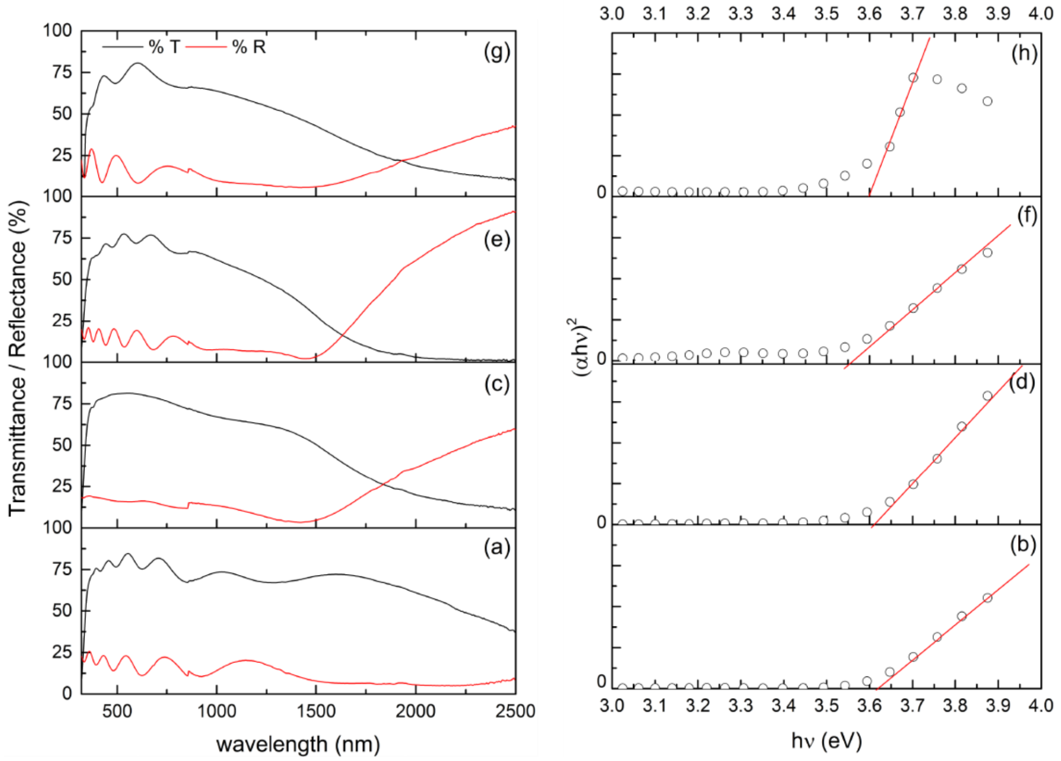

Fig. 6.9. Optical transmittance and reflectance spectra taken with an air background and the Tauc plots for SnO_2 and WFTO thin films deposited at 450 °C. (a,b) undoped SnO_2 (c,d) $Sn_{0.98}W_{0.015}F_{0.005}O_2$ (e,f) $Sn_{0.977}W_{0.015}F_{0.008}O_2$ (g,h) $Sn_{0.974}W_{0.015}F_{0.011}O_2$.

6.3.2.5 Electrical properties

The WFTO thin films were also identified as n-type. Apart from $Sn_{0.98}W_{0.015}F_{0.005}O_2$, the remaining films were of similar thickness (Table 6.6). Therefore, the unusually high sheet resistance, despite a greater charge carrier concentration compared with WTO films, is a consequence of it being a much thinner film. Comparing the 0.8 at.% and 1.1 at.% fluorine WFTO films there is a small decrease in charger carrier concentration which in turn leads to an increase in resistivity. The mobility of these films is similar and this can be again attributed to the preferred film growth in the (200) plane (Fig. 6.7 and see Section 6.3.1.5). A study by Turgut e*t al.* deposited WFTO films *via* a spray pyrolysis method by varying the tungsten amounts between 1-5 at.% and keeping the F content constant at 20 at.%. They achieved resistances as low as 1.12 Ω.[184] However, *via* AACVD it is difficult to incorporate such large amounts of fluoride ions (Section 3.3.2). The optimal optoelectronic properties were observed for the $Sn_{0.977}W_{0.015}F_{0.008}O_2$ film with a sheet resistance of 9.7 Ω □$^{-1}$ which is slightly better than the optimal single doped WTO film. This could be a consequence of the morphology being smoother and more compact (Fig. 6.8e).

Table 6.6. Hall effect measurements and film thicknesses of SnO_2 and WFTO films. *d*, film thickness; *n*, charge carrier concentration; *μ*, charge carrier mobility; *ρ*, bulk resistivity; R_{sh}, sheet resistance.*

Film	d/nm	n/ ×10^{20} cm^{-3}	μ/cm^2 V^{-1} s^{-1}	ρ/×10^{-3} Ω cm	R_{sh}/Ω □$^{-1}$
SnO_2	500	1.100	29.6	1.917	38.3
$Sn_{0.98}W_{0.015}F_{0.005}O_2$	300	5.646	18.03	0.613	20.4
$Sn_{0.977}W_{0.015}F_{0.008}O_2$	550	7.979	14.63	0.535	9.7
$Sn_{0.974}W_{0.015}F_{0.011}O_2$	550	6.123	14.78	0.690	12.5

---

* The electrical properties for the undoped SnO_2 thin film in this chapter differs from the value given in Chapter 5, this is primarily due the slightly different synthetic procedure.

6.4 Conclusions

Tungsten doped and tungsten-fluorine co-doped thin films were successfully deposited on to glass substrates with excellent coverage *via* aerosol assisted chemical vapour deposition (AACVD). The films were colourless and exhibited superior optoelectronic properties. For this system, the required mol.% of the dopant amount in solution was much lower than any other system mentioned in this thesis. This is because there are two electrons donated into the conduction band when W^{6+} replaces an Sn^{4+} atom. At the higher amounts of tungsten dopant (greater than 1.5 at.%), two oxidation states were present with +6 being the more predominate state over the +4. For the co-doped films the amount of tungsten remained the same as in the best single doped film ($Sn_{0.985}W_{0.015}O_2$ with a sheet resistance of 11.4 $\Omega\ \square^{-1}$), allowing them to be compared in the same way as the films were in chapter 4. All the films produced in the present chapter were polycrystalline and the incorporation of tungsten into the SnO_2 lattice resulted in a preference for the film to grow along the (200) plane. The general morphology of the WTO films was similar, although the range of particle sizes widened with increasing amounts of dopant. The addition of fluorine into the system resulted in the particles becoming more rounded. All films, WTO and WFTO, exhibited transmittance of about 80% meeting one of the main requirements of TCO. Co-doping further blue-shifted the onset of the plasma edge making the films more ideal for applications such as heat mirrors. The electronic properties of the films were also enhanced by co-doping, unlike the unexpected result in chapter 5, with the best film, $Sn_{0.977}W_{0.015}F_{0.008}O_2$, having a sheet resistance of 9.7 $\Omega\ \square^{-1}$.

7

General conclusions and future work

7.1 General conclusions

Aerosol assisted chemical vapour deposition (AACVD) proved to be a reliable and simple method for the deposition of thin films exhibiting the characteristics favoured in TCOs. The apparatus was easily adaptable to coping with multiple precursors and more than one solvent system. There were two main foci of this thesis were:

1. to investigate the suitability of AACVD in working with low-cost precursors in depositing undoped and single doped metal oxide films based on zinc and tin.
2. to enhance the optoelectronic properties of doped films by the introduction of a second dopant, namely fluorine which replaces the oxide ion in the metal oxide lattice. Fluorine was chosen because of its established use in FTO, a commercially available TCO.

In this thesis 31 films were analysed and discussed in the context of their optoelectronic properties. Table 7.1 summarises the maximum percentage transmittance in the visible and the sheet resistance for the optimum films, with the film showing the best compromise between the two factors highlighted. All films exhibited transparencies around the 80% mark (one of the requirements for a TCO) except for the antimony doped films from chapter 5 as a consequence of them being coloured. All films were compared to an undoped ZnO or SnO_2 film and when deposition conditions were identical, the reproducibility of the undoped films was evident from their similar sheet resistance values.

Zinc oxide films doped with aluminium or/and fluorine (Chapter 3) exhibited the same degree of transparency. The sheet resistance values showed that FZO was the better TCO. However, a closer examination of optical properties found that the crossover of the transmittance and reflectance curves for the co-doped AFZO film was blue shifted. This would make this film more suitable for applications as a heat mirror. Furthermore, whilst the AZO film had the poorest conductivity out of the three, it was still superior to the undoped ZnO for this system ($54.6\ \Omega\ \square^{-1}$ vs $75.1\ \Omega\ \square^{-1}$). At this stage in the discussion, it is important to emphasise that the approach taken to establish the conditions for producing the co-doped film was different to the one taken in subsequent chapters. In Chapter 3, the conditions used to produce the optimum AZO film and the optimum FZO film were incorporated to produce a single co-doped AFZO film. However, the desired film composition of 1 at.% Al and 1 at.% F into ZnO was not achieved and hence this co-doped film may not have the compositional attributes of the best AFZO film that could have been synthesised. In subsequent chapters, the concentration of the anion dopant was varied after establishing the ideal conditions for the single cation doped films.

Following on from Chapter 3, gallium doped into zinc oxide was investigated in Chapter 4 because of the similarity in ionic radii of Zn^{2+} and Ga^{3+}. Undoped ZnO for this system had a sheet resistance of $53.6\ \Omega\ \square^{-1}$ which reduced 3-fold to $17.6\ \Omega\ \square^{-1}$ for the optimum single doped GZO film, $Zn_{0.95}Ga_{0.05}O$. This corresponded with a 3-fold increase in the charge carrier concentration (ZnO: $1.362 \times 10^{20}\ cm^{-3}$; $Zn_{0.95}Ga_{0.05}O$: $4.230 \times 10^{20}\ cm^{-3}$). The co-doped film, $Zn_{0.94}Ga_{0.05}F_{0.01}O$, not only had a marginally greater transparency but an even lower sheet resistance than the GZO and other GFZO films. This film emerged as the one with the best optimal optoelectronic properties out of the 31 films characterised. A likely reason why films containing gallium over aluminium have better electrical properties maybe a consequence of Ga_2O_3 having a less exothermic enthalpy of formation compared with Al_2O_3 and hence more likely for Ga^{3+} to substitute the Zn^{2+} than form a non-conducting oxide.

Moving away from the ZnO lattice, the SnO_2 lattice was investigated in Chapter 5. Antimony was introduced into the lattice followed by antimony and fluorine. The ATO films were blue in colour which darkened with increasing amounts of dopant incorporation; transparency decreased from 80% to 45% transmittance. The AFTO films were black which remained at a transparency of about 40% regardless of the amount of fluorine incorporation. These coloured films are valued in architecture for aesthetic appeal. The single doped $Sn_{0.96}Sb_{0.04}O_2$ film exhibited the lowest sheet resistance out of the 31 films investigated. Co-doping in this system surprisingly did not increase conductivity despite FTO being a commercially available TCO. However, the $Sn_{0.98}Sb_{0.01}F_{0.01}O_2$ AFTO film approximately halved in its sheet resistance value compared with undoped SnO_2.

The final experimental chapter explored another tin(IV) oxide system, this time doped with tungsten or tungsten and fluorine. The optimum films produced in this system (Table 7.1) were similar in regards to their transmittance in the visible and conductivity. The sheet resistance for the WFTO film was four times lower compared with the undoped SnO_2 ($9.7\ \Omega\ \square^{-1}$ vs $38.3\ \Omega\ \square^{-1}$). The optoelectronic properties of the films can be tuned to suit specific applications by altering the film composition. For example, the onset of the increase in reflection in the infrared is blue-shifted to lower wavelengths for the GFZO films compared with the GZO films making them more suitable for use as heat mirrors. In general, all the doped and co-doped films discussed in this thesis had plasma edge onsets blue shifted to 1500 nm or less except for WTO films.

Table 7.1. Summary of the optoelectronic properties of the optimum films deposited in Chapters 3-6.

Chapter	**Optimum films**	**Maximum transmittance in the visible /%**	**Sheet resistance /$\Omega\ \square^{-1}$**
3	$Zn_{0.99}Al_{0.01}O$	84	54.6
	$Zn_{0.99}F_{0.01}O$	84	33.1
	$Zn_{0.97}Al_{0.02}F_{0.01}O$	84	53.3
4	$Zn_{0.95}Ga_{0.05}O$	84	17.6
	$Zn_{0.94}Ga_{0.05}F_{0.01}O$	85	12.2
5	$Sn_{0.96}Sb_{0.04}O_2$	65	9.0
	$Sn_{0.98}Sb_{0.01}F_{0.01}O_2$	40	19.4
6	$Sn_{0.985}W_{0.015}O_2$	81	11.4
	$Sn_{0.977}W_{0.015}F_{0.008}O_2$	77	9.7

Overall, the thesis has confirmed the reliability of AACVD in producing TCO thin films. The method was easily modifiable to accommodate for the chemical nature of a variety of precursors and allowed control over dopant incorporation into the metal oxide lattice. In three of the four different systems tested, fluorine proved to be an effective co-dopant, improving the sheet resistance compared with their single doped equivalent and the undoped metal oxide film. Industry standard FTO glass is available with sheet resistances between 7 and 20 Ω □$^{-1}$ and transparencies between 80 to 84%.[188] The films with the optimum optoelectronic properties from the work described in Chapters 4 and 6 fall within these industry standards. This thesis for the first time, to my knowledge, presents studies on GFZO and WFTO produced *via* a CVD method. Prior to this these co-doped systems have been synthesised once only by a PVD (GFZO) and wet chemical (WFTO) methods. Furthermore, the tunability of the films *via* AACVD would allow further improvements in the film properties now that a base line for performance has been established in this thesis.

7.2 Future work

An obvious future direction is to further fine-tune some of the optimum films (Table 7.1) by varying the deposition conditions. As previously mentioned, aerosol assisted chemical vapour deposition (AACVD) has proved to be a reliable and simple method for thin film coatings where a volatile precursor is no longer a requirement. This leads to an increase in the range of precursors that can potentially be used for CVD, and hence experiments can be carefully designed to use precursors that will have minimum impact on the environment. Sustainability is becoming an increasingly important consideration in the production of future functional materials. The films manufactured in this thesis were based on zinc oxide using pyrophoric diethyl zinc and tin(IV) oxide using the halogenated precursor, butyltin trichloride. It is worth moving away from these precursors to ones that are easier to handle and produce non-toxic waste, without compromising film properties and potentially even bettering existing films.

In order for AACVD to be an industrial process it needs to overcome a few challenges with the main one being the growth rate of films.[189] In a research laboratory an AACVD experiment can take between 20-90 minutes depending on the required film thickness. This is too slow for industrial scale manufacture where rates are typically 1000's nm min^{-1}. A previous study has shown that the growth rate using AACVD can be scaled from 10 to 100 nm min^{-1} without a loss in functionality.[190] This shows that AACVD has the potential to be scaled to meet industrial requirements, however more research is required to reach the desired growth rates. Therefore, increasing film growth rates and improving sustainability of the CVD process, with no effect on film functionality, is an area that needs establishing.

Furthermore, the work discussed has so far been based on n-type transparent conducting oxides (TCOs). There is still a need to find a p-type TCO that exhibits optical transparency and electronic conductivity comparable with the current universal n-type industry leaders, ITO and FTO. The formation of such a material would allow the production of a p-n junction, revolutionising the electronics industry for the better. SnO is a promising p-type material however it is difficult to produce due to the disproportionation of the tin species at elevated temperatures. There has been computational studies suggesting the find for new materials that exhibit p-type conductivity which include Mg doped Cr_2O_3[191] and MCuP where M=Mg, Ca, Sr or Ba.[192] Research into these materials would be a good starting point to potentially discover a p-type material.

8. References

1. Fan, J. C. C.; Bachner, F. J. Transparent heat mirrors for solar-energy applications. *Appl. Opt.* **1976,** *15* (4), 1012-1017.
2. Viguié, J. C.; Spitz, J. Chemical Vapor Deposition at Low Temperatures. *Journal of The Electrochemical Society* **1975,** *122* (4), 585-588.
3. Kodas, T. T.; Hampden-Smith, M. J. Overview of Metal CVD. In *The Chemistry of Metal CVD*; Wiley-VCH, 1994, pp 429-498.
4. Kodas, T. T.; Hampden-Smith, M. J. *Aerosol Processing of Materials*; Wiley - VCH 1999. p 712.
5. Savile Bradbury, B. J. F., David C. Joy. Scanning electron microsope. https://www.britannica.com/technology/scanning-electron-microscope.
6. Robertson, J.; Falabretti, B. Electronic Structure of Transparent Conducting Oxides. In *Handbook of Transparent Conductors*, Ginley, D. S., Ed.; Springer US: Boston, MA, 2011, pp 27-50.
7. Yang, Y.; Jin, S.; Medvedeva, J. E.; Ireland, J. R.; Metz, A. W.; Ni, J.; Hersam, M. C.; Freeman, A. J.; Marks, T. J. CdO as the Archetypical Transparent Conducting Oxide. Systematics of Dopant Ionic Radius and Electronic Structure Effects on Charge Transport and Band Structure. *Journal of the American Chemical Society* **2005,** *127* (24), 8796-8804.
8. Srikant, V.; Clarke, D. R. On the optical band gap of zinc oxide. *Journal of Applied Physics* **1998,** *83* (10), 5447-5451.
9. Jackson, S. D.; Hargreaves, J. S. J. *Metal Oxide Catalysis*; Wiley - VCH: 2009; p. 866.
10. Mattox, D. M. *Handbook of Physical Vapor Deposition (PVD) Processing*; 2nd ed.; Elsevier: Oxford, 2010. p 792.
11. Creighton, J. R.; Ho, P. Introduction to chemical vapor depoisiton (CVD). In *Chemical Vapor Deposition*; ASM International: Albuquerqu, 2011, pp 1-22.
12. Choy, K. L. Chemical vapour deposition of coatings. *Progress in Materials Science* **2003,** *48* (2), 57-170.
13. Tauc, J. Optical properties and electronic structure of amorphous Ge and Si. *Materials Research Bulletin* **1968,** *3* (1), 37-46.
14. Bhachu, D. S.; Sankar, G.; Parkin, I. P. Aerosol Assisted Chemical Vapor Deposition of Transparent Conductive Zinc Oxide Films. *Chemistry of Materials* **2012,** *24* (24), 4704-4710.
15. Tadatsugu, M. Transparent conducting oxide semiconductors for transparent electrodes. *Semiconductor Science and Technology* **2005,** *20* (4), S35.
16. Noor, N.; Parkin, I. P. Enhanced transparent-conducting fluorine-doped tin oxide films formed by Aerosol-Assisted Chemical Vapour Deposition. *Journal of Materials Chemistry C* **2013,** *1* (5), 984-996.
17. Thomas, G. Materials science: Invisible circuits. *Nature* **1997,** *389* (6654), 907-908.
18. Banerjee, A. N.; Chattopadhyay, K. K. Recent developments in the emerging field of crystalline p-type transparent conducting oxide thin films. *Progress in Crystal Growth and Characterization of Materials* **2005,** *50* (1–3), 52-105.
19. Bright, C. I. Review of Transparent Conductive Oxides (TCO). In *50 Years of Vacuum Coating Technology and the Growth of the Society of Vacuum Coaters*, Mattox, D. M.; Mattox, V. H., Ed.; Society of Vacuum Coaters: Tuscon, Arizona, 2007, pp 38-45.
20. Chew, C. K. T.; Salcianu, C.; Bishop, P.; Carmalt, C. J.; Parkin, I. P. Functional thin film coatings incorporating gold nanoparticles in a transparent conducting

fluorine doped tin oxide matrix. *Journal of Materials Chemistry C* **2015,** *3* (5), 1118-1125.

21. Bhachu, D. S.; Waugh, M. R.; Zeissler, K.; Branford, W. R.; Parkin, I. P. Textured Fluorine-Doped Tin Dioxide Films formed by Chemical Vapour Deposition. *Chemistry – A European Journal* **2011,** *17* (41), 11613-11621.

22. Kahraman, S.; Çakmak, H. M.; Çetinkaya, S.; Bayansal, F.; Çetinkara, H. A.; Güder, H. S. Characteristics of ZnO thin films doped by various elements. *Journal of Crystal Growth* **2013,** *363*, 86-92.

23. Jin, S.; Yang, Y.; Medvedeva, J. E.; Wang, L.; Li, S.; Cortes, N.; Ireland, J. R.; Metz, A. W.; Ni, J.; Hersam, M. C.; Freeman, A. J.; Marks, T. J. Tuning the Properties of Transparent Oxide Conductors. Dopant Ion Size and Electronic Structure Effects on CdO-Based Transparent Conducting Oxides. Ga- and In-Doped CdO Thin Films Grown by MOCVD. *Chemistry of Materials* **2007,** *20* (1), 220-230.

24. Ridley, B. K. Large-bandgapsemiconductors. *Turkish Journal of Physics* **1999,** *23*, 577-582.

25. Fujita, M. Silicon photonics: Nanocavity brightens silicon. *Nat Photon* **2013,** *7* (4), 264-265.

26. Pauling, L. The nature of the chemical bond. IV. The energy of single bonds and the relative electronegativity of atoms. *Journal of the American Chemical Society* **1932,** *54* (9), 3570-3582.

27. Dagenais, K.; Chamberlin, M.; Constantin, C. Modeling energy band gap as a function of optical electronegativity for binary oxides. *Journal of Young Investigators* **2013,** *25*, 73-78.

28. Mishra, S.; Ganguli, B. Effect of p–d hybridization, structural distortion and cation electronegativity on electronic properties of $ZnSnX_2$ (X=P, As, Sb) chalcopyrite semiconductors. *Journal of Solid State Chemistry* **2013,** *200*, 279-286.

29. Chen, S.; Gong, X.; Wei, S.-H. Band-structure anomalies of the chalcopyrite semiconductors $CuGaX_2$ versus $AgGaX_2$ (X=S and Se) and their alloys. *Physical Review B* **2007,** *75* (20), 205209.

30. McCluskey, M. D.; Haller, E. E. *Dopants and Defects in Semiconductors*; 1st ed.; CRC Press 2012. p 390.

31. King, P. D. C.; Veal, T. D. Conductivity in transparent oxide semiconductors. *Journal of Physics: Condensed Matter* **2011,** *23* (33), 334214.

32. McCluskey, M. D.; Jokela, S. J. Defects in ZnO. *Journal of Applied Physics* **2009,** *106* (7), 071101.

33. Janotti, A.; Van de Walle, C. G. Native point defects in ZnO. *Physical Review B* **2007,** *76* (16), 165202.

34. Ganose, A. M.; Scanlon, D. O. Band gap and work function tailoring of SnO_2 for improved transparent conducting ability in photovoltaics. *Journal of Materials Chemistry C* **2016,** *4* (7), 1467-1475.

35. Kumar, J.; Amit, K. S. Band gap narrowing in zinc oxide-based semiconductor thin films. *Journal of Applied Physics* **2014,** *115* (13), 134904.

36. Yousaf, S. A.; Ali, S. The effect of fluorine doping on optoelectronic properties of tin-dioxide ($F:SnO_2$) thin films. *Journal of Natural Sciences and Mathmatics* **2009,** *48*, 43-50.

37. Dakhel, A. A. Study of high mobility carriers in Ni-doped CdO films. *Bull Mater Sci* **2013,** *36* (5), 819-825.

38. Jiang, Y.; Sun, W.; Xu, B.; Yan, M.; Bahlawane, N. Unusual enhancement in electrical conductivity of tin oxide thin films with zinc doping. *Physical Chemistry Chemical Physics* **2011,** *13* (13), 5760-5763.

39. Castañeda, L. Present status of the development and application of transparent conductors oxide thin solid films. *Materials Sciences and Applications* **2011,** *2*, 1233-1242.

40. Joseph, U.; Sarah Eunkyung, K. Homo-Junction pn Diode Using p-Type SnO and n-Type SnO_2 Thin Films. *ECS Solid State Letters* **2014,** *3* (8), 94-98.

41. Savarimuthu, E.; Lalithambika, K. C.; Moses Ezhil Raj, A.; Nehru, L. C.; Ramamurthy, S.; Thayumanavan, A.; Sanjeeviraja, C.; Jayachandran, M. Synthesis and materials properties of transparent conducting In_2O_3 films prepared by sol–gel-spin coating technique. *Journal of Physics and Chemistry of Solids* **2007,** *68* (7), 1380-1389.

42. Sato, H.; Minami, T.; Takata, S.; Yamada, T. Transparent conducting p-type NiO thin films prepared by magnetron sputtering. *Thin Solid Films* **1993,** *236* (1–2), 27-31.

43. Sheng, S.; Fang, G.; Li, C.; Xu, S.; Zhao, X. p-type transparent conducting oxides. *physica status solidi (a)* **2006,** *203* (8), 1891-1900.

44. Kawazoe, H.; Yasukawa, M.; Hyodo, H.; Kurita, M.; Yanagi, H.; Hosono, H. P-type electrical conduction in transparent thin films of $CuAlO_2$. *Nature* **1997,** *389* (6654), 939-942.

45. Banerjee, A.; Chattopadhyay, K. K.; Joo, S. W. Wet-chemical dip-coating preparation of highly oriented copper–aluminum oxide thin film and its opto-electrical characterization. *Physica B: Condensed Matter* **2011,** *406* (2), 220-224.

46. Bouzidi, C.; Bouzouita, H.; Timoumi, A.; Rezig, B. Fabrication and characterization of $CuAlO_2$ transparent thin films prepared by spray technique. *Materials Science and Engineering: B* **2005,** *118* (1–3), 259-263.

47. Saha, B.; Thapa, R.; Chattopadhyay, K. K. A novel route for the low temperature synthesis of p-type transparent semiconducting $CuAlO_2$. *Materials Letters* **2009,** *63* (3–4), 394-396.

48. Neumann-Spallart, M.; Pinto, R. Growth conditions of $CuAlO_2$ films — Thermodynamic considerations. *Thin Solid Films* **2011,** *520* (4), 1299-1302.

49. Gong, H.; Wang, Y.; Luo, Y. Nanocrystalline p-type transparent Cu–Al–O semiconductor prepared by chemical-vapor deposition with $Cu(acac)_2$ and $Al(acac)_3$ precursors. *Applied Physics Letters* **2000,** *76* (26), 3959-3961.

50. Zhang, Y.; Liu, Z.; Zang, D.; Feng, L. Structural and opto-electrical properties of Cu–Al–O thin films prepared by magnetron sputtering method. *Vacuum* **2014,** *99*, 160-165.

51. Banerjee, A. N.; Maity, R.; Chattopadhyay, K. K. Preparation of p-type transparent conducting $CuAlO_2$ thin films by reactive DC sputtering. *Materials Letters* **2004,** *58* (1–2), 10-13.

52. Chiu, S. H.; Huang, J. C. A. Characterization of p-type $CuAlO_2$ thin films grown by chemical solution deposition. *Surface and Coatings Technology* **2013,** *231*, 239-242.

53. Shanmin, G.; Yan, Z.; Pingping, G.; Nan, C.; Yi, X. Preparation of $CuAlO_2$ nanocrystalline transparent thin films with high conductivity. *Nanotechnology* **2003,** *14* (5), 538-541.

54. Allen, J. P.; Scanlon, D. O.; Parker, S. C.; Watson, G. W. Tin Monoxide: Structural Prediction from First Principles Calculations with van der Waals Corrections. *The Journal of Physical Chemistry C* **2011,** *115* (40), 19916-19924.

55. Ogo, Y.; Hiramatsu, H.; Nomura, K.; Yanagi, H.; Kamiya, T.; Hirano, M.; Hosono, H. p-channel thin-film transistor using p-type oxide semiconductor, SnO. *Applied Physics Letters* **2008,** *93* (3), 032113.

56. Chattopadhyay D.; Rakshit, P. C. *Electronics Fundamentals and Applications*; New Age International (P) Limited 2008.

57. Tyagi, M.; Tomar, M.; Gupta, V. P-N Junction of NiO Thin Film for Photonic Devices. *Electron Device Letters, IEEE* **2013,** *34* (1), 81-83.

58. Sathyamoorthy, R.; Abhirami, K. M.; Gokul, B.; Gautam, S.; Chae, K.; Asokan, K. Fabrication of p-n junction diode using SnO/SnO_2 thin films and its device characteristics. *Electron. Mater. Lett.* **2014,** *10* (4), 743-747.

59. Morkoç, H.; Özgür, Ü. General Properties of ZnO. In *Zinc Oxide*; Wiley-VCH, 2009, pp 1-76.

60. Neri, G. First Fifty Years of Chemoresistive Gas Sensors. *Chemosensors* **2015,** *3* (1), 1.

61. Coleman, V. A.; Jagadish, C. Chapter 1 - Basic Properties and Applications of ZnO. In *Zinc Oxide Bulk, Thin Films and Nanostructures*; Elsevier Science Ltd: Oxford, 2006, pp 1-20.

62. Vogel, D.; Krüger, P.; Pollmann, J. Ab initio electronic-structure calculations for II-VI semiconductors using self-interaction-corrected pseudopotentials 1995; Vol. 52. p 14316-14319.

63. Liu, Y.; Li, Y.; Zeng, H. ZnO-Based Transparent Conductive Thin Films: Doping, Performance, and Processing. *Journal of Nanomaterials* **2013,** *2013*, 9.

64. Wang, M.; Gao, Y.; Chen, Z.; Cao, C.; Zhou, J.; Dai, L.; Guo, X. Transparent and Conductive W-Doped SnO2 Thin Films Fabricated by an Aqueous Solution Process. *Thin Solid Films* 2013; Vol. 544. p 419-426.

65. González, G. B. Investigating the Defect Structures in Transparent Conducting Oxides Using X-ray and Neutron Scattering Techniques. *Materials* **2012,** *5* (5).

66. Jarzebski, Z. M.; Marton, J. P. Physical Properties of SnO_2 Materials: II . Electrical Properties. *Journal of The Electrochemical Society* **1976,** *123* (9), 299C-310C.

67. Kılıç, Ç.; Zunger, A. Origins of Coexistence of Conductivity and Transparency in SnO_2. *Physical Review Letters* **2002,** *88* (9), 095501.

68. Singh, A. K.; Janotti, A.; Scheffler, M.; Van de Walle, C. G. Sources of Electrical Conductivity in SnO_2. *Physical Review Letters* **2008,** *101* (5), 055502.

69. Fortunato, E.; Ginley, D.; Hosono, H.; Paine, D. C. Transparent Conducting Oxides for Photovoltaics. *MRS Bulletin* **2011,** *32* (3), 242-247.

70. Luque, A.; Hegedus, S. Handbook of photovoltaic science and engineering. In *Chapter 1: Achievements and challenges of solar electricity from photovoltaics*; John Wiley & Sons, 2011; Vol. 2.

71. Ravichandran, K.; Jabena Begum, N.; Snega, S.; Sakthivel, B. Properties of Sprayed Aluminum-Doped Zinc Oxide Films—A Review. *Materials and Manufacturing Processes* **2016,** *31* (11), 1411-1423.

72. Lampert, C. M. Heat mirror coatings for energy conserving windows. *Solar Energy Materials* **1981,** *6* (1), 1-41.

73. Dobrikov, G. H.; Rassovska, M. M.; Andreev, N. M.; Boyadzhiev, S. I.; Gesheva, K. A.; Ivanova, T. M.; Sharlandjiev, P. S.; Nazarowa, D. I. Development of transparent heat mirrors based on metal oxide thin film structures. *Thin Solid Films* **2009,** *518* (4), 1091-1094.

74. Gong, L.; Ye, Z.; Lu, J.; Zhu, L.; Huang, J.; Gu, X.; Zhao, B. Highly transparent conductive and near-infrared reflective ZnO:Al thin films. *Vacuum* **2010,** *84* (7), 947-952.

75. Durrani, S. M. A.; Khawaja, E. E.; Al-Shukri, A. M.; Al-Kuhaili, M. F. Dielectric/Ag/dielectric coated energy-efficient glass windows for warm climates. *Energy and Buildings* **2004,** *36* (9), 891-898.

76. Wu, C.-C.; Chen, P.; Peng, C.-H.; Wang, C.-C. $TiO_x/Ag/TiO_x$ multilayer for application as a transparent conductive electrode and heat mirror. *J Mater Sci: Mater Electron* **2013,** *24* (7), 2461-2468.

77. Angadi, M. A.; Nallamshetty, K. Heat mirrors using $CeO_2/Cu/CeO_2$ multilayer films. *J Mater Sci Lett* **1989,** *8* (4), 391-394.

78. Ohodnicki, P. R.; Andio, M.; Wang, C. Optical gas sensing responses in transparent conducting oxides with large free carrier density. *Journal of Applied Physics* **2014,** *116* (2), 024309.

79. B. Mooney, J.; B. Radding, S. *Spray Pyrolysis Processing* 2003; Vol. 12. p 81-101.

80. Hench, L. L.; West, J. K. The sol-gel process. *Chemical Reviews* **1990,** *90* (1), 33-72.

81. Depla, D.; Mahieu, S.; Greene, J. Sputter deposition processes. In *Handbook of deposition technologies for films and coatings : science, applications and technology,* Martin, P. M., Ed.; William Andrew: Oxford, UK, 2010, pp 253-296.

82. Perednis, D.; Gauckler, L. Thin Film Deposition Using Spray Pyrolysis. *J Electroceram* **2005,** *14* (2), 103-111.

83. Al-Dahoudi, N. Wet chemical deposition of transparent conducting coatings made of redispersable crystalline ITO nanoparticles on glass and polymeric substrates. Saarland University 2003.

84. Physical Vapor Deposition. In *The Materials Science of Semiconductors*, Rockett, A., Ed.; Springer US: Boston, MA, 2008, pp 505-572.

85. Lewis, B. G.; Paine, D. C. Applications and Processing of Transparent Conducting Oxides. *MRS Bulletin* **2011,** *25* (8), 22-27.

86. Jones, A. C.; Hitchman, M. L. *Chemical Vapour Deposition: Precursors, Processes and Applications*; Royal Society of Chemistry 2008. p 600.

87. Pasquarelli, R. M.; Ginley, D. S.; O'Hayre, R. Solution processing of transparent conductors: from flask to film. *Chemical Society Reviews* **2011,** *40* (11), 5406-5441.

88. Fischer, R. A.; Parala, H. Chapter 9 Metal-organic Chemical Vapour Deposition of Refractory Transition Metal Nitrides. In *Chemical Vapour Deposition: Precursors*; The Royal Society of Chemistry, 2009, pp 413-450.

89. Johnson, R. W.; Hultqvist, A.; Bent, S. F. A brief review of atomic layer deposition: from fundamentals to applications. *Materials Today* **2014,** *17* (5), 236-246.

90. Grover, M. S.; Hersh, P. A.; Chiang, H. Q.; Kettenring, E. S.; Wager, J. F.; Keszler, D. A. Thin-film transistors with transparent amorphous zinc indium tin oxide channel layer. *Journal of Physics D: Applied Physics* **2007,** *40* (5), 1335.

91. Chambers, S. A. Epitaxial growth and properties of thin film oxides. *Surface Science Reports* **2000,** *39* (5), 105-180.

92. Ponja, S. D.; Sathasivam, S.; Davies, H. O.; Parkin, I. P.; Carmalt, C. J. Polyoxometalate Complexes as Precursors to Vanadium-Doped Molybdenum or Tungsten Oxide Thin Films by Means of Aerosol-Assisted Chemical Vapour Deposition. *ChemPlusChem* **2016,** *81* (3), 307-314.

93. Nalwa, H. S. *Handbook of nanostructured materials and nanotechnology: synthesis and processing*; Academic Press 1999; Vol. 1. p 645.

94. Brennen, C. E. *Cavitation and Bubble Dynamics*; Oxford University Press: New York, 1995. p 254.

95. Barreras, F.; Amaveda, H.; Lozano, A. Transient high-frequency ultrasonic water atomization. *Experiments in Fluids* **2002,** *33* (3), 405-413.

96. Rodes, C.; Smith, T.; Crouse, R.; Ramachandran, G. Measurements of the Size Distribution of Aerosols Produced by Ultrasonic Humidification. *Aerosol Science and Technology* **1990,** *13* (2), 220-229.

97. Knapp, C. E.; Carmalt, C. J. Solution based CVD of main group materials. *Chemical Society Reviews* **2016**.

98. Porter, D. A. Coated glass. Google Patents, 1992.

99. Gilbert, S. D. a. B. *Foundations of Spectrocscopy (Oxford Chemistry Primers, 78)*; Oxford University Press: USA, 2000. p 96.

100. Rietveld, H. M. A Profile Refinement Method for Nuclear and Magnetic Structures. *J. Appl. Cryst.* **1969,** *2*, 65-71.

101. Le Bail, A.; Duroy, H.; Fourquet, J. L. *Ab Initio Structure Determination of $LiSbWO_6$ by X ray Powder Diffraction* 1988; Vol. 23. p 447-452.

102. Barrett, C. S., Massalski, T. B. *Structure of Metals, Third Edition: Crystallographic Methods, Principles and Data* 3rd ed.; Pergamon 1980.

103. Mittal, K. L. Adhesion Measurement of Thin Films. *ElectroComponent Science and Technology* **1976,** *3* (1), 21-42.

104. Guo, Y. M.; Zhu, L. P.; Jiang, J.; Li, Y. G.; Hu, L.; Xu, H. B.; Ye, Z. Z. Highly conducting and wide-band transparent F-doped $Zn_{1-x}Mg_xO$ thin films for optoelectronic applications. *Journal of Alloys and Compounds* **2014,** *602*, 294-299.

105. Waugh, M. R.; Hyett, G.; Parkin, I. P. Zinc Oxide Thin Films Grown by Aerosol Assisted CVD. *Chemical Vapor Deposition* **2008,** *14* (11-12), 366-372.

106. Carta, G.; El Habra, N.; Crociani, L.; Rossetto, G.; Zanella, P.; Zanella, A.; Paolucci, G.; Barreca, D.; Tondello, E. CVD of MgO Thin Films from Bis(methylcyclopentadienyl) Magnesium. *Chemical Vapor Deposition* **2007,** *13* (4), 185-189.

107. Knapp, C. E.; Hyett, G.; Parkin, I. P.; Carmalt, C. J. Aerosol-Assisted Chemical Vapor Deposition of Transparent Conductive Gallium–Indium–Oxide Films. *Chemistry of Materials* **2011,** *23* (7), 1719-1726.

108. Kim, H.; Auyeung, R. C. Y.; Piqué, A. Transparent conducting F-doped SnO_2 thin films grown by pulsed laser deposition. *Thin Solid Films* **2008,** *516* (15), 5052-5056.

109. Baka, O.; Azizi, A.; Velumani, S.; Schmerber, G.; Dinia, A. Effect of Al concentrations on the electrodeposition and properties of transparent Al-doped ZnO thin films. *J Mater Sci: Mater Electron* **2014,** *25* (4), 1761-1769.

110. Ebrahimifard, R.; Golobostanfard, M. R.; Abdizadeh, H. Sol–gel derived Al and Ga co-doped ZnO thin films: An optoelectronic study. *Applied Surface Science* **2014,** *290*, 252-259.

111. Hu, J.; Gordon, R. G. Atmospheric pressure chemical vapor deposition of gallium doped zinc oxide thin films from diethyl zinc, water, and triethyl gallium. *Journal of Applied Physics* **1992,** *72* (11), 5381-5392.

112. Babar, A. R.; Deshamukh, P. R.; Deokate, R. J.; Haranath, D.; Bhosale, C. H.; Rajpure, K. Y. Gallium doping in transparent conductive ZnO thin films prepared by chemical spray pyrolysis. *Journal of Physics D: Applied Physics* **2008,** *41* (13), 135404.

113. de la L. Olvera, M.; Maldonado, A.; Vega-Pérez, J.; Solorza-Feria, O. Aluminum-doped zinc oxide (ZnO:Al) thin films deposited on glass substrates by chemical spray starting from zinc pentanedionate and aluminum chloride. *Materials Science and Engineering: B* **2010,** *174* (1–3), 42-45.

114. Aragonès, A. C.; Palacios-Padrós, A.; Caballero-Briones, F.; Sanz, F. Study and improvement of aluminium doped ZnO thin films: Limits and advantages. *Electrochimica Acta* **2013,** *109*, 117-124.

115. Anderson, J.; Chris, G. Fundamentals of zinc oxide as a semiconductor. *Reports on Progress in Physics* **2009,** *72* (12), 126501.

116. Hu, J.; Gordon, R. G. Textured aluminum-doped zinc oxide thin films from atmospheric pressure chemical-vapor deposition. *Journal of Applied Physics* **1992,** *71* (2), 880-890.

117. Anusha, M.; Arivuoli, D. High intense violet luminescence in fluorine doped zinc oxide (FZO) thin films deposited by aerosol assisted CVD. *Journal of Alloys and Compounds* **2013,** *580*, 131-136.

118. Hu, J.; Gordon, R. G. Textured fluorine-doped ZnO films by atmospheric pressure chemical vapor deposition and their use in amorphous silicon solar cells. *Solar Cells* **1991,** *30* (1–4), 437-450.

119. Choi, Y.-J.; Park, H.-H. A simple approach to the fabrication of fluorine-doped zinc oxide thin films by atomic layer deposition at low temperatures and an investigation into the growth mode. *Journal of Materials Chemistry C* **2014,** *2* (1), 98-108.

120. Lemire, A. Zinc Methoxide. In *Encyclopedia of Reagents for Organic Synthesis*; John Wiley & Sons, Ltd, 2001.

121. Jana, S.; Berger, R. J. F.; Fröhlich, R.; Pape, T.; Mitzel, N. W. Oxygenation of Simple Zinc Alkyls: Surprising Dependence of Product Distributions on the Alkyl Substituents and the Presence of Water. *Inorganic Chemistry* **2007,** *46* (10), 4293-4297.

122. Sokołowski, K.; Justyniak, I.; Bury, W.; Grzonka, J.; Kaszkur, Z.; Mąkolski, Ł.; Dutkiewicz, M.; Lewalska, A.; Krajewska, E.; Kubicki, D.; Wójcik, K.; Kurzydłowski, K. J.; Lewiński, J. tert-Butyl(tert-butoxy)zinc Hydroxides: Hybrid Models for Single-Source Precursors of ZnO Nanocrystals. *Chemistry – A European Journal* **2015,** *21* (14), 5488-5495.

123. Petersen, T. O.; Tausch, E.; Schaefer, J.; Scherer, H.; Roesky, P. W.; Krossing, I. Ethyl-Zinc(II)-Cation Equivalents: Synthesis and Hydroamination Catalysis. *Chemistry – A European Journal* **2015,** *21* (39), 13696-13702.

124. Zhai, C.-H.; Zhang, R.-J.; Chen, X.; Zheng, Y.-X.; Wang, S.-Y.; Liu, J.; Dai, N.; Chen, L.-Y. Effects of Al Doping on the Properties of ZnO Thin Films Deposited by Atomic Layer Deposition. *Nanoscale Research Letters* **2016,** *11* (1), 407.

125. Maldonado, F.; Stashans, A. *Al-doped ZnO: Electronic, electrical and structural properties* 2010; Vol. 71. p 784-787.

126. Abrahams, S. C.; Bernstein, J. L. Remeasurement of the structure of hexagonal ZnO. *Acta Crystallographica Section B* **1969,** *25* (7), 1233-1236.

127. Walters, G.; Parkin, I. P. Aerosol assisted chemical vapour deposition of ZnO films on glass with noble metal and p-type dopants; use of dopants to influence preferred orientation. *Applied Surface Science* **2009,** *255* (13–14), 6555-6560.

128. Nunes, P.; Fortunato, E.; Tonello, P.; Braz Fernandes, F.; Vilarinho, P.; Martins, R. Effect of different dopant elements on the properties of ZnO thin films. *Vacuum* **2002,** *64* (3–4), 281-285.

129. Ghosh, R.; Basak, D.; Fujihara, S. Effect of substrate-induced strain on the structural, electrical, and optical properties of polycrystalline ZnO thin films. *Journal of Applied Physics* **2004,** *96* (5), 2689-2692.

130. Zhang, H.; Yang, S.; Liu, H.; Yuan, C. Preparation and characterization of transparent conducting ZnO:W films by DC magnetron sputtering. *Journal of Semiconductors* **2011,** *32* (4), 043002.

131. Lacy, F. Developing a theoretical relationship between electrical resistivity, temperature, and film thickness for conductors. *Nanoscale Research Letters* **2011,** *6* (1), 636-636.

132. Yoon, H. S.; Lee, K. S.; Lee, T. S.; Cheong, B.; Choi, D. K.; Kim, D. H.; Kim, W. M. Properties of fluorine doped ZnO thin films deposited by magnetron sputtering. *Solar Energy Materials and Solar Cells* **2008,** *92* (11), 1366-1372.

133. Shukla, A.; Kaushik, V.; Prasher, D. Growth and characterization of $Mg_xZn_{1-x}O$ thin films by aerosol-assisted chemical vapor deposition (AACVD). *Electron. Mater. Lett.* **2014,** *10* (1), 61-65.

134. Hu, J.; Gordon, R. G. Deposition of Boron Doped Zinc Oxide Films and Their Electrical and Optical Properties. *Journal of The Electrochemical Society* **1992,** *139* (7), 2014-2022.

135. Chen, S.; Noor, N.; Parkin, I. P.; Binions, R. Temperature and thickness-dependent growth behaviour and opto-electronic properties of Ga-doped ZnO films prepared by aerosol-assisted chemical vapour deposition. *Journal of Materials Chemistry A* **2014,** *2* (40), 17174-17182.

136. Dixon, S. C.; Scanlon, D. O.; Carmalt, C. J.; Parkin, I. P. n-Type doped transparent conducting binary oxides: an overview. *Journal of Materials Chemistry C* **2016,** *4* (29), 6946-6961.

137. Muchuweni, E.; Sathiaraj, T. S.; Nyakotyo, H. Effect of gallium doping on the structural, optical and electrical properties of zinc oxide thin films prepared by spray pyrolysis. *Ceramics International* **2016,** *42* (8), 10066-10070.

138. Jun, M.-C.; Park, S.-U.; Koh, J.-H. Comparative studies of Al-doped ZnO and Ga-doped ZnO transparent conducting oxide thin films. *Nanoscale Research Letters* **2012,** *7* (1), 1-6.

139. Ponja, S. D.; Sathasivam, S.; Parkin, I. P.; Carmalt, C. J. Transparent conductive aluminium and fluorine co-doped zinc oxide films via aerosol assisted chemical vapour deposition. *RSC Advances* **2014,** *4* (91), 49723-49728.

140. Mao, C.; Fang, L.; Zhang, H.; Li, W.; Wu, F.; Qin, G.; Ruan, H.; Kong, C. Effect of B doping on optical, electrical properties and defects of ZnO films. *Journal of Alloys and Compounds* **2016,** *676*, 135-141.

141. Pugalenthi, A. S.; Balasundaraprabhu, R.; Gunasekaran, V.; Muthukumarasamy, N.; Prasanna, S.; Jayakumar, S. Effect of thickness on the structural, optical and electrical properties of RF magnetron sputtered GZO thin films. *Materials Science in Semiconductor Processing* **2015,** *29*, 176-182.

142. Fortunato, E.; Raniero, L.; Silva, L.; Gonçalves, A.; Pimentel, A.; Barquinha, P.; Águas, H.; Pereira, L.; Gonçalves, G.; Ferreira, I.; Elangovan, E.; Martins, R. Highly stable transparent and conducting gallium-doped zinc oxide thin films for photovoltaic applications. *Solar Energy Materials and Solar Cells* **2008,** *92* (12), 1605-1610.

143. Ellmer, K. Resistivity of polycrystalline zinc oxide films: current status and physical limit. *Journal of Physics D: Applied Physics* **2001,** *34* (21), 3097.

144. Lin, Y. C.; Chen, T. Y.; Wang, L. C.; Lien, S. Y. Comparison of AZO, GZO, and AGZO Thin Films TCOs Applied for a-Si Solar Cells. *Journal of The Electrochemical Society* **2012,** *159* (6), H599-H604.

145. Sahoo, S. K.; Gupta, C. A.; Singh, U. P. Impact of Al and Ga co-doping with different proportion in ZnO thin film by DC magnetron sputtering. *J Mater Sci: Mater Electron* **2016,** *27* (7), 7161-7166.

146. Seo, K.-W.; Shin, H.-S.; Lee, J.-H.; Chung, K.-B.; Kim, H.-K. The effects of thickness on the electrical, optical, structural and morphological properties of Al and Ga co-doped ZnO films grown by linear facing target sputtering. *Vacuum* **2014,** *101*, 250-256.

147. Shi, Q.; Zhou, K.; Dai, M.; Lin, S.; Hou, H.; Wei, C.; Hu, F. Growth of high-quality Ga–F codoped ZnO thin films by mid-frequency sputtering. *Ceramics International* **2014,** *40* (1, Part A), 211-216.

148. Chen, S.; Carraro, G.; Barreca, D.; Sapelkin, A.; Chen, W.; Huang, X.; Cheng, Q.; Zhang, F.; Binions, R. Aerosol assisted chemical vapour deposition of Ga-doped ZnO films for energy efficient glazing: effects of doping concentration on the film growth behaviour and opto-electronic properties. *Journal of Materials Chemistry A* **2015,** *3* (24), 13039-13049.

149. Pawar, B. N.; Ham, D.-H.; Mane, R. S.; Ganesh, T.; Cho, B.-W.; Han, S.-H. Fluorine-doped zinc oxide transparent and conducting electrode by chemical spray synthesis. *Applied Surface Science* **2008,** *254* (20), 6294-6297.

150. Bhachu, D. S.; Scanlon, D. O.; Sankar, G.; Veal, T. D.; Egdell, R. G.; Cibin, G.; Dent, A. J.; Knapp, C. E.; Carmalt, C. J.; Parkin, I. P. Origin of High Mobility in Molybdenum-Doped Indium Oxide. *Chemistry of Materials* **2015,** *27* (8), 2788-2796.

151. Lin, Y.-Y.; Lee, H.-Y.; Ku, C.-S.; Chou, L.-W.; Wu, A. T. Bandgap narrowing in high dopant tin oxide degenerate thin film produced by atmosphere pressure chemical vapor deposition. *Applied Physics Letters* **2013,** *102* (11), 111912.

152. Li, Y.; Wang, J.; Feng, B.; Duan, K.; Weng, J. Synthesis and characterization of antimony-doped tin oxide (ATO) nanoparticles with high conductivity using a facile ammonia-diffusion co-precipitation method. *Journal of Alloys and Compounds* **2015,** *634*, 37-42.

153. Yadav, A. A.; Pawar, S. C.; Patil, D. H.; Ghogare, M. D. Properties of (200) oriented, highly conductive SnO_2 thin films by chemical spray pyrolysis from non-aqueous medium: Effect of antimony doping. *Journal of Alloys and Compounds* **2015,** *652*, 145-152.

154. Castañeda, L. Present Status of the Development and Application of Transparent Conductors Oxide Thin Solid Films. *Materials Sciences and Applications* **2011,** *Vol.02 No.09*, 10.

155. Banyamin, Y. Z.; Kelly, J. P.; West, G.; Boardman, J. Electrical and Optical Properties of Fluorine Doped Tin Oxide Thin Films Prepared by Magnetron Sputtering. *Coatings* **2014,** *4* (4).

156. Lekshmy, S. S.; Daniel, G. P.; Joy, K. Microstructure and physical properties of sol gel derived SnO_2:Sb thin films for optoelectronic applications. *Applied Surface Science* **2013,** *274*, 95-100.

157. Correa Baena, J. P.; Agrios, A. G. Transparent Conducting Aerogels of Antimony-Doped Tin Oxide. *ACS Applied Materials & Interfaces* **2014,** *6* (21), 19127-19134.

158. Ravichandran, K.; Philominathan, P. Analysis of critical doping level of sprayed antimony doped tin oxide films. *J Mater Sci: Mater Electron* **2010,** *22* (2), 158-161.

159. Yadav, A. A. Influence of film thickness on structural, optical, and electrical properties of spray deposited antimony doped SnO_2 thin films. *Thin Solid Films* **2015,** *591, Part A*, 18-24.

160. Luan, C.; Zhu, Z.; Mi, W.; Ma, J. Effect of Sb doping on structural, electrical and optical properties of epitaxial SnO_2 films grown on r-cut sapphire. *Journal of Alloys and Compounds* **2014,** *586*, 426-430.

161. Gaewdang, T.; Wongcharoen, N. Growth and Characterization of Co-Doped Fluorine and Antimony in Tin Oxide Thin Films Obtained by Ultrasonic Spray Pyrolysis. *Journal of Solid Mechanics and Materials Engineering* **2007,** *1* (4), 592-601.

162. Vázquez-Arreguín, R.; Aguilar-Frutis, M.; Falcony-Guajardo, C.; Castañeda-Galván, A.; Mariscal-Becerra, L.; Gallardo-Hernández, S.; Alarcón-Flores, G.; García-

Rocha, M. Electrical, Optical and Structural Properties of SnO_2:Sb:F Thin Films Deposited from $Sn(acac)_2$ by Spray Pyrolysis. *ECS Journal of Solid State Science and Technology* **2016,** *5* (3), Q101-Q107.

163. Ravichandran, K., Muruganantham, G. and Sakthivel, B. Highly conducting and crystalline doubly doped tin oxide films fabricated using a low-cost and simplified spray technique. *Physica B: Condensed Matter* **2009,** *404* (21), 4299-4302.

164. Sathasivam, S.; Arnepalli, R. R.; Bhachu, D. S.; Lu, Y.; Buckeridge, J.; Scanlon, D. O.; Kumar, B.; Singh, K. K.; Visser, R. J.; Blackman, C. S.; Carmalt, C. J. Single Step Solution Processed GaAs Thin Films from $GaMe_3$ and $^tBuAsH_2$ under Ambient Pressure. *The Journal of Physical Chemistry C* **2016,** *120* (13), 7013-7019.

165. Li, Y.; Liu, J.; Liang, J.; Yu, X.; Li, D. Tunable Solar-Heat Shielding Property of Transparent Films Based on Mesoporous Sb-Doped SnO_2 Microspheres. *ACS Applied Materials & Interfaces* **2015,** *7* (12), 6574-6583.

166. Baur, W. H.; Khan, A. A. Rutile-type compounds. IV. SiO_2, GeO_2 and a comparison with other rutile-type structures. *Acta Crystallographica Section B* **1971,** *27* (11), 2133-2139.

167. Yu, S.; Zhang, W.; Li, L.; Xu, D.; Dong, H.; Jin, Y. Fabrication of p-type SnO_2 films *via* pulsed laser deposition method by using Sb as dopant. *Applied Surface Science* **2013,** *286*, 417-420.

168. Rahal, A.; Benhaoua, A.; Bouzidi, C.; Benhaoua, B.; Gasmi, B. Effect of antimony doping on the structural, optical and electrical properties of SnO_2 thin films prepared by spray ultrasonic. *Superlattices and Microstructures* **2014,** *76*, 105-114.

169. Yang, W.; Yu, S.; Zhang, Y.; Zhang, W. Properties of Sb-doped SnO_2 transparent conductive thin films deposited by radio-frequency magnetron sputtering. *Thin Solid Films* **2013,** *542*, 285-288.

170. Hammad, T. M.; Hejazy, N. K. Structural, electrical, and optical properties of ATO thin films fabricated by dip coating method. *International Nano Letters* **2012,** *2* (1), 1-5.

171. Elangovan, E.; Ramamurthi, K. A study on low cost-high conducting fluorine and antimony-doped tin oxide thin films. *Applied Surface Science* **2005,** *249* (1–4), 183-196.

172. Jung, D.-W.; Park, D.-W. Synthesis of nano-sized antimony-doped tin oxide (ATO) particles using a DC arc plasma jet. *Applied Surface Science* **2009,** *255* (10), 5409-5413.

173. Kojima, M.; Kato, H.; Gatto, M. Blackening of tin oxide thin films heavily doped with antimony. *Philosophical Magazine Part B* **1993,** *68* (2), 215-222.

174. Naghavi, N.; Marcel, C.; Dupont, L.; Leriche, J. B.; Tarascon, J. M. On the electrochromic properties of antimony–tin oxide thin films deposited by pulsed laser deposition. *Solid State Ionics* **2003,** *156* (3), 463-474.

175. Korhonen, E.; Prozheeva, V.; Tuomisto, F.; Bierwagen, O.; Speck, J. S.; White, M. E.; Galazka, Z.; Liu, H.; Izyumskaya, N.; Avrutin, V.; Ü, Ö.; Morkoç, H. Cation vacancies and electrical compensation in Sb-doped thin-film SnO_2 and ZnO. *Semiconductor Science and Technology* **2015,** *30* (2), 024011.

176. Geraldo, V.; Briois, V.; Scalvi, L. V. A.; Santilli, C. V. Structural Characterization of Nanocrystalline Sb-Doped SnO_2 Xerogels by Multiedge X-ray Absorption Spectroscopy. *The Journal of Physical Chemistry C* **2010,** *114* (45), 19206-19213.

177. Samatov, I. G.; Jeppesen, B. R.; Larsen, A. N.; Ram, S. K. Room-temperature rf-magnetron sputter-deposited W-doped indium oxide: decoupling the influence

of W dopant and O vacancies on the film properties. *Applied Physics A* **2016,** *122* (4), 458.

178. Yu, S.; Li, L.; Sun, Z.; Zheng, H.; Dong, H.; Xu, D.; Zhang, W. Characteristics of Transparent Conducting W-Doped SnO_2 Thin Films Prepared by Using the Magnetron Sputtering Method. *Journal of the American Ceramic Society* **2015,** *98* (4), 1121-1127.

179. Vadivel, S.; Rajarajan, G. Effect of W doping on structural, optical and photocatalytic activity of SnO_2 nanostructure thin films. *Journal of Materials Science: Materials in Electronics* **2015**; Vol. 26.

180. Huang, Y.; Zhang, Q.; Li, G.; Yang, M. Tungsten-Doped Tin Oxide Thin Films Prepared by Pulsed Plasma Deposition. *Materials Charactrization* **2009**; Vol. 60. p 415-419.

181. Huo, X.; Jiang, S.; Liu, P.; Shen, M.; Qiu, S.; Li, M.-Y. Molybdenum and tungsten doped SnO_2 transparent conductive thin films with broadband high transmittance between the visible and near-infrared regions. *CrystEngComm* **2017,** *19* (30), 4413-4423.

182. Huang, Y.; Li, G.; Feng, J.; Zhang, Q. Investigation on structural, electrical and optical properties of tungsten-doped tin oxide thin films. *Thin Solid Films* **2010,** *518* (8), 1892-1896.

183. Huang, Y.; Li, D.; Feng, J.; Li, G.; Zhang, Q. Transparent conductive tungsten-doped tin oxide thin films synthesized by sol–gel technique on quartz glass substrates. *Journal of Sol-Gel Science and Technology* **2010,** *54* (3), 276-281.

184. Turgut, G.; Keskenler, E. F.; Aydın, S.; Tatar, D.; Sonmez, E.; Dogan, S.; Duzgun, B. Characteristic evaluation on spray-deposited WFTO thin films as a function of W doping ratio. *Rare Metals* **2014,** *33* (4), 433-441.

185. Jianwen, Y.; Ting, M.; Zhao, Y.; Can, C.; Qun, Z. Investigation of tungsten doped tin oxide thin film transistors. *Journal of Physics D: Applied Physics* **2015,** *48* (43), 435108.

186. Kumar, M.; Kumar, A.; Abhyankar, A. C. Influence of Texture Coefficient on Surface Morphology and Sensing Properties of W-Doped Nanocrystalline Tin Oxide Thin Films. *ACS Applied Materials & Interfaces* **2015,** *7* (6), 3571-3580.

187. Wang, J. T.; Shi, X. L.; Liu, W. W.; Zhong, X. H.; Wang, J. N.; Pyrah, L.; Sanderson, K. D.; Ramsey, P. M.; Hirata, M.; Tsuri, K. Influence of Preferred Orientation on the Electrical Conductivity of Fluorine-Doped Tin Oxide Films. *Sci. Rep.* **2014,** *4*.

188. Pilkington. NSG TEC Technical Data. https://www.pilkington.com/en/global/products/product-categories/special-applications/nsg-tec-for-technical-applications - literature.

189. Powell, M. J.; Carmalt, C. J. Aerosols: A Sustainable Route to Functional Materials. *Chemistry – A European Journal* **2017,** *23* (62), 15543-15552.

190. Powell, M. J.; Potter, D. B.; Wilson, R. L.; Darr, J. A.; Parkin, I. P.; Carmalt, C. J. Scaling aerosol assisted chemical vapour deposition: Exploring the relationship between growth rate and film properties. *Materials & Design* **2017,** *129* (Supplement C), 116-124.

191. Aoife, B. K.; Elisabetta, A.; David, O. S.; Igor, V. S.; Graeme, W. W. Assessing the potential of Mg-doped Cr_2O_3 as a novel p -type transparent conducting oxide. *Journal of Physics: Condensed Matter* **2016,** *28* (12), 125501.

192. Williamson, B. A. D.; Buckeridge, J.; Brown, J.; Ansbro, S.; Palgrave, R. G.; Scanlon, D. O. Engineering Valence Band Dispersion for High Mobility p-Type Semiconductors. *Chemistry of Materials* **2017,** *29* (6), 2402-2413.